Debonding and stretching of biogenic cellular structures

Alexander Taufiq Safar

Thesis submitted in candidature for the degree of

Doctor of Philosophy

School of Mathematics

Cardiff University

2019

Abstract

Plant material can regulate the mechanical properties of its cellular structure by changing: (i) the structure of the cell wall, (ii) the cell core pressure, and (iii) the cell-cell cohesion. The relevant scale at which such phenomena occur, though beyond the capacity of the human eye, can be followed by mechanical analysis and mathematical models based on micro-structural evidence. This thesis focuses on two fundamental mechanical aspects. First, it concerns the mechanism of cell debonding, as this is key in explaining the softening of fruit and legumes during storage or cooking, and is decisive for the perceived quality of food products. Particular attention is given to the mathematical modelling of damage through shear deformation as this has been largely neglected in the literature due to many theoretical and computational difficulties. Second, it provides a multiscale hyperelastic framework which relates the stresses and strains of a whole structure to those at the cell level, and vice versa. Specifically, the non-linear elastic moduli at the macroscopic level are derived systematically from those at the cell level.

Acknowledgements

First and foremost, I am thankful to Dr Angela Mihai for this opportunity. With her guidance and expertise I have been able to conduct an exploration of this fascinating subject, whilst keeping a grounding in the essential components which have led to the publication of key results included in this thesis.

I wish to acknowledge Dr Hayley Wyatt for teaching me how to use experimental equipment and finite element software. There are many engineers whose insights have led me to a greater understanding, including Professor Sam Evans (Cardiff), Dr Mokarram Hossain (Swansea), Michael Robinson and Dr Shwe Soe (Cardiff).

On a more personal note, I have a great appreciation of my office friends throughout this experience, including Lorenzo De Biase, Dr Waleed Ali, Danny Groves and Joe Bishop, who have provided a friendly and relaxed office environment. Further still, there are countless people who have inspired me to achieve this goal, including Dr Ben McGovern, Dr Dominic Hosler, Dr Mark Pearce, Peter Lavelle, Dr Paul Smart and James Ashton.

Finally, I must acknowledge my family, my partner and my close friends, who have supported me throughout this process.

Publications

The research findings published in the journal articles listed below are incorporated into this thesis as part of the main chapters, except for those of the experimental paper Wyatt *et al.* (2019), which are deferred to the Appendix B.

1. Wyatt HL, **Safar AT**, Clarke A, Evans S, Mihai LA. 2019. Non-linear scaling effects in the stiffness of soft cellular structures. Royal Society Open Science 6:181361.

2. **Safar AT**, Mihai LA. 2018. The non-linear elasticity of hyperelastic models for stretch-dominated cellular structures. International Journal of Non-Linear Mechanics 106, pp. 144-154.

3. Mihai LA, **Safar AT**, Wyatt HL. 2018. Debonding of cellular structures with fibre-reinforced cell walls under shear deformation. Journal of Engineering Mathematics 109(1), pp. 3-19.

4. Wyatt HL, **Safar AT**, Evans S, Mihai LA. 2017. The elastic behaviour of soft cellular structures under large tensile loading. Presented at: 7th International Conference on Mechanics of Biomaterials and Tissues, Hawaii, USA, 10-14 December 2017.

5. **Safar AT**, Wyatt HL, Mihai LA. 2017. Debonding of cellular structures under shear deformation. Presented at: 25th Conference of the UK Association for Computational Mechanics, University of Birmingham, Birmingham, UK, 11-13 April 2017.

The author of this thesis has also collaborated with a number of researchers within the Cardiff School of Engineering. This includes the classification of a soft 3D printing material ninjaflex, with Michael Robinson and the classification of neonatal myocardium tissue, with Faizan Ahmed.

Conferences and invited talks

The work included in this thesis has been disseminated widely at national and international conferences and scientific meetings, including:

- 10th European Solid Mechanics Conference
  Bologne, Italy (July 2018)
- Invited talk in the Food Sciences group
  University of Nottingham (June 2018)
- 10th Oxford SIAM-IMA Student Chapter Conference
  University of Oxford (May 2018)
- Newton Trilateral Workshop: Bio-soft-matter & Agrifood Challenges
  Sao Paulo, Brazil (March 2018)
- SIAM-UKIE Annual Meeting
  University of Southampton (Jan 2018)
- Public engagement: Invited school lecture 'Patterns in the world around us'
  The Romsey School, Southampton (July 2017)
- Public engagement: Science Cafe 'Why does the apple fall apart?'
  Cardiff City Centre (June 2017)
- 6th SIAM National Student Conference
  NUI Galway (May 2017)
- 25th UK-ACM Computational Mechanics
  University of Birmingham (Apr 2017)

In addition, most of the work has been communicated at numerous research seminars organised by the Applied and Computational Mathematics Group and the School of Engineering at Cardiff University.

Awards

Several prizes and funding awards have been presented to the author of this thesis throughout his postgraduate research, which are gratefully acknowledged:

- EPSRC and Cardiff University Postgraduate Research Studentship (October 2015 - April 2019)
- SIAM-IMA Student Travel Award (May 2018)
- Full Sponsorship for participation in the Newton Trilateral Workshop, Brazil, by the Newton Fund, British Council, ANII and FAPESP (March 2018)
- SIAM-UKIE Student Travel Award (January 2018)
- SIAM-IMA Cardiff Student Chapter Three Minute Thesis Presentation - Second Place (May 2017)
- 6th SIAM National Student Conference - Best Presenter (May 2017)
- Cardiff Spark Ideas - Competition Winner (April 2017)
- UK-ACM Mike Crisfield Prize for best presenter among PhD students and potsdoctoral researchers (April 2017)
- SIAM-UKIE Poster Prize (Jan 2017)
- SIAM-UKIE Student Travel Award (Jan 2017)

Contents

List of Figures

List of Tables

Chapter 1

Introduction

In this chapter, first, to motivate our work, we introduce some of the processes which have resulted in the food products that we know and love today. We also discuss the physical principles which affect the shape and cellular structure of these products, and describe textural features and the link between texture and mechanical properties at the cellular level. We then outline the continuum mechanics problems studied in this thesis.

1.1 Background and motivation

Fruits have evolved through natural selective processes. Appealing properties (to the animals who choose to consume them) have promoted success of the plant species [41]. Fruit ripens and becomes most attractive when the seeds are fully developed, and thus mature seeds are transported to new locations through the animal gut [155, p. 78]. Man has also domesticated plants using selective breeding over millennia to enhance specific characteristics. This has lead to many of the cultivars known today. For example, rapeseed, mustard, cabbage, kale, brussel sprouts, broccoli and turnip have all been bred from an original genus of brassica, where either the seeds, leaves, stems, buds, flowers or roots have been optimised [40, 80]. More recently, scientific methods such as genetic modification (GM) have

been developed to further control food quality [158]. Desirable characteristics can include: crop yield (shape, size and quantity), consistency/uniformity, time to maturity, drought/pest resistance, taste, nutrition, appearance and texture.

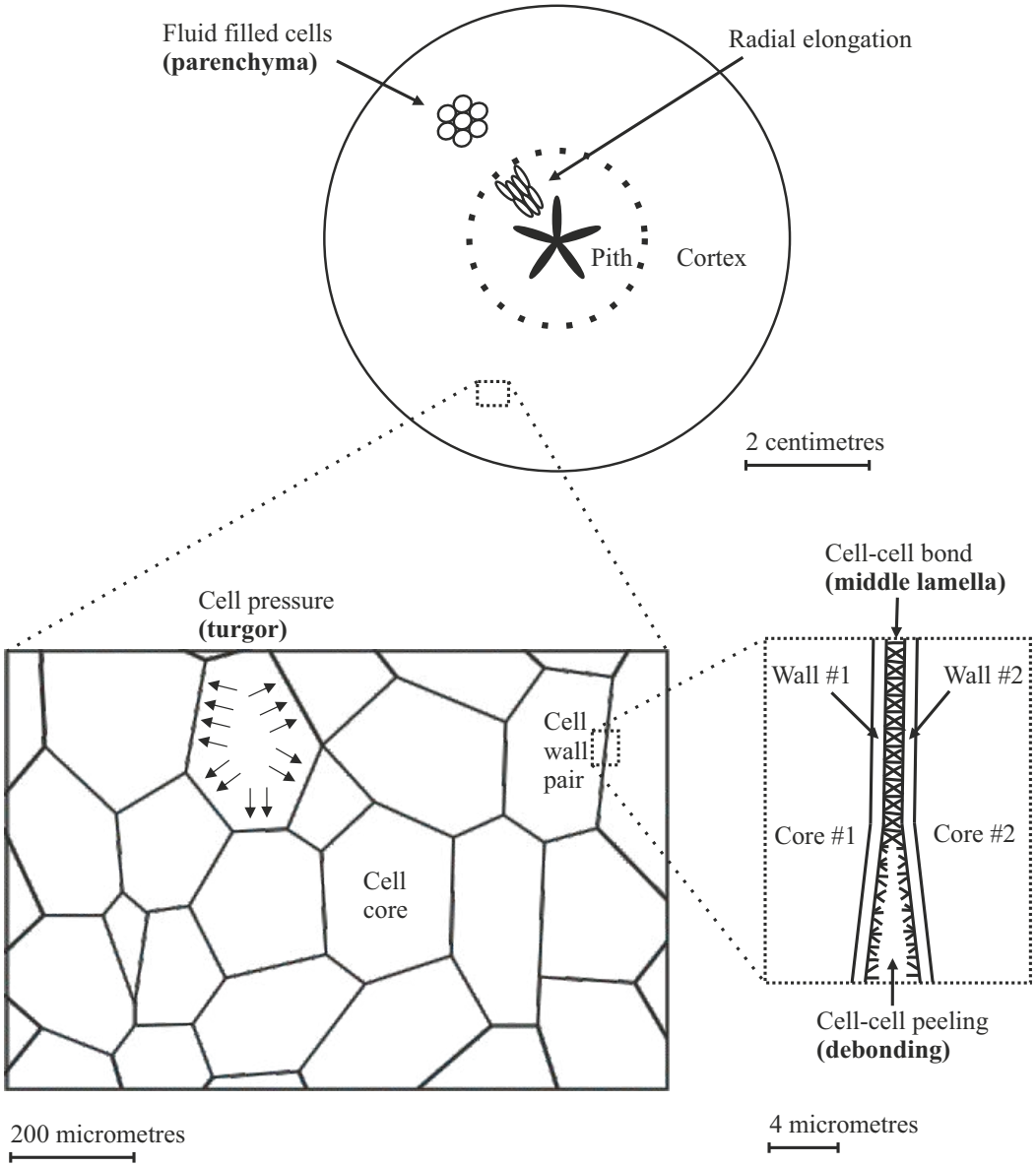

Figure 1.1: Multiscale demonstration of the cellular structure of an apple, with an equatorial slice of an apple (top), cellular tissue including cell core pressure (bottom left) and neighbouring cell walls with a cohesive cell-cell bond (bottom right). Equivalent biological terms are shown in brackets. The cellular structure is similar for potatoes, and many soft fruit including pears, tomatoes and kiwi.

Tubers (e.g. potato) and legumes (e.g. lentils) are deceptively similar to fruit (e.g. apple, pear). The cellular tissues are comprised of a cohesive network, the middle lamella, binding together fluid-filled parenchyma cells [64] (Figure 1.1). They can all be used as a food product, or to seed new plants in the next season. Cell-cell disassociation (or debonding) affects the perceived texture but is also an essential mechanism in new root growth [139]. The cytoplasm in mature apples contains high levels of sugars, whereas in potatoes the sugars are converted into starch. The cell walls also contain fibres important in our diets - a fibre-reinforced matrix, comprising of hemicellulouse, pectins and glycoproteins [122]. This primary structural component, within the hydrostatic structure, can sustain large deformations and the presence of fibres gives the walls a non-linear mechanical response [28, 46, 59].

Gene activation and regulation are known to control functions, such as cell division and expansion, but the shape and form is also developed by the physical forces in the environment [67, p. 27]. An example of force-growth interaction is the cellular structure of trabecular bone. As a load-bearing material, the cellular structure is in alignment with the principal stretches across the geometry (approximated by an isotropic homogeneous material under the same mechanical loading). Wolff's law of bone remodelling is used to describe the active process that bones adopt to realign to best resist applied load [141]. Similarly, in non-load-bearing materials, such as fruit (primarily supporting their own body forces), the cell geometry and stiffness must also be influenced by some local mechanical forces. In an apple, the central region (pith) has large radially organised elongated cells, whereas in the cortex where there is less competition for space, the cells are more uniform (and with larger intercellular spaces) [78] (see Figure 1.1 for reference). Active remodelling can be observed in root growth as lateral roots initiate within the mother root, which debonds its cells to allow for new growth [128].

Texture can be defined as the physical response of a material or substance to some contact stimuli, with textural characteristics stemming from the behaviours of deformation, failure and flow [71]. We primarily assess texture through touch, mouth feel and experiment, although our interpretation can also be influenced by psychological factors [71]. Squeezing a fruit or vegetable can assess how ripe or fresh the produce is [142]. A firm avocado is not yet ripe, while a soft/limp carrot is stale. Taste and appearance are primary factors in many foods, but there is a large selection of mild flavoured foods (bread, mashed potatoes) where texture is the most important attribute [27]. The boiling of potato causes the parenchyma cells to swell, increasing the cell core (turgor) pressure and cell wall tension, which reduces its strength, allowing it to fail more easily [90]. Terminology used to describe the texture of mash potato includes: soft, fresh, smooth, creamy, fluffy, light, airy, lumpy, sticky, claggy, soggy, wet, dense, dry, hard, bitty, grainy and mealy. These descriptive words are subjective and the terminology and definitions used in literature are inconsistent [77].

The interactions we have with food (squeezing, slicing, chewing, etc.) can be simulated with mechanical testing methods, such as compression, tension, penetration and bending tests [17]. These engineering tools can quantify properties in space and time, but the information we extract from them requires precise and meaningful definition. Many have set out to standardise terminology, such as [71]:

- Hardness: force required to compress;
- Crispness: amount and pitch of sound generated;
- Juiciness: amount of fluid released.

A greater understanding of the relationship between cellular level properties and texture may lead to overcoming quality problems in plant foods [77] and also inform industrial processing techniques (such as the extraction of oils [24]).

1.2 Contribution of this thesis

Texture is a manifestation of the micro- and macro-organisation of the tissue [77]. In apples and potatoes, the texture is dependant on the structural integrity of the cell wall, middle lamella and turgor pressure [59, 123, 130]. The interplay between the cell level parameters and the macroscopic behaviour at the tissue is investigated in this work using the tools of finite elasticity theory and computational finite element models. As a thesis in applied mathematics, the general approach adopted here is outlined as follows:

1. Choose specific phenomenological processes to study;
2. Make appropriate simplifications and assumptions;
3. Create model problems;
4. Develop and apply suitable theoretical and computational frameworks;
5. Interpret and draw insight from the results.

1.2.1 Debonding

The first subject of our attention is the process of cell-cell debonding. The texture named 'mealy', or 'mealiness' occurs if less energy is required to debond cells rather than to rupture/burst them [53,79]. This is desirable for baked and mashed potato but not for potatoes in soups or salads where the structural integrity of the piece is important [135]. In apples, this texture can be dry and bitty as the cells do not release their fluid. The biological process which promotes this texture has three major components [19, 29, 70, 168]:

- Dismantling of the middle lamella;
- Degradation of the pectin in the cell walls;
- Dehydration and loss of turgor pressure.

If the pectin levels in the cell walls drops, then the cell walls become stiffer and harder to rupture. If the intercellular bonds weaken and break down, then less force needed to separate parenchyma cells. These, in turn, cause the failure mode to transition from cell bursting/rupture to cell debonding. In addition, if the force acting on the cell wall from the cell core decreases, then the cell wall will be under less tension and its strength will increase. Further drops in pressure will promote cell shrinking, which also pulls at the intercellular bonds [19, 70, 81].

This study aims to explore the interactions of these variables on the behaviour of debonding. Shear is chosen as the primary deformation of study as it is ubiquitous yet largely neglected in literature, due to difficulties in engineering testing and measurement. In practice, our teeth are offset and so, during chewing, our food is subjected to shearing forces. In this thesis, the investigation is approached systematically, firstly considering the behaviour on the smallest scale and then increasing size and complexity to find multiscale relationships.

We start with a purely analytical study of generalised shear in a transversely isotropic cell wall, finding the permissible forms of the deformed face. This is used to explore if two walls in unilateral contact can debond when they are sheared together. The contribution of cellulose fibres to the mechanical properties of the walls is captured by transverse isotropy, and of the cell core by the inter-cellular pressure. Moving up the scale, we consider shearing of collections of cells in unilateral contact. As the solution to this more complex problem relies on the finite element method employed, computational scaling with model size is explored, such that large scale models can be evaluated. This includes cell wall elasticity, cohesion and cell core effects. A model parameter analysis is carried out to shed light on the fundamental physical interactions observed in the literature for debonding in fruit tissues.

1.2.2 Multiscale stretching

Our second main focus is developing direct models which relate the cell level properties to the tissue stiffness. Here, a general continuum hyperelastic framework is stated for creating new isotropic material models describing cellular materials. In this case, we assume that no failure occurs at the microscopic scale, such as cell rupturing or debonding. These models can be used to extend the idea of model scalability further as these are easier to compute and can represent large tissue samples. Such models are not limited to fruit and vegetables, but can describe other non-load bearing structures, such as the brain, fat tissue and man-made architectured materials, such as tissue scaffolds. The main restriction is that the architecture deforms primarily by wall stretching rather than bending. They may have cells which are closed and possibly pressurised by some compressible or incompressible contents. Alternatively, cells may be open collections of struts that would not inhibit the transportation of fluid. Non-linear elastic parameters can be derived for these new cellular material models, and used to measure the relationship between scales, such as the effects of cell core stiffness on the macroscopic non-linear shear modulus. The models can be applied to experimental data of cellular tissues to estimate cell wall properties from the tissue elastic behaviour.

This thesis aims to provide insight into the mathematics of shearing materials, computational procedures for cellular modelling, non-linear elastic moduli and an insight into the multiscale relationships between parameters - which can all have an impact on research and development in food science. This work could also be applied to the creation of synthetic industrially engineered materials using the developing technology of additive manufacture and 3D printing, which is briefly explored as well.

Chapter 2

Prerequisites and notation

2.1 Introduction

Robert Hooke is responsible for early work in elasticity and also first identified the cellular structure of cork using early microscopes in 1665 [75, p. 112]. Hooke's law gives a linear relationship between force and deformation in a spring. A linearly elastic (or Hookean) material is the fundamental principal in the *infinitesimal strain / small strain / linear elastic* regime, which adequately explains the behaviour of many materials in engineering. This elastic regime was applied to cellular materials in 1958 to investigate the relationships of cell wall stiffness and turgor pressure on macroscopic stiffness [123]. An extensive overview of the mechanical behaviour of cellular structures, studied under the linearly elastic regime is provided in [66] (see also [63–65]).

2.1.1 Preliminary concepts from linear elasticity

When a sample undergoes mechanical deformation, the load and the displacement can be recorded giving a force-deformation curve. The stiffness, rigidity or firmness is the slope of the initial linear curve. This is considered elastic behaviour if the original shape is recovered when loads are released. If the deformation rate changes

significantly, this could be considered a yield point, which is often an indication of some microscopic damage/rearrangement. In this case, the original shape is often not recovered and the result is a plastic deformation. Large scale failure, observed as a dramatic drop at the end of the force-displacement curve, is an indication of the material strength and the required force for failure. The toughness is given by the work done (force times deformation) to reach failure and is also represented as the area under the curve.

Rescaling the force by the cross sectional area gives stress (Pa) and the deformation by length gives strain (dimensionless). A stress-strain curve and the parameters derived from it are considered *material properties* as opposed to *sample properties*. The following elastic parameters are important measures of material properties and are considered constants in the linear elastic regime [113]:

- Young's modulus, or elastic modulus $E > 0$ is the stiffness of a material in uniaxial tension and is given by the slope of the stress-strain curve. The larger the modulus, the stiffer the material and the more force is required to deform it.

- Poisson's ratio ν is the negative ratio of lateral to longitudinal strain in uniaxial tensile stress. Values of ν are typically between -1 and 0.5 for an isotropic material, with $\nu = 0.5$ for incompressible materials, which maintain their volume under deformation.

- Shear modulus μ is the ratio of shear stress to shear strain.

- Bulk modulus κ represents the materials response to uniform compression or hydrostatic pressure and the resulting decrease in volume. For nearly incompressible materials κ is large compared to μ, tending towards infinity for true incompressibility.

For a linear isotropic material (with uniform behaviour in all directions), these parameters are not independent: from any two, the others can be calculated.

2.1.2 Finite elasticity

Finite strain / finite elasticity approaches consider large deformations and capture non-linear behaviour caused by changes in properties as the deformation progresses [6, 58, 84]. These approaches raise numerous challenges and opportunities for new (and often counter-intuitive) findings. The non-linear elasticity theory has been applied to the study of cellular materials, capturing behaviours not observed in the small strain regime, in [103, 104, 174].

Next, we summarise some elements of finite elasticity theory [67, 73, 88, 112, 127, 157] that are relevant for the results of this thesis, including: deformation of a solid body (kinematics), stress within a continuum material, and boundary and contact conditions, which are at the heart of this thesis.

2.2 Large-strain deformation

2.2.1 Deformation

Definition 2.2.1 *(material body) A material body $\mathcal{B}$ is a set of material points which occupy a compact domain of the 3D Euclidean space, $\overline{\Omega} \subseteq \mathbb{R}^3$. The interior of the body is an open, bounded and connected subset $\Omega \subset \mathbb{R}^3$ with boundary $\Gamma = \partial\Omega = \overline{\Omega}\backslash\Omega$, which is Lipschitz continuous, and therefore a unit normal vector $\mathbf{n}$ exists almost everywhere on Γ.*

Definition 2.2.2 *(reference configuration) A reference (material) configuration $\mathcal{B}_0$ is a chosen configuration where the material points have unique coordinates $\mathbf{X} = (X_1, X_2, X_3) \in \overline{\Omega}$.*

Definition 2.2.3 *(current configuration) The current (spatial) configuration $\mathcal{B}$ is the configuration after a deformation has been applied and has coordinates $\mathbf{x} = (x_1, x_2, x_3) \in \mathbb{R}^3$.*

Transformation from the reference configuration to the current configuration is achieved with a map χ, such that:

$$\mathbf{x} = \chi(\mathbf{X}). \tag{2.2.1}$$

This map is a one-to-one, continuously differentiable vector field $\chi : \Omega \to \mathbb{R}^3$ with $\det(\nabla\chi) > 0$ on Ω, such that χ is injective on Ω, to ensure that no two material points in the interior of the body can map to the same location (no interpenetration). Then the inverse map χ^{-1} also exists. The map needs not be injective on $\overline{\Omega}$ as self-contact is allowed on the body surface (see Figure 2.1).

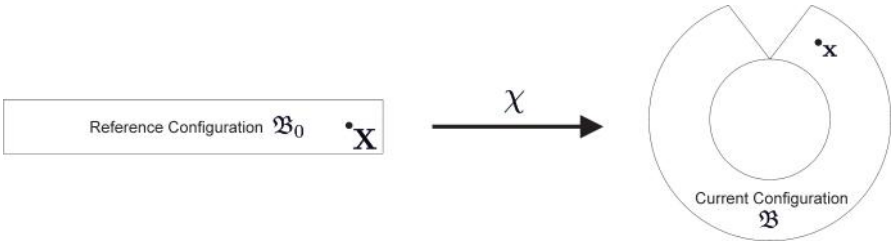

Figure 2.1: Example of deformation with self-contact.

Definition 2.2.4 *(deformation gradient) Changes in length, area and volume are determined by the deformation gradient*

$$\nabla\chi = \mathbf{F} = \begin{bmatrix} \frac{\partial\chi_1}{\partial X_1} & \frac{\partial\chi_1}{\partial X_2} & \frac{\partial\chi_1}{\partial X_3} \\ \frac{\partial\chi_2}{\partial X_1} & \frac{\partial\chi_2}{\partial X_2} & \frac{\partial\chi_2}{\partial X_3} \\ \frac{\partial\chi_3}{\partial X_1} & \frac{\partial\chi_3}{\partial X_2} & \frac{\partial\chi_3}{\partial X_3} \end{bmatrix}. \tag{2.2.2}$$

Then, the deformation of a line is given by $\mathbf{F}$, change in area by $\text{cof}\mathbf{F} = \det(\mathbf{F})\mathbf{F}^{-T}$ and volume by the Jacobian $J = \det\mathbf{F}$.

Definition 2.2.5 *(isochoric deformation) If $J = 1$ then the volume remains constant and the deformation is said to be isochoric.*

Definition 2.2.6 *(homogeneous deformation) If the deformation gradient is uniform (does not depend on material coordinates) then each part of the material*

deforms as the whole does and the deformation is said to be homogeneous.

Definition 2.2.7 *(displacement field) The displacement field is denoted as:*

$$\mathbf{u}(\mathbf{X}) = \mathbf{x} - \mathbf{X}. \tag{2.2.3}$$

Definition 2.2.8 *(displacement gradient) The displacement gradient, more commonly used in engineering, is defined as:*

$$\nabla \mathbf{u} = \mathbf{F} - \mathbf{I}, \tag{2.2.4}$$

or

$$\frac{\partial u_i}{\partial X_j} = \frac{\partial \chi_i}{\partial X_j} - \delta_{ij} = F_{ij} - \delta_{ij}. \tag{2.2.5}$$

Example 2.2.9 *(Simple Shear (SS))*

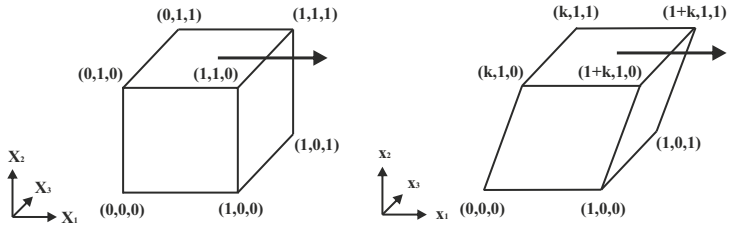

Figure 2.2: Unit cube (left) subject to simple shear (right).

A simple shear (SS) deformation is characterised by [33, 35, 114]:

$$x_1 = X_1 + kX_2 \quad x_2 = X_2 \quad x_3 = X_3, \tag{2.2.6}$$

where k is a positive constant, i.e. the deformation parallel to the X_1 axis is linear. The gradient tensor for this deformation is

$$\nabla \chi = \mathbf{F} = \begin{bmatrix} 1 & k & 0 \\ 0 & 1 & 0 \\ 0 & 0 & 1 \end{bmatrix}. \tag{2.2.7}$$

$\det(\mathbf{F}) = 1$*, so this is an isochoric deformation.*

2.2.2 Deformation tensors

Deformation tensors are measures of an elementary vector after deformation. In finite elasticity, the Cauchy-Green tensors are commonly used: the *left Cauchy-Green* tensor $\mathbf{B} = \mathbf{F}\mathbf{F}^T$ and the *right Cauchy-Green* tensor $\mathbf{C} = \mathbf{F}^T\mathbf{F}$. The *Green-Lagrange* tensor $\mathbf{E} = 1/2(\mathbf{C} - \mathbf{I})$ is commonly used in engineering and in the finite element solver, Finite Elements for Biomechanics (FEBio) [92], employed in this thesis.

In terms of the displacement gradient, the Green-Lagrange deformation tensor is expressed as

$$E_{ij} = \frac{1}{2}\Big(\frac{\partial u_i}{\partial X_j} + \frac{\partial u_j}{\partial X_i} + \frac{\partial u_k}{\partial X_i}\frac{\partial u_k}{\partial X_j}\Big). \tag{2.2.8}$$

In the linear elastic limit, the quadratic terms in the Green-Lagrange tensor are ignored, giving the linear, infinitesimal deformation tensor

$$\boldsymbol{\varepsilon} = (\varepsilon_{ij})_{i,j=1,2,3}, \quad \varepsilon_{ij} = \frac{1}{2}\Big(\frac{\partial u_i}{\partial X_j} + \frac{\partial u_j}{\partial X_i}\Big). \tag{2.2.9}$$

In terms of the deformation gradient $\mathbf{F}$, this is equal to

$$\boldsymbol{\varepsilon} = \frac{1}{2}(\mathbf{F} + \mathbf{F}^T) - \mathbf{I}. \tag{2.2.10}$$

Both Cauchy-Green tensors are symmetric positive definite (SPD) by construction and therefore have strictly positive eigenvalues $\{\lambda_i^2\}_{i=1,2,3}$, where $\{\lambda_i\}_{i=1,2,3}$ are known as the *principal stretch ratios* or *principal stretches*. λ_i can be found by solving the characteristic equation

$$\det(\mathbf{B} - \lambda\mathbf{I}) = \lambda^3 - I_1(\mathbf{B})\lambda^2 + I_2(\mathbf{B})\lambda - I_3(\mathbf{B}) = 0, \tag{2.2.11}$$

where $I_i(\mathbf{B})$ are the *principal invariants* given by:

$$I_1(\mathbf{B}) = \mathrm{tr}(\mathbf{B}), \tag{2.2.12}$$

$$I_2(\mathbf{B}) = \mathrm{tr}(\mathrm{cof}((\mathbf{B})) = \frac{1}{2}(\mathrm{tr}(\mathbf{B})^2 - \mathrm{tr}(\mathbf{B}^2)), \tag{2.2.13}$$

$$I_3(\mathbf{B}) = \det(\mathbf{B}) = J^2 \quad (\text{as } J = \det(\mathbf{F}) = \det(\mathbf{F}^T)). \tag{2.2.14}$$

Note that $I_i(\mathbf{B}) = I_i(\mathbf{C})$, for $i = 1, 2, 3$.

Equivalently, the principal invariants can be expressed as functions of the principal stretches as follows:

$$I_1(\mathbf{B}) = \lambda_1^2 + \lambda_2^2 + \lambda_3^2, \tag{2.2.15}$$

$$I_2(\mathbf{B}) = \lambda_1^2\lambda_2^2 + \lambda_2^2\lambda_3^2 + \lambda_3^2\lambda_1^2, \tag{2.2.16}$$

$$I_3(\mathbf{B}) = \lambda_1^2\lambda_2^2\lambda_3^2. \tag{2.2.17}$$

Remark 2.2.10 *When the right Cauchy-Green tensor is strictly diagonal,* $\mathbf{C} = \mathrm{diag}(\lambda_1^2, \lambda_2^2, \lambda_3^2)$*, where* $\{\lambda_i\}_{i=1,2,3}$ *are the principal stretches, then*

$$\mathbf{E} = \mathrm{diag}\Big(\frac{\lambda_1^2 - 1}{2}, \frac{\lambda_2^2 - 1}{2}, \frac{\lambda_3^2 - 1}{2}\Big). \tag{2.2.18}$$

Theorem 2.2.11 *The Polar Decomposition Theorem states that any deformation gradient* $\mathbf{F}$ *can be decomposed as follows,*

$$\mathbf{F} = \mathbf{RU} = \mathbf{VR}, \tag{2.2.19}$$

where $\mathbf{R}$ *is a rotation tensor, satisfying* $\mathbf{RR}^T = \mathbf{I}$*,* $\mathbf{U}$ *is the right (material) stretch tensor with respect to the reference configuration,* $\mathbf{V}$ *is the left (spatial) stretch tensor with respect to the current configuration, and* $\mathbf{U}, \mathbf{V}$ *are unique SPD tensors.*

For the left and right Cauchy-Green deformation tensors, respectively,

$$\mathbf{C} = \mathbf{F}^T\mathbf{F} = \mathbf{U}^T\mathbf{R}^T\mathbf{R}\mathbf{U} = \mathbf{U}^2, \tag{2.2.20}$$

$$\mathbf{B} = \mathbf{F}\mathbf{F}^T = \mathbf{V}\mathbf{R}\mathbf{R}^T\mathbf{V}^T = \mathbf{V}^2. \tag{2.2.21}$$

We consider $\mathbf{U}$, with strictly positive eigenvalues $\{\lambda_i\}_{i=1,2,3}$ and the corresponding mutually orthogonal and normalised set of eigenvectors forming the columns of a 3×3 matrix $\mathbf{Q} = \{\mathbf{Q}_i\}_{i=1,2,3}$, then the eigenvalue problem is

$$\mathbf{U}\mathbf{Q}_i = \lambda_i\mathbf{Q}_i. \tag{2.2.22}$$

For $\mathbf{C}$, the eigenvalue problem is

$$\mathbf{C}\mathbf{Q}_i = \mathbf{U}^2\mathbf{Q}_i = \lambda_i^2\mathbf{Q}_i, \tag{2.2.23}$$

and thus $\mathbf{C}$ and $\mathbf{U}$ have the same eigenvectors $\{\mathbf{Q}_i\}_{i=1,2,3}$, and the eigenvalues of $\mathbf{C}$ and the square of the eigenvalues of $\mathbf{U}$. Here, $\{\lambda_i\}_{i=1,2,3}$ are the principal stretches (as in (2.2.11)) and $\{\mathbf{Q}_i\}_{i=1,2,3}$ are the *Lagrangian (referential) principal axes*. It is then clear that $\mathbf{C}$ can be written in terms of a triaxial stretch along the principal axes. The *spectral decomposition* of the right Cauchy-Green tensor is a product of the principal stretches and the Lagrangian principal axes,

$$\mathbf{C} = \mathbf{Q}\mathbf{\Lambda}\mathbf{Q}^T, \tag{2.2.24}$$

where $\mathbf{\Lambda} = \mathrm{diag}(\lambda_i^2)$.

In terms of the current configuration, we consider $\mathbf{F} = \mathbf{V}\mathbf{R}$, and substituting $\mathbf{R}\mathbf{R}^T = \mathbf{I}$, we have

$$\mathbf{F} = \mathbf{R}\mathbf{R}^T\mathbf{V}\mathbf{R} = \mathbf{R}\mathbf{U}, \tag{2.2.25}$$

where $\mathbf{U} = \mathbf{R}^T\mathbf{V}\mathbf{R}$. Therefore,

$$\mathbf{C} = (\mathbf{R}^T\mathbf{V}\mathbf{R})^2 = \mathbf{R}^T\mathbf{V}^2\mathbf{R}. \tag{2.2.26}$$

Substituting into the eigenvalue problem,

$$\mathbf{C}\mathbf{Q}_i = \mathbf{R}^T\mathbf{V}^2\mathbf{R}\mathbf{Q}_i = \lambda_i^2\mathbf{Q}_i \tag{2.2.27}$$

$$= \mathbf{R}\mathbf{R}^T\mathbf{V}^2\mathbf{R}\mathbf{Q}_i = \mathbf{R}\lambda_i^2\mathbf{Q}_i \tag{2.2.28}$$

$$= \mathbf{V}^2(\mathbf{R}\mathbf{Q}_i) = \lambda_i^2(\mathbf{R}\mathbf{Q}_i). \tag{2.2.29}$$

By letting $\mathbf{R}\mathbf{Q}_i = \mathbf{q}_i$, we find the eigenvalue problem for $\mathbf{B}$,

$$\mathbf{B}\mathbf{q}_i = \mathbf{V}^2\mathbf{q}_i = \lambda_i^2\mathbf{q}_i, \tag{2.2.30}$$

where $\mathbf{q} = \{\mathbf{q}_i\}_{i=1,2,3}$ are the *Eulerian principal axes* in terms of the current configuration. The spectral decomposition of the left Cauchy-Green deformation tensor is

$$\mathbf{B} = \mathbf{q}\mathbf{\Lambda}\mathbf{q}^T. \tag{2.2.31}$$

2.3 Hyperelastic materials

A hyperelastic material is characterised by a *constitutive law* or *strain energy density function*, $\mathcal{W}(\mathbf{F})$, which depends on the deformation gradient $\mathbf{F}$. It typically involves various *deterministic* model parameters, such as the *constant* elastic moduli for infinitesimal deformations of a material within a given class of functions. The total strain energy over the domain of the reference configuration is then

$$E = \int_\Omega \mathcal{W}(\mathbf{F})dV. \tag{2.3.1}$$

The following assumptions are long-standing principles in isotropic finite elasticity [67, 127, 157]:

The principle of *material objectivity* or *frame indifference* states that the constitutive equations must be invariant under changes of frame of reference. It requires that the scalar strain energy function is unaffected by a superimposed rigid body transformation (which involves a change of position) after deformation, i.e. $\mathcal{W}(\mathbf{R}^T\mathbf{F}) = \mathcal{W}(\mathbf{F})$, where $\mathbf{R} \in SO(3)$ is a proper orthogonal tensor (rotation). Material objectivity is guaranteed by considering strain energy functions defined in terms of invariants.

The principle of *material isotropy*, or *material symmetry* requires that scalar strain energy function is unaffected by a superimposed rigid-body transformation prior to deformation, i.e. $\mathcal{W}(\mathbf{FQ}) = \mathcal{W}(\mathbf{F})$, where $\mathbf{Q} \in SO(3)$. For isotropic materials, the strain energy function is a symmetric function of either the principal invariants $\mathcal{W}(\mathbf{F}) = \mathcal{W}(I_1, I_2, I_3)$ or the principal stretches $\mathcal{W}(\mathbf{F}) = \mathcal{W}(\lambda_1, \lambda_2, \lambda_3)$.

2.3.1 Strain energy density functions

For homogeneous isotropic hyperelastic materials described by a strain energy density function that depends only on the deformation gradient $\mathbf{F}$, we assume the energy to be identically zero at the unstressed state, i.e. $\mathcal{W}(\mathbf{I}) = 0$. By the principle of objectivity, requiring that the strain energy function is unaffected by a superimposed rigid-body deformation, and by the material symmetry, $\mathcal{W}$ can be expressed equivalently in terms of the principal invariants I_1, I_2, I_3, or alternatively, in terms of the principal stretches $\lambda_1, \lambda_2, \lambda_3$. In order to simplify the notation, we write the strain-energy function as $\mathcal{W}$ and infer its argument from the context.

The following isotropic strain energy density functions are used in this thesis, defined in terms of the principal invariants and the deterministic elastic material constants:

- Incompressible neo-Hookean

$$\mathcal{W} = \frac{\mu}{2}(I_1 - 3), \tag{2.3.2}$$

- Compressible neo-Hookean

$$\mathcal{W} = \frac{\mu}{2}\left(I_1 - 3 - \ln I_3\right) + \frac{\lambda}{2}\left(\ln I_3^{1/2}\right)^2, \tag{2.3.3}$$

- Compressible Mooney-Rivlin

$$\mathcal{W} = \frac{C_1}{2}(I_1 - 3) + \frac{C_2}{2}(I_2 - 3) + \frac{\kappa}{2}\left(\ln I_3^{1/2}\right)^2, \tag{2.3.4}$$

- Incompressible Fung

$$\mathcal{W} = \frac{\mu}{2b}\left(e^{b(I_1-3)} - 1\right), \tag{2.3.5}$$

  where b is the stiffening factor.

Transverse isotropy is considered with the addition of a family of extensible fibres embedded in an incompressible Mooney-Rivlin material:

$$\mathcal{W}(I_1, I_2, I_4) = \frac{C_1}{2}\left(I_1 - 3\right) + \frac{C_2}{2}\left(I_2 - 3\right) + \frac{C_4}{4}\left(I_4 - 1\right)^2, \tag{2.3.6}$$

where the fourth invariant $I_4 = (\mathbf{CM})\cdot\mathbf{M}$ and $\mathbf{M}$ is a unit vector denoting direction of transverse isotropy, in the reference configuration.

2.3.2 Stress

Cauchy stress

The *Cauchy (true) stress* represents the internal force per unit of deformed area acting in the deformed solid. For a compressible hyperelastic material, it can be expressed (in terms of the left Cauchy-Green deformation tensor $\mathbf{B}$) as follows [68],

$$\boldsymbol{\sigma} = \beta_0 \mathbf{I} + \beta_1 \mathbf{B} + \beta_{-1} \mathbf{B}^{-1}, \tag{2.3.7}$$

where

$$\beta_0 = \frac{2}{\sqrt{I_3}} \left(I_2 \frac{\partial \mathcal{W}}{\partial I_2} + I_3 \frac{\partial \mathcal{W}}{\partial I_3} \right), \tag{2.3.8}$$

$$\beta_1 = \frac{2}{\sqrt{I_3}} \frac{\partial \mathcal{W}}{\partial I_1}, \tag{2.3.9}$$

$$\beta_{-1} = -2\sqrt{I_3} \frac{\partial \mathcal{W}}{\partial I_2}. \tag{2.3.10}$$

For an incompressible hyperelastic material, the Cauchy stress tensor takes the form

$$\boldsymbol{\sigma} = -p\mathbf{I} + \beta_1 \mathbf{B} + \beta_{-1} \mathbf{B}^{-1}, \tag{2.3.11}$$

where p is known as the 'hydrostatic pressure', or the Lagrange multiplier, for the incompressibility constraints and $I_3 = \det(\mathbf{B}) = 1$ [127, p. 200].

The Cauchy stress can also be written equivalently in terms of the right Cauchy-Green deformation tensor $\mathbf{C}$, as follows,

$$\boldsymbol{\sigma} = 2J^{-1} \mathbf{F} \frac{\partial \mathcal{W}}{\partial \mathbf{C}} \mathbf{F}^T, \tag{2.3.12}$$

where for an isotropic material,

$$\frac{\partial \mathcal{W}}{\partial \mathbf{C}} = \frac{\partial \mathcal{W}}{\partial I_1} \mathbf{I} + \frac{\partial \mathcal{W}}{\partial I_2} (I_1 \mathbf{I} - \mathbf{C}) + \frac{\partial \mathcal{W}}{\partial I_3} I_3 \mathbf{C}^{-1}. \tag{2.3.13}$$

1st Piola Kirchhoff stress

The *1st Piola Kirchhoff stress* tensor represents the internal force per unit of undeformed area acting within the deformed solid. By the Piola transform, it can be expressed in terms of the Cauchy stress as

$$\mathbf{P} = \boldsymbol{\sigma}\text{cof}(\mathbf{F}) = J\boldsymbol{\sigma}\mathbf{F}^{-T}. \tag{2.3.14}$$

Equivalently, in terms of the strain energy density function $\mathcal{W}$ and the right Cauchy-Green deformation tensor $\mathbf{C}$,

$$\mathbf{P} = 2\mathbf{F}\frac{\partial \mathcal{W}}{\partial \mathbf{C}} = \frac{\partial \mathcal{W}}{\partial \mathbf{F}}. \tag{2.3.15}$$

For an incompressible hyperelastic material, the 1st Piola Kirchhoff stress tensor takes the form

$$\mathbf{P} = \frac{\partial \mathcal{W}}{\partial \mathbf{F}} - p\mathbf{F}^{-T}. \tag{2.3.16}$$

2.3.3 Principal stresses

In Section 2.2.2, it was shown that the Cauchy-Green deformation tensors can be written in terms of principal stretches with respect to the principal directions. A similar process can be applied to stresses to give strictly diagonal, triaxial stress tensors, with the diagonal entries known as the *principal stresses*.

Principal Cauchy stresses

Consider the Cauchy stress defined by (2.3.7). Substituting the spectral decomposition for $\mathbf{B}$ from (2.2.31) and likewise a 'decomposition' of $\mathbf{I}$ in terms of $\mathbf{q}$ (as

the identity matrix is indifferent to the change of basis), we obtain

$$\boldsymbol{\sigma} = \beta_0 \mathbf{q}\mathbf{I}\mathbf{q}^T + \beta_1 \mathbf{q}\boldsymbol{\Lambda}\mathbf{q}^T + \beta_{-1}\mathbf{q}\boldsymbol{\Lambda}^{-1}\mathbf{q}^T \tag{2.3.17}$$

$$= \mathbf{q}(\beta_0 \mathbf{I} + \beta_1 \boldsymbol{\Lambda} + \beta_{-1}\boldsymbol{\Lambda}^{-1})\mathbf{q}^T. \tag{2.3.18}$$

Therefore, the Cauchy stress can also be written in terms of the basis $\mathbf{q}$ and takes the form

$$\boldsymbol{\sigma} = \sigma_1 \mathbf{q}_1 \otimes \mathbf{q}_1 + \sigma_2 \mathbf{q}_2 \otimes \mathbf{q}_2 + \sigma_3 \mathbf{q}_3 \otimes \mathbf{q}_3, \tag{2.3.19}$$

where σ_i are the principal stress values of the Cauchy stress tensor, and the tensor product is defined as $\mathbf{q}_i \otimes \mathbf{q}_j = \mathbf{q}_i \mathbf{q}_j^T$.

If the Cauchy stress is written in terms the right Cauchy-Green deformation tensor $\mathbf{C}$, as in (2.3.12), then the principal Cauchy stresses take the form

$$\sigma_i = 2J^{-1}\lambda_i^2 \frac{\partial \mathcal{W}}{\partial \lambda_i^2}, \quad i = 1, 2, 3 \qquad \text{(no summation)}. \tag{2.3.20}$$

By the chain rule, this becomes

$$\sigma_i = 2J^{-1}\lambda_i^2 \frac{\partial \mathcal{W}}{\partial \lambda_i^2} = 2J^{-1}\lambda_i^2 \frac{\partial \mathcal{W}}{\partial \lambda_i}\frac{\partial \lambda_i}{\partial \lambda_i^2} = 2J^{-1}\lambda_i^2 \frac{\partial \mathcal{W}}{\partial \lambda_i}\frac{1}{2\lambda_i} = J^{-1}\lambda_i \frac{\partial \mathcal{W}}{\partial \lambda_i}. \tag{2.3.21}$$

Principal 1st Piola Kirchhoff stress

Recalling that the 1st Piola Kirchhoff stress is related to the Cauchy stress by (2.3.14), we obtain the principal stress values of the 1st Piola Kirchhoff stress tensor,

$$P_i = J\sigma_i \frac{1}{\lambda_i} = \frac{\partial \mathcal{W}}{\partial \lambda_i}, \quad i = 1, 2, 3 \qquad \text{(no summation)}. \tag{2.3.22}$$

The spectral decomposition of the 1st Piola Kirchhoff stress in terms of prin-

cipal stresses is

$$\mathbf{P} = \frac{\partial \mathcal{W}}{\partial \lambda_1}\mathbf{q}_1 \otimes \mathbf{Q}_1 + \frac{\partial \mathcal{W}}{\partial \lambda_2}\mathbf{q}_2 \otimes \mathbf{Q}_2 + \frac{\partial \mathcal{W}}{\partial \lambda_3}\mathbf{q}_3 \otimes \mathbf{Q}_3. \tag{2.3.23}$$

where the second vector in the tensor products now represent the basis of the reference state.

2.3.4 Material responses: Adscititious inequalities

Decades of theory and experiments have suggested that isotropic nonlinearly elastic materials satisfy the following principles, known as the adscititious inequalities [8, 93, 108]:

Baker-Ericksen (BE) inequalities: the greatest principal stress occurs in the direction of the greatest principal stretch. The BE inequalities in linear elasticity reduce to $\mu > 0$ and $\kappa > 0$, where μ is the shear modulus and κ is the bulk modulus. For finite elasticity, the BE inequalities are formally stated as follows:

$$\lambda_i \neq \lambda_j \Rightarrow (\sigma_i - \sigma_j)(\lambda_i - \lambda_j) > 0, \quad i, j = 1, 2, 3, \tag{2.3.24}$$

where $\{\lambda_i\}_{i=1,2,3}$ and $\{\sigma_i\}_{i=1,2,3}$ are the principal stretches and stresses, respectively, and "$\geq$" replaces the strict inequality "$>$" if any two principal stretches are equal.

Considering the form of Cauchy stress given by (2.3.7), the BE inequalities can also be written in terms of the elastic coefficients [8, 93, 108] as follows,

$$\beta_1 \lambda_i^2 \lambda_j^2 - \beta_{-1} > 0, \quad i, j = 1, 2, 3. \tag{2.3.25}$$

Pressure-compression (PC) inequality: each principal stress is a pressure or a tension according if the corresponding principal stretch is a contraction or an

elongation, respectively.

$$\sigma_i(\lambda_i - 1) > 0, \quad i = 1, 2, 3. \tag{2.3.26}$$

In practice, mean versions of the PC condition are used, as follows [113],

$$\sigma_1(\lambda_1 - 1) + \sigma_2(\lambda_2 - 1) + \sigma_3(\lambda_3 - 1) > 0, \tag{2.3.27}$$

or

$$\sigma_1 \left(1 - \frac{1}{\lambda_1}\right) + \sigma_2 \left(1 - \frac{1}{\lambda_2}\right) + \sigma_3 \left(1 - \frac{1}{\lambda_3}\right) > 0, \tag{2.3.28}$$

if not all $\lambda_i = 1$, $i = 1, 2, 3$. In general, BE $\not\Rightarrow$ PC and PC $\not\Rightarrow$ BE [103].

2.4 Boundary value problems

2.4.1 Elastostatic equilibrium

For a deformed body, the equilibrium state can be described by the *Eulerian field equation*

$$-\text{div } \boldsymbol{\sigma} = \mathbf{b}(\mathbf{x}), \tag{2.4.1}$$

where $\mathbf{b}(\mathbf{x})$ is the total body forces acting on the object, for example, due to gravity.

The deformed configuration may not be known, so it can be more convenient to define the equilibrium equation in terms of the reference configuration, giving the *Lagrangian equation*

$$-\text{Div } \mathbf{P} = \mathbf{b_0}(\mathbf{X}), \tag{2.4.2}$$

where $\mathbf{b_0}(\mathbf{X}) = J^{-1}\mathbf{b}(\mathbf{x})$. In the absence of body forces $\mathbf{b_0}(\mathbf{X}) = \mathbf{0}$.

The above governing equations are completed by a constitutive law, depending on material properties (Section 2.3), and supplemented by boundary conditions.

2.4.2 Boundary conditions

The solution of a boundary value problem (BVP) is the displacement field $\mathbf{u}(\mathbf{X})$, such that the equilibrium equation (2.4.2) is satisfied for all $X \in \Omega$, together with the following conditions on the boundary $\partial\Omega = \Gamma$. Here, we consider the relatively disjoint and open subset $\{\Gamma_0, \Gamma_D, \Gamma_N, \Gamma_C\} \subset \Gamma$, such that $\Gamma \setminus (\Gamma_0 \cup \Gamma_D \cup \Gamma_N \cup \Gamma_C)$ has zero area [88, Chapter VI].

Dirichlet (displacement) conditions. The displacement is zero where the object is fixed:

$$\mathbf{u}(\mathbf{X}) = \mathbf{0} \quad \text{on } \Gamma_0. \tag{2.4.3}$$

The displacement is prescribed:

$$\mathbf{u}(\mathbf{X}) = \mathbf{u}_D \quad \text{on } \Gamma_D. \tag{2.4.4}$$

Neumann (stress/traction) condition. External normal force applied at the surface causes a normal stress:

$$\boldsymbol{\tau} = \boldsymbol{\sigma}\mathbf{n} = \mathbf{g}(\mathbf{x}) \quad \text{on } \Gamma_N, \tag{2.4.5}$$

or equivalently, in the reference configuration,

$$\mathbf{P}(\mathbf{X})\mathbf{N} = \mathbf{g_0}(\mathbf{X}) \quad \text{on } \Gamma_N, \tag{2.4.6}$$

where $\mathbf{g}(\mathbf{x})$ and $\mathbf{g_0}(\mathbf{X})$ are the traction forces, and $\mathbf{n}$ and $\mathbf{N}$ are the normal vectors to Γ_N. Here, the subscript 0 refers to a vector with respect to the reference configuration.

Unilateral contact conditions. Acting on Γ_C, the area where contact is possible [88, 112]:

- *Contact displacement condition* (interpenetration of bodies cannot occur):

$$[\mathbf{u}_C] \cdot \mathbf{N} \leq d, \qquad \text{where } [\mathbf{u}_C] = [\mathbf{u}(\mathbf{X}) - \mathbf{u}(\mathbf{X}')] \tag{2.4.7}$$

  where $\mathbf{X}$ and $\mathbf{X}'$ are material points potentially in contact (within different bodies, or the same body for self-contact), $\mathbf{N}$ is the normal vector, $[\mathbf{u}_C]$ is a function of the displacement giving the relative distance between the contacting surfaces, and $d \geq 0$ is a bounded measurable gap between surfaces, which is the distance that cannot be exceeded between potential contacting points.

- *Normal contact pressure* (surface loads cause compressive stress in the material body):

$$\mathbf{P}(\mathbf{X})\mathbf{N} \cdot \mathbf{N} = \mathbf{g}_C(\mathbf{X}) \cdot \mathbf{N} \leq g \tag{2.4.8}$$

  where $\mathbf{g}_C(\mathbf{X})$ is the force acting on the contact surface and $g \geq 0$ is the cohesion parameter, a force that must be overcome to separate (debond) the contacting surfaces.

- *Complementarity condition* (if there is contact pressure, then contact occurs, while no contact results in no contact pressure):

$$([\mathbf{u}_C] \cdot \mathbf{N} - d)(\mathbf{P}(\mathbf{X})\mathbf{N} \cdot \mathbf{N} - g) = 0 \tag{2.4.9}$$

  The complementarity condition is highlighted in Figure 2.3, with $d = 0$ and $g = 0$.

- *Newton's third law* (if two material points map to the same point in space,

equal and opposite reaction forces occur):

$$\mathbf{g}_C(\mathbf{X}) = \mathbf{P}(\mathbf{X})\mathbf{N} = -\mathbf{P}(\mathbf{X}')\mathbf{N}' = -\mathbf{g}_C(\mathbf{X}') \text{ if } \boldsymbol{\chi}(\mathbf{X}) = \boldsymbol{\chi}(\mathbf{X}') \tag{2.4.10}$$

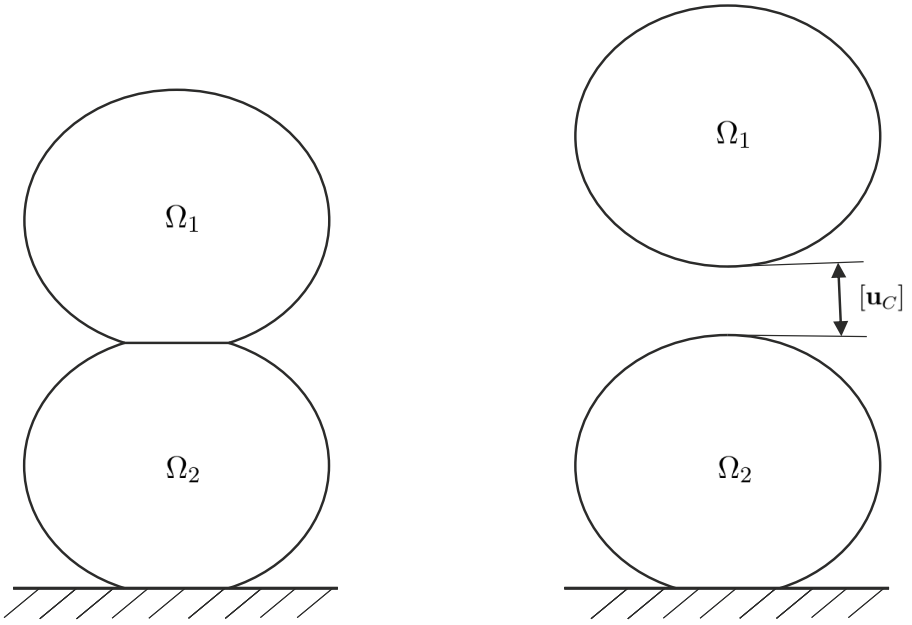

Figure 2.3: The complementarity condition, with two bodies Ω_1 and Ω_2 in contact (left) and not in contact (right). Where the bodies are in contact, a force is possible through the contact interface, whereas when there is a gap $\mathbf{u}_C < 0$ the normal force must be zero.

Here, general unilateral contact conditions are given for surfaces with cohesion and a permissible bounded gap (in which objects are still considered in contact) in the absence of friction [88, 112]. We can define contact in terms of the current state or the reference state. Here, it is stated in terms of the reference state.

The complexity of contact problems modelling structural systems is generally associated with the detection of contacts and openings, and the resolution of non-linear equations for contact [102, 112]. These problems originate in the so-called problem with 'ambiguous boundary conditions' which was first posed by the Italian mathematician Antonio Signorini in 1933 [149].

2.4.3 Variational formulation

To form the variational problem which will be solved numerically, we need to define the kinematically and statically admissible fields (conditions on displacement and force, respectively). For simplicity, we assume the cohesion parameter and the permissible gap to be zero, i.e. $g = 0$ and $d = 0$.

Definition 2.4.1 *(kinematically admissible fields) The vector field* $\boldsymbol{u}$ *is a kinematically admissible displacement if and only if it simultaneously satisfies both the Dirichlet boundary condition and the non-penetrative contact condition. We denote the closed convex set of kinematically admissible fields by:*

$$\mathcal{K} = \{\mathbf{u}' \in W^{1,s}(\Omega;\mathbb{R}^3) \,|\mathbf{u}'(\mathbf{X}) = \mathbf{u}_D \text{ on } \Gamma_D, \tag{2.4.11}$$

$$[\boldsymbol{u}_C] \cdot \boldsymbol{N} \leq 0 \text{ on } \Gamma_C\}, \tag{2.4.12}$$

where $W^{1,s}$ *is a Sobolev space. The condition* $s > 3/2$ *is sufficient for a solution to exist [112].*

Definition 2.4.2 *(statically admissible fields) A tensor field* $\mathbf{F} = \mathbf{I} + \nabla\mathbf{u}$ *is a statically admissible field if and only if* $\partial\mathcal{W}/\partial\mathbf{F}$ *simultaneously satisfies the elastostatic equilibrium condition, Neumann boundary condition and contact conditions (contact pressure and Newton's third law - for every action, there is an equal and opposite reaction). We denote the closed convex set of statically admissible gradient field by:*

$$S = \{\mathbf{F}' \in L^q(\Omega;\mathbb{R}) \,|\mathrm{Div}\frac{\partial\mathcal{W}}{\partial\mathbf{F}'} = 0 \text{ in } \Omega, \tag{2.4.13}$$

$$\frac{\partial\mathcal{W}}{\partial\mathbf{F}'}\boldsymbol{N} = \mathbf{g}_N \text{ on } \Gamma_N, \tag{2.4.14}$$

$$\frac{\partial\mathcal{W}}{\partial\mathbf{F}'}\boldsymbol{N} \cdot \mathbf{N} = \mathbf{g}_C \cdot \mathbf{N} \leq 0 \text{ on } \Gamma_C, \tag{2.4.15}$$

$$\mathbf{g}_C(\mathbf{X}) = -\mathbf{g}_C(\mathbf{X}') \text{ if } \boldsymbol{\chi}(\mathbf{X}) = \boldsymbol{\chi}(\mathbf{X}') \text{ on } \Gamma_C\}, \tag{2.4.16}$$

where L^q is a Lebesgue space with $q > 1$, such that the function is greater than once integrable [112].

2.4.4 Weak formulation (without contact)

If there are no contact boundaries to be resolved and no body forces present, then the variational (weak) form of the potential energy is as follows: Find the displacement $\mathbf{u} = \mathbf{x} - \mathbf{X} \in \mathcal{K}$ such that

$$\int_\Omega \frac{\partial \mathcal{W}}{\partial \mathbf{F}}(\mathbf{X}, \mathbf{F}(\mathbf{u})) : \nabla \mathbf{v} dV = \int_{\Gamma_N} \mathbf{g}_N \cdot \mathbf{v} dA, \tag{2.4.17}$$

with the admissible test field $\mathbf{v} = \mathbf{u}' - \mathbf{u}$, $\mathbf{u}' \in \mathcal{K}$, $\mathbf{g}_N$ is the normal surface traction measured per unit area of the undeformed state. This can be solved by employing the Newton-Raphson Method [88, 109].

2.4.5 Weak formulation with unilateral contact

In the case of unilateral (i.e. non-penetrative, cohesionless, frictionless) contact, and in the absence of body forces, the weak variational form of the potential energy is as follows: Find the displacement $\mathbf{u} = \mathbf{x} - \mathbf{X} \in \mathcal{K}$ such that

$$\int_\Omega \frac{\partial \mathcal{W}}{\partial \mathbf{F}}(\mathbf{X}, \mathbf{F}(\mathbf{u})) : \nabla \mathbf{v} dV = \int_{\Gamma_N} \mathbf{g}_N \cdot \mathbf{v} dA + \int_{\Gamma_C} \frac{\partial \mathcal{W}}{\partial \mathbf{F}} \mathbf{N} \cdot (\mathbf{v} + \mathbf{u}) dA \tag{2.4.18}$$

with the admissible test field $\mathbf{v} = \mathbf{u}' - \mathbf{u}$, $\mathbf{u}' \in \mathcal{K}$, $\mathbf{g}_N$ is the normal surface traction measured per unit area of the undeformed state.

Note the difference between the energy equation without contact (2.4.17) and with contact (2.4.18) is the integral over the contact area. Solving (2.4.18) is more complex and computationally expensive.

2.4.6 Solution schemes

In this thesis, there are two solution schemes used:

1. Semi-inverse method;

2. Finite element method.

Both approaches are briefly described, along with their strengths and weaknesses.

Semi-inverse method

In continuum mechanics, the semi-inverse method is one of the few analytical techniques able to obtain exact solutions. The approach is as follows:

1. Describe:

   (a) material, geometry and if it is static or dynamic,

   (b) deformation,

2. Find:

   (a) material responses (such as stress),

   (b) mechanical behaviour.

Exact solutions provide powerful insights and direct understanding of the non-linear behaviour of solids. The semi-inverse method depends on the deformation being defined a priori. Often we assume homogeneous deformations and substitute into the field equations, hoping that they simplify such that exact solutions to BVPs can be acquired. For complex deformations, the deformation cannot be described and the semi-inverse method cannot be employed. Here, approximate solutions can be obtained by numerical procedure, where it is cast as a variational problem used to generate finite element methods.

Finite element method

The finite element method (FEM) is a numerical method to analyse an object to approximate its deformation and stresses (see [88, 124] and references therein). FEM requires inputs such as geometry, material properties and boundary conditions. The inputs create a variational formulation, such as (2.4.17), that requires numerical integration. The solid is discretised into intervals, known as a mesh. Each element (which could be a 4 node tetrahedral element) in the mesh has a simple function to approximate it's displacement. A large set of linear equations is formulated where the unknowns are the displacement at each node. These linear equations are then solved. FEBio is a Finite element solver specifically designed for biomechanics and as such provides the requires hyperelastic material models and boundary conditions appropriate for modelling biological tissue [92].

In the last decade the finite element method has become more powerful (with increasing computing power) and highly accessible (with simple user interfaces and work flows). It is capable of approximating complex coupled fields problems and produces highly detailed visual outputs with colour maps for stress and displacement. As it is an approximation, there are several factors which affect it's accuracy, such as the density of the mesh and the shape of elements used. It can also suffer from diverging solutions in the minimization algorithm, for which the cause is not always obvious. In contrast to the semi-inverse method, calculating incompressible materials is not possible and the material stiffness is overestimated, which is called "element locking". However, no real material is truly incompressible and the FEM software has a special class of nearly incompressible materials.

Remark 2.4.3 *It is important to note that although physical phenomena are being explored, assumptions and simplifications must be made on the material, the deformation and the boundary conditions.*

Remark 2.4.4 *In non-linear elasticity, multiple solutions can exist, as seen, for example, in the case of the classic problem of the Rivlin cube [116, 137].*

Chapter 3

Debonding of sheared cell walls

3.1 Introduction

Many cellular solids are anisotropic due to the structural distribution of the cells as well as the cell wall material aeolotropic properties. For example, at the millimetre scale, wood is a cellular structure, which can be modelled as a hexagonal prismatic honeycomb, while at the micrometre scale, the cell walls are fibre-reinforced composites, made up of fibres of crystalline cellulose embedded an amorphous matrix of hemicellulose and lignin. Features such as wood density, representing the relative quantity of the cell wall in a given volume of wood tissue, and microfibril angle play important roles in the stiffness and load bearing capacity of this complex structure, and the impact of their variations on the tree biomechanical performance is non-trivial [38, 56, 65, 66, 136]. While wood density varies significantly, the composition and strength of the cell wall is less variable, and phenomena such as cell debonding, commonly known as "cell-peeling", consisting in "the pulling apart of two halves of the cell wall which debond along the central lamella" are responsible for fast and extensive crack propagation in many wood types [7]. The behaviour of wood is captured well by the small strain regime, however analogous behaviours occur in softer plant tissue, where large strains require a non-linear framework.

The relevant scale at which such phenomena occur, though beyond the capacity of the human eye, can be followed by mechanical analysis and mathematical models based on micro-structural evidence [18,89,122]. To effectively capture cell wall debonding, mathematical models that account for the attachment between cells, which in some structures may sufficiently weaken so that cells separate, are required for improved predictions of large distortions and failure in cellular structures. However, obtaining suitable models that are, at the same time, physically plausible, mathematically tractable, and computationally feasible raises many theoretical and numerical challenges.

In this study, we model cellular structures with non-linear hyperelastic cell walls under large shear deformations [110], and incorporate cell wall material anisotropy [33,35] and unilateral contact between neighbouring cells in our structural models [25, 26, 82, 88, 112]. The theoretical and computational challenges raised by these models range from the non-linear deformation of the individual elastic cell walls, to the detection of contact and openings between individual cells. For the cell wall material, we consider one of the most common features of many cellular solids, namely transverse isotropy, whereby the material has one axis of rotational symmetry and the cell wall is stiffer in that direction [76,85,99]. The fibre direction is often aligned close to the vertical axis of the cell [64], with fibre angle varying in-plane, as the cell walls are thin. We analyse the mechanical behaviour of two cuboid cell walls in unilateral, frictionless, contact and subject to generalised shear deformation, and find that, if the walls are in mutual contact in the undeformed state, then gaps can form at the interface between the sheared walls. Although the finite shear deformation of transversely isotropic hyperelastic solids was previously analysed in the literature, a similar study of the simultaneous shear deformation of two transversely isotropic bodies under unilateral contact has not been carried out before. Furthermore, our theoretical and numerical results help to explain the important role of internal cell pressure in some natural cellular

structures (such as apples, potatoes, pears, tomatoes, kiwi) where cell debonding occurs. In Section 3.2, we analyse theoretically the mechanical behaviour of two cuboids of incompressible transversely isotropic Mooney-Rivlin material in unilateral (frictionless) contact and subject to simultaneous generalised shear deformations, and demonstrate the appearance of gaps at the potential contact zone. In Section 3.3, we extend this approach to include time dependence, for a more simple material, such as the isotropic incompressible neo-Hookean material, and find that walls have multiple modes of deformation, which suggests a greater likelihood of debonding than the static case.

3.2 Fibre-reinforced cell walls under shear

The classical problem of generalised shear deformation involves finite plane deformations of a rectangular section of a material in which straight lines parallel to the X_1-axis are displaced relative to one another in the X_2-direction, and the straight lines parallel to the X_2-axis in the undeformed state remain parallel after the deformation. When a cuboid cell wall is subject to generalised shear, the deformation takes the form:

$$x_1 = X_1 + f(X_2), \qquad x_2 = X_2, \qquad x_3 = X_3, \tag{3.2.1}$$

where $\mathbf{X} = (X_1, X_2, X_3)$ and $\mathbf{x} = (x_1, x_2, x_3)$ are the Cartesian coordinates for the reference (Lagrangian, material) and the deformed (Eulerian, spatial) representation, respectively, and f is a function to be determined (see Figure 3.1).

In particular, for the simple shear deformation, (3.2.1) takes the form:

$$x_1 = X_1 + kX_2, \qquad x_2 = X_2, \qquad x_3 = X_3, \tag{3.2.2}$$

where k is a positive constant (see Figure 3.2) [34, 35, 108, 157]. In this case, the

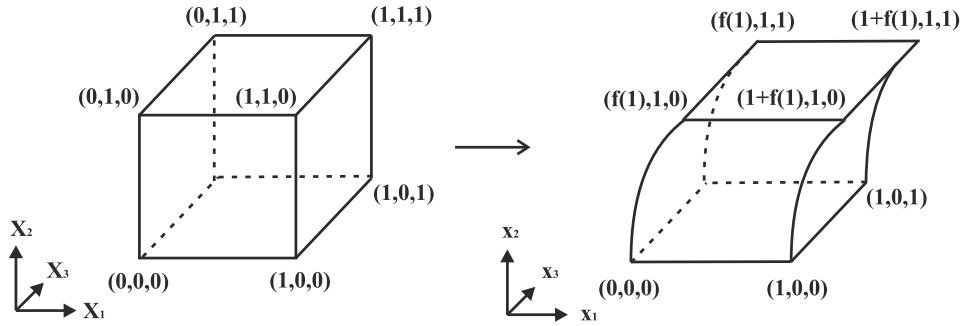

Figure 3.1: Unit cube (left) subject to generalised shear (right).

straight lines parallel to the X_1 or the X_2-axis in the undeformed state remain straight and parallel after the deformation.

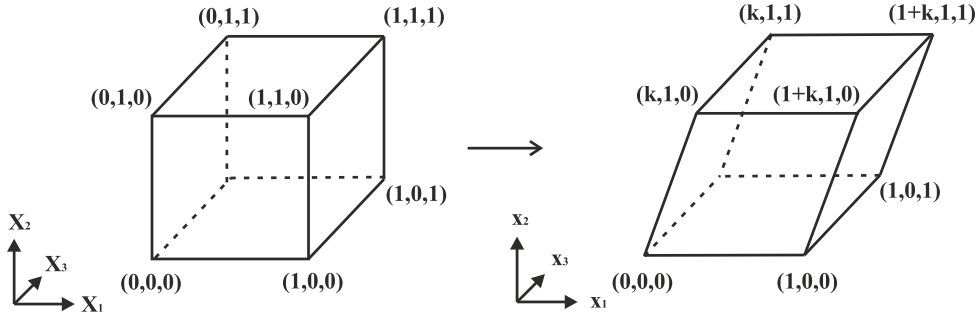

Figure 3.2: Unit cube (left) subject to simple shear (right).

For a cuboid wall of incompressible Mooney-Rivlin material under the deformation (3.2.1), Green & Adkins (1970) [68, pp. 127-129] found that the straight lines parallel to the X_2-axis deform in the shape of a quadratic parabola. In the semi-inverse method where the deformation is defined, the surface tractions need not be known a priori. However, a normal stress may be needed on the inclined faces to enforce this deformation, which is important for defining the boundary conditions in finite element simulations. The surface tractions for simple shear are calculated by Mihai & Goriely (2013) [109] in their paper investigating the Poynting effect in simple shear deformations of Mooney-type materials. The positive Poynting effect in shear is obtained if "the sheared faces tend to spread apart", while the negative Poynting effect occurs if "the sheared faces tend to draw together".

The generalised shear of anisotropic incompressible materials was analysed by

Merodio *et. al* [100] and Destrade *et al.* [36]. Both assume that the material is clamped between two rigid plates and is infinite in length. To account for material anisotropy, the strain energy density function is decomposed into an isotropic and anisotropic part, such that

$$\mathcal{W} = \mathcal{W}_{iso} + \mathcal{W}_{ani}. \tag{3.2.3}$$

They used an incompressible neo-Hookean material for $\mathcal{W}_{iso}$ and a *standard reinforcing model* for $\mathcal{W}_{ani}$, where

$$\mathcal{W}_{ani} = \frac{\gamma}{4}\left(I_4 - 1\right)^2, \tag{3.2.4}$$

with $\gamma > 0$ being a material constant describing fibre stiffness. Merodio *et. al* [100] found that instabilities such as fibre kinking can occur whereas Destrade *et al.* [36] studied two families of fibres embedded int the material and found instabilities can occur from their relative orientation.

Here, we consider two hyperelastic bodies made from an incompressible transversely isotropic material containing one family of extensible fibres embedded in a Mooney-Rivlin material, which is described by the strain energy density function [33, 35, 88]

$$\mathcal{W}(I_1, I_2, I_4) = \frac{C_1}{2}\left(I_1 - 3\right) + \frac{C_2}{2}\left(I_2 - 3\right) + \frac{C_4}{4}\left(I_4 - 1\right)^2, \tag{3.2.5}$$

where I_1, I_2, I_3 are the principal isotropic invariants, I_4 is the anisotropic invariant, and $C_1 > 0$, $C_2 > 0$, and $C_4 > 0$ are constants. If the fibres are contained in the plane (X_1, X_2) and oriented in the direction

$$\mathbf{M} = \begin{bmatrix} \cos\psi \\ \sin\psi \\ 0 \end{bmatrix}, \tag{3.2.6}$$

where $\psi \in [0, \pi/2]$, in the reference configuration, then the stretch of the fibre λ_4 under the deformation (3.2.1) is given by the parameter

$$I_4 = \lambda_4^2 = (\mathbf{CM}) \cdot \mathbf{M} = (f')^2 \sin^2 \psi + 2f' \sin \psi \cos \psi + 1. \tag{3.2.7}$$

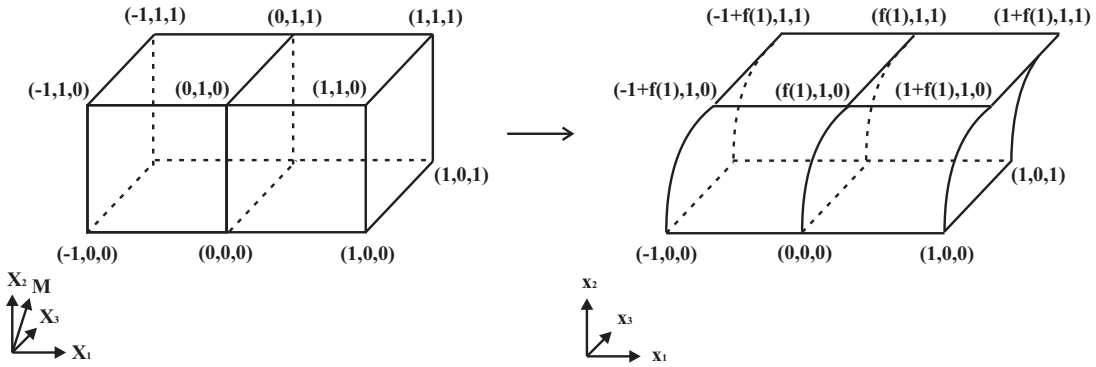

Figure 3.3: Two unit cubes in unilateral contact (left) deformed by generalised shear (right), with the fibre direction $\mathbf{M}$ also shown.

Assuming that the bodies are initially in contact at a common interface, we wish to determine whether they will separate if they are deformed simultaneously by the generalised shear (see Figure 3.3). For the deformation (3.2.1), the deformation gradient is equal to

$$\mathbf{F} = \begin{bmatrix} 1 & f' & 0 \\ 0 & 1 & 0 \\ 0 & 0 & 1 \end{bmatrix}, \tag{3.2.8}$$

where f' is the derivative of f with respect to X_2. The associated left and right Cauchy-Green tensors are, respectively,

$$\mathbf{B} = \mathbf{F}\mathbf{F}^T = \begin{bmatrix} (f')^2 + 1 & f' & 0 \\ f' & 1 & 0 \\ 0 & 0 & 1 \end{bmatrix} \qquad \mathbf{C} = \mathbf{F}^T\mathbf{F} = \begin{bmatrix} 1 & f' & 0 \\ f' & (f')^2 + 1 & 0 \\ 0 & 0 & 1 \end{bmatrix}, \tag{3.2.9}$$

and their principal invariants are

$$I_1 = \text{tr } \mathbf{C} = (f')^2 + 3, \tag{3.2.10}$$

$$I_2 = \text{tr}\,(\text{Cof } \mathbf{C}) = \frac{1}{2}\left[(\text{tr } \mathbf{C})^2 - \text{tr } \mathbf{C}^2\right] = (f')^2 + 3, \tag{3.2.11}$$

$$I_3 = \det \mathbf{C} = 1. \tag{3.2.12}$$

For a deforming body made of a homogeneous incompressible transversely isotropic hyperelastic material described by the strain energy function $\mathcal{W}(I_1, I_2, I_4)$, the Cauchy stress tensor can be represented as

$$\boldsymbol{\sigma} = -p\mathbf{I} + \beta_1\mathbf{B} + \beta_{-1}\mathbf{B}^{-1} + \beta_4\mathbf{FM}\otimes\mathbf{FM}, \tag{3.2.13}$$

where $\beta_1 = 2\partial\mathcal{W}/\partial I_1$, $\beta_{-1} = -2\partial\mathcal{W}/\partial I_2$, and $\beta_4 = 2\partial\mathcal{W}/\partial I_4$ are the material response coefficients, and p is a Lagrange multiplier associated with incompressibility (3.2.12).

In particular, if the material is reinforced with fibres which are oriented in the direction (3.2.6), then

$$\mathbf{FM}\otimes\mathbf{FM} = \begin{bmatrix} (f'\sin\psi + \cos\psi)^2 & f'\sin^2\psi + \sin\psi\cos\psi & 0 \\ f'\sin^2\psi + \sin\psi\cos\psi & \sin^2\psi & 0 \\ 0 & 0 & 0 \end{bmatrix}. \tag{3.2.14}$$

Then, by (3.2.9) and (3.2.14), the components of the Cauchy stress (3.2.13)

take the form

$$\begin{aligned}
\sigma_{11} &= -p + \beta_1 + \beta_{-1} + \beta_1 (f')^2 + \beta_4 \left(f' \sin\psi + \cos\psi\right)^2, && (3.2.15)\\
\sigma_{12} &= (\beta_1 - \beta_{-1}) f' + \beta_4 \left(f' \sin^2\psi + \sin\psi\cos\psi\right), && (3.2.16)\\
\sigma_{22} &= -p + \beta_1 + \beta_{-1} + \beta_{-1}(f')^2 + \beta_4 \sin^2\psi, && (3.2.17)\\
\sigma_{33} &= -p + \beta_1 + \beta_{-1}, && (3.2.18)\\
\sigma_{13} &= \sigma_{23} = 0, && (3.2.19)
\end{aligned}$$

where

$$\beta_1 = C_1, \qquad \beta_{-1} = -C_2, \qquad \beta_4 = C_4 \left[(f')^2 \sin^2\psi + 2f' \sin\psi\cos\psi\right]. \quad (3.2.20)$$

Next, by the equilibrium equation in absence of body forces (2.4.1), it follows that

$$\begin{aligned}
\frac{\partial \sigma_{11}}{\partial x_1} + \frac{\partial \sigma_{12}}{\partial x_2} &= 0, && (3.2.21)\\
\frac{\partial \sigma_{12}}{\partial x_1} + \frac{\partial \sigma_{22}}{\partial x_2} &= 0, && (3.2.22)\\
\frac{\partial \sigma_{33}}{\partial x_3} &= 0, && (3.2.23)
\end{aligned}$$

and substituting (3.2.15)-(3.2.18) in (3.2.21)-(3.2.23) yields

$$\begin{aligned}
\frac{\partial p}{\partial x_1} &= \frac{\partial}{\partial x_2}\left[(\beta_1 - \beta_{-1}) f' + \beta_4 \left(f' \sin^2\psi + \sin\psi\cos\psi\right)\right], && (3.2.24)\\
\frac{\partial p}{\partial x_2} &= \frac{\partial}{\partial x_2}\left[\beta_1 + \beta_{-1}[(f')^2 + 1] + \beta_4 \sin^2\psi\right], && (3.2.25)\\
\frac{\partial p}{\partial x_3} &= 0. && (3.2.26)
\end{aligned}$$

Equation (3.2.26) shows that p is independent of x_3, while equation (3.2.24) implies that p is a linear function of x_1. Next, integration of (3.2.25) with respect

to x_2, gives

$$p(x_1, x_2) = \beta_1 + \beta_{-1} + \beta_{-1}(f')^2 + \beta_4 \sin^2\psi + ax_1 + c, \tag{3.2.27}$$

where a and c are undetermined constants. By (3.2.24) and (3.2.27),

$$\frac{\partial}{\partial X_2}\left[(\beta_1 - \beta_{-1})f' + \beta_4\left(f'\sin^2\psi + \sin\psi\cos\psi\right)\right] = a, \tag{3.2.28}$$

and the constant c remains to be obtained from the contact conditions.

Integrating and substituting β_1, β_{-1}, and β_4 using (3.2.20) yields the following cubic equation in f'

$$C_4(f')^3\sin^4\psi + 3(f')^2 C_4\sin^3\psi\cos\psi + \left(C_1 + C_2 + 2C_4\sin^2\psi\cos^2\psi\right)f' = aX_2 + b, \tag{3.2.29}$$

where b is an arbitrary constant.

In particular, if the fibres align in the X_1-direction in the reference configuration, *i.e.* $\psi = 0$, then $\beta_4 = 0$ and (3.2.29) reduces to a linear equation in f, as in the isotropic case.

We now focus our investigation on the special case when the fibres align in the X_2-direction, *i.e.* $\psi = \pi/2$. In this case, by (3.2.27) and (3.2.20),

$$p(x_1, x_2) = C_1 - C_2 + (C_4 - C_2)(f')^2 + ax_1 + c, \tag{3.2.30}$$

and the stress components (3.2.15)-(3.2.18) take the form:

$$\sigma_{11} = (C_1 + C_2 - C_4)(f')^2 + C_4(f')^4 - ax_1 - c, \tag{3.2.31}$$

$$\sigma_{12} = (C_1 + C_2)f' + C_4(f')^3, \tag{3.2.32}$$

$$\sigma_{22} = -ax_1 - c, \tag{3.2.33}$$

$$\sigma_{33} = (C_2 - C_4)(f')^2 - ax_1 - c. \tag{3.2.34}$$

The equation (3.2.29) simplifies as

$$C_4(f')^3 + (C_1 + C_2)\, f' = aX_2 + b, \tag{3.2.35}$$

where $C_1 > 0$, $C_2 > 0$, and $C_4 > 0$.

Assuming that the fibres are much stiffer than the matrix, so that $C_4 \gg C_1 + C_2$, (3.2.35) becomes

$$C_4 \left[(f')^3 + \frac{C_1 + C_2}{C_4} f' \right] = aX_2 + b. \tag{3.2.36}$$

It can be approximated as

$$C_4(f')^3 = aX_2 + b. \tag{3.2.37}$$

3.2.1 Possible shear deformations

Assuming that, during the deformation, the points of coordinates $(X_1, 0, 0)$ remain fixed and those of coordinates $(1, X_2, 0)$ are deformed into $(1, X_2 + k, 0)$, *i.e.*

$$f(0) = 0 \qquad \text{and} \qquad f(1) = k, \tag{3.2.38}$$

the following two cases are distinguished:

(i) If $a = 0$, then (3.2.37) reduces to

$$f' = \left(\frac{b}{C_4} \right)^{1/3}. \tag{3.2.39}$$

Then, by (3.2.38), this reduces to simple shear

$$f = \left(\frac{b}{C_4} \right)^{1/3} X_2 = kX_2, \tag{3.2.40}$$

with $b = C_4 k^3$.

(ii) If $a \neq 0$, then solving (3.2.37) in f' yields

$$f' = \left(\frac{a}{C_4}\right)^{1/3} \left(X_2 + \frac{b}{a}\right)^{1/3}, \tag{3.2.41}$$

and integration with respect to X_2 gives

$$f = \frac{3}{4}\left(\frac{a}{C_4}\right)^{1/3} \left(X_2 + \frac{b}{a}\right)^{4/3}. \tag{3.2.42}$$

Then, by (3.2.38), $b = 0$ and $a = C_4(4k/3)^3$, *i.e.*

$$f = kX_2^{4/3}. \tag{3.2.43}$$

Note that in the paper [114], the Dirichlet condition $f(1) = k$ was replaced with the Neumann condition $f'(1) = k$, with similar results. The Dirichlet conditions in (3.2.38) are used as they are more general, for shear deformation.

3.2.2 The unilateral contact constraints

Now, we consider two unit cubes made from the same fibre-reinforced material described by the strain energy function (3.2.5) and occupying the reference domains $[-1, 0] \times [0, 1] \times [0, 1]$ and $[0, 1] \times [0, 1] \times [0, 1]$, respectively, with the fibres aligning in the X_2-direction (*i.e.* $\psi = \pi/2$). Assuming that the two cubes are sheared simultaneously by (3.2.1), such that $f(0) = 0$, where f satisfies (3.2.40) for the first cube and (3.2.43) for the second cube, while at the interface between the two cubes, the contact conditions (2.4.7)-(2.4.10) are satisfied such that $d = 0$, we wish to verify if it is possible for gaps to appear at the common interface $(X_1, X_2, X_3) \in \{0\} \times [0, 1] \times [0, 1]$.

Since gaps do not appear when the two bodies deform by the same deformation, we assume $f_1(X_2) = kX_2$ as given by (3.2.40) for the first cube and $f_2(X_2) = kX_2^{4/3}$ as given by (3.2.43) for the second cube, such that $f_1(0) = f_2(0) = 0$. We wish

to verify if, in this case, the contact condition (2.4.7)-(2.4.10) are simultaneously satisfied. The unit normal vector at any point on the curve $(0, X_2)$ is

$$\mathbf{N} = [1, 0, 0]^T. \tag{3.2.44}$$

- The unilateral contact condition (2.4.7) between the deforming cubes is

$$0 \leq [\mathbf{u}_C] \cdot \mathbf{N} = f_1(X_2) - f_2(X_2), \qquad \forall X_2 \in (0, 1), \tag{3.2.45}$$

and, since

$$f_1(X_2) = kX_2 > kX_2^{4/3} = f_2(X_2), \qquad \text{for all } X_2 \in (0, 1), \tag{3.2.46}$$

it follows that the condition (3.2.45) is satisfied.

- The normal forces condition (2.4.8) for each cube is

$$\mathbf{PN} \cdot \mathbf{N} = \sigma_{11} - f_i'\sigma_{12} \leq g, \qquad \forall X_2 \in (0, 1), \qquad i = 1, 2. \tag{3.2.47}$$

Equivalently, by (3.2.31)-(3.2.32),

$$\mathbf{PN} \cdot \mathbf{N} = -C_4(f_i')^2 - ax_1 - c \leq g, \qquad \forall X_2 \in (0, 1), \qquad i = 1, 2, \tag{3.2.48}$$

where $x_1 = X_1 + f_i(X_2)$ for $i = 1, 2$.

Since $X_1 = 0$ at the interface between the two bodies in the reference configuration, the condition (3.2.48) is equivalent to

$$\mathbf{PN} \cdot \mathbf{N} = -C_4(f_i')^2 - af_i - c \leq g, \qquad \forall X_2 \in (0, 1), \qquad i = 1, 2. \tag{3.2.49}$$

For the first cube, $a = 0$ and (3.2.49) takes the form

$$\mathbf{PN} \cdot \mathbf{N} = -C_4 k^2 - c_1 \leq g, \tag{3.2.50}$$

where the constant c_1 remains to be determined.

For the second cube, $a = C_4(4k/3)^3$ and (3.2.49) becomes

$$\mathbf{PN} \cdot \mathbf{N} = -C_4 \left(\frac{4}{3}\right)^2 k^2 X_2^{2/3} - C_4 \left(\frac{4}{3}\right)^3 k^4 X_2^{4/3} - c_2 \leq g, \qquad \forall\ X_2 \in (0,1), \tag{3.2.51}$$

where the constant c_2 is to be determined.

- In the reference configuration, at $X_2 = 0$, $[\mathbf{u}_C]\cdot\mathbf{N} = 0$ and the action-reaction relation (2.4.10) implies

$$c_2 = C_4 k^2 + c_1. \tag{3.2.52}$$

- By the complementarity condition (2.4.9), since by (3.2.46), the relative displacement across the interface between the two cubes is strictly greater than zero for all $X_2 \in (0,1)$, the corresponding normal contact stress must satisfy

$$\mathbf{PN} \cdot \mathbf{N} = g. \tag{3.2.53}$$

For the first cube, (3.2.53) holds if and only if the equality in (3.2.50) is satisfied, *i.e.*

$$c_1 = -C_4 k^2 - g. \tag{3.2.54}$$

For the second cube, by (3.2.52) and (3.2.54),

$$c_2 = -g, \tag{3.2.55}$$

and (3.2.51) simplifies as follows

$$-C_4\left(\frac{4}{3}\right)^2 k^2 X_2^{2/3} - C_4\left(\frac{4}{3}\right)^3 k^4 X_2^{4/3} \leq 0, \qquad \forall\ X_2 \in (0,1). \tag{3.2.56}$$

Note that, by taking $k \to 0$, the equality in (3.2.56) is satisfied to the first order in k, hence (3.2.53) holds for sufficiently small k.

Under the given assumptions and prescribed deformation, the contact conditions (2.4.7)-(2.4.10) with $d = 0$ are simultaneously satisfied for both cubes. If the contact conditions had not been satisfied then we would have concluded that the assumptions and/or prescribed deformation were incorrect, but since they are satisfied, it is possible for gaps to appear at the common interface between the two cubes when these are sheared simultaneously.

3.2.3 The cohesive effect of internal cell pressure

We now turn our attention to the normal stresses (3.2.48) at the external faces $(X_1, X_2, X_3) \in [-1,1] \times [0,1] \times [0,1]$. Assuming that the cells are filled and there is a normal force $g_0 \leq g$ exerted by the cell core on the faces of the cell walls, then, at these faces,

$$\mathbf{PN} \cdot \mathbf{N} = -C_4 (f')^2 - aX_1 - af - c = g_0, \qquad \forall X_2 \in (0,1), \tag{3.2.57}$$

where $X_1 \in \{-1, 1\}$.

For the first cube, the normal stresses (3.2.57) are equal to that at the interface between the two cubes, *i.e.*

$$\mathbf{PN} \cdot \mathbf{N} = -C_4 k^2 - c_1 = g_0. \tag{3.2.58}$$

For the second cube, (3.2.57) takes the form

$$\mathbf{PN}\cdot\mathbf{N} = -C_4\left(\frac{4}{3}\right)^2 k^2 X_2^{2/3} \pm C_4\left(\frac{4}{3}\right)^3 k^3 - C_4\left(\frac{4}{3}\right)^3 k^4 X_2^{4/3} - c_2 = g_0, \forall\, X_2 \in (0,1), \tag{3.2.59}$$

and if $k \to 0$, then these stresses are also equal to the normal stress at the interface between the two cubes to the first order in k.

Consequently, if $g_0 = g$, then the contact conditions are satisfied and we correctly assumed that gaps may appear at the interface between the two cubes. Else if $g_0 < g$, then the complementarity condition is not met and the assumption of gaps appearing between the cell walls does not hold. In particular, when $g = 0$, if the cells are empty, *i.e.* $g_0 = 0$, then the sheared cell walls may debond due to gaps appearing between adjacent cell walls, whereas if the cells are filled and there is internal pressure $g_0 < 0$ exerted on the cell walls, then these walls remain in full contact during the generalised shear deformation.

3.2.4 Surface tractions

The semi-inverse method requires the deformation to be defined a priori and then an exact solution to a BVP can be attempted. The required surface tractions to enforce the deformation do not need to be defined a priori and can depend on the solution to the BVP and the contact conditions. Here we calculate the normal and tangential stresses which must be applied to the faces in the planes $X_1 = -1, 0, 1$, to enforce these deformations.

The normal and tangential stresses on the vertical cell walls in order to ensure the prescribed deformation are given by

$$P_N = \mathbf{N}\cdot(\mathbf{PN}), \tag{3.2.60}$$

$$\mathbf{P}_T = (\mathbf{PN}) - [\mathbf{N}\cdot(\mathbf{PN})]\mathbf{N}, \tag{3.2.61}$$

where $\mathbf{N} = [1, 0, 0]^T$ in the reference configuration. In terms of the Cauchy stress components this becomes

$$P_N = \sigma_{11} - f'\sigma_{12}, \tag{3.2.62}$$

$$\mathbf{P}_T = \begin{bmatrix} 0 \\ \sigma_{21} - f'\sigma_{22} \\ \sigma_{31} - f'\sigma_{32} \end{bmatrix} = \begin{bmatrix} P_{T_1} \\ P_{T_2} \\ P_{T_3} \end{bmatrix}. \tag{3.2.63}$$

From the Cauchy stresses given in (3.2.31)-(3.2.34)

$$P_N = -C_4(f')^2 - ax_1 - c, \tag{3.2.64}$$

$$P_{T_2} = (C_1 + C_2 + ax_1 + c)f' + C_4(f')^3, \tag{3.2.65}$$

$$P_{T_3} = 0. \tag{3.2.66}$$

By (3.2.35) and $x_1 = X_1 + f(X_2)$,

$$P_N = -C_4(f')^2 - a(X_1 + f) - c, \tag{3.2.67}$$

$$P_{T_2} = aX_2 + b + (ax_1 + c)f' = a(X_2 + X_1 f' + ff') + b + cf'. \tag{3.2.68}$$

From Section 3.2.1, we know that for the cube deformed by $f = kX_2$: $a = 0$ and $b = C_4k^3$, and for the cube deformed by $f = kX_2^{4/3}$: $a = C_4(4k/3)^3$ and $b = 0$. The values for c for each cube are defined in (3.2.54)-(3.2.55), resulting from the complementarity condition. Thus, for the first cube

$$P_N = g, \tag{3.2.69}$$

$$P_{T_2} = -gk. \tag{3.2.70}$$

and for the second cube,

$$P_N = g - C_4(4k/3)^2 X_2^{2/3} - C_4(4k/3)^3 X_1 - C_4 k(4k/3)^3 X_2^{4/3}, \tag{3.2.71}$$

$$P_{T_2} = -g(4k/3)X_2^{1/3} + C_4(4k/3)^3 X_2 + C_4(4k/3)^4 X_1 X_2^{1/3} + C_4 k(4k/3)^4 X_2^{5/3}. \tag{3.2.72}$$

Considering small deformation, a first order approximation in k reduces the surface tractions on the second cube to

$$P_N = g, \tag{3.2.73}$$

$$P_{T_2} = -g(4k/3)X_2^{1/3}. \tag{3.2.74}$$

The dependence on X_2 in the second cube's tangential stress is hard to implement in simulation, but essential to enforce the exact deformation prescribed. Without these surface tractions a different deformation would occur and one that that would be less tractable using the semi-inverse method.

3.2.5 Numerical examples

In this section, we illustrate numerically the shear deformation of two hyperelastic cuboid walls in unilateral contact, with and without internal cell pressure and demonstrate it's cohesive effect. The numerical example presented here was realised within the open-source Finite Elements for Biomechanics (FEBio) software environment [92], and in particular, unilateral contact was approximated numerically using the inbuilt FEBio finite element implementation.

First, we consider two cuboid walls of hyperelastic material described by (3.2.75) and occupying the domains $[-1,0]\times[-1,1]\times[0,1]$ and $[0,1]\times[-1,1]\times[0,1]$, respectively, in the undeformed state, as in Figure 3.4. The bodies are allowed frictionless non-penetrative contact on the faces in the plane $X_1 = 0$. Both cuboids are deformed simultaneously by imposing the following Dirichlet boundary conditions:

- $\mathbf{u}_1 = k$ on faces in the plane $X_2 = 1$;
- $\mathbf{u}_1 = -k$ on faces in the plane $X_2 = 0$;
- $\mathbf{u}_2 = 0$ on faces in the planes $X_2 = 0, 1$;
- $\mathbf{u}_3 = 0$ on faces in the planes $X_1 = -1, 0, 1$, $X_2 = 0, 1$ and $X_3 = 0, 1$,

where $\mathbf{u}_i$ is a displacement in the i^{th} direction. The following Neumann boundary conditions are applied:

- $\mathbf{g}_1, \mathbf{g}_2, \mathbf{g}_3 = 0$ on faces in the planes $X_1 = -1, 0, 1$,

where $\mathbf{g}_i$ is a force applied in the i^{th} direction. These surface tractions are derived from (3.2.69)-(3.2.74) where the cohesion parameter $g = 0$. If we did not set $g = 0$ then there would have been a dependence on X_2 which is not possible to implement in FEBio. It is also important to highlight that $\mathbf{g}_1$ and $\mathbf{g}_2$ are defined in the reference state and the normal $\mathbf{N}$ does not change throughout the deformation.

In a second simulation, in addition to the above boundary conditions, an extra Neumann boundary condition is applied:

- $\mathbf{g}_1 = g_0$ on faces in the plane $X_1 = -1, 1$,

where the $g_0 = 0.1$ MPa represents the force from a cell core.

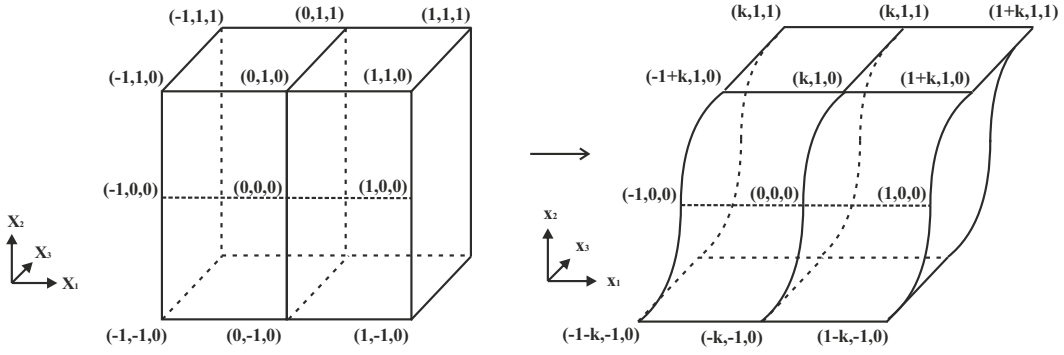

Figure 3.4: Two cuboids in unilateral contact (left) deformed by generalised shear (right). Note the antisymmetry of the deformation with respect to the horizontal line separating each undeformed cuboid into unit cubes.

In the computer simulation, the transverse isotropic hyperelastic material is characterised by the strain energy function [162]

$$\mathcal{W}(I_1, I_2, I_4) = \frac{C_1}{2}(I_1 - 3) + \frac{C_2}{2}(I_2 - 3) + \frac{1}{2}\kappa(\ln J)^2 + \frac{C_4}{4}(I_4 - 1)^2, \quad (3.2.75)$$

where $C_1 = 0.1$ MPa, $C_2 = 0.01$ MPa, $\kappa = 100$ MPa, $C_4 = 1$ MPa, and the fibre direction is parallel to the contact surface [168].

The undeformed and deformed bodies are represented in Figure 3.5A, where gaps across their interface are captured in the deformed state. In Figure 3.5B, for the two bodies, normal pressure g_0 is also applied on the two external side surfaces, causing the bodies to remain in full (active) contact after the deformation.

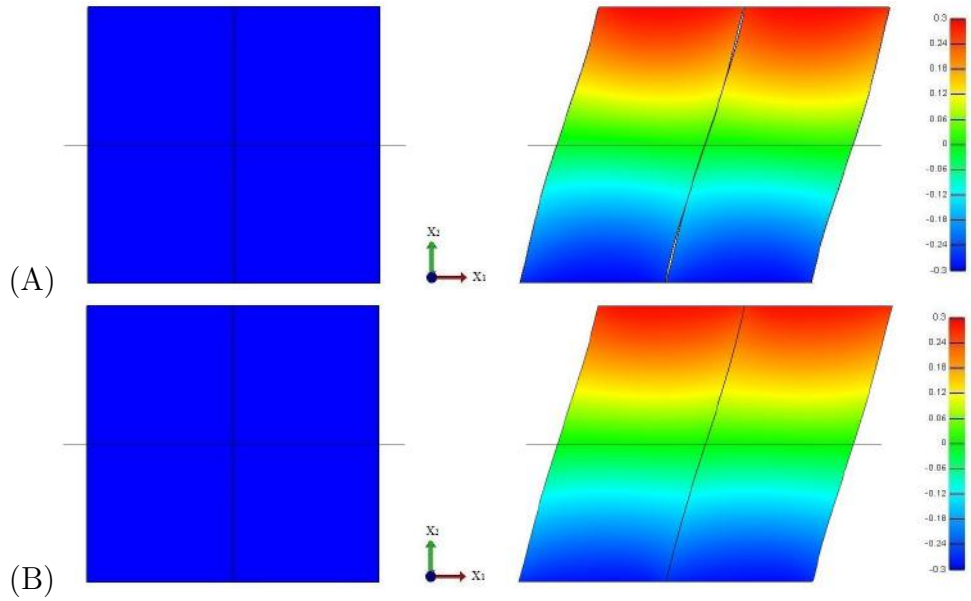

Figure 3.5: Finite element representation of two cuboids of hyperelastic material in mutual unilateral contact, with dimensionless size $1 \times 2 \times 1$ each in the undeformed state (left), and under generalised shear deformation (right), when the lateral external sides are (A) free and (B) subject to uniform normal pressure. The colour bar indicates displacements in the X_1- (horizontal) direction.

For FEM, the contact interfaces are split into discrete sections for which the deformation is approximated at each time step. Solutions in the semi-inverse method which do not satisfy the complementarity conditions could still be approximated by FEM since potential interpenetration would change the deformation in the lo-

cal area - resulting with areas of contact and gaps, both on the same interface. These results support that of the previous section where gaps can occur between bodies under generalised shear. Also, they support the notion that intercellular pressure can work as a cohesive force between pairs of cell walls.

3.3 Isotropic cell walls under time-dependant shear deformation

Now we consider the problem of time-dependant generalised shear deformation where a large number of solutions for the shape of the deformed face f may exist. To maintain tractability of the solutions for shear motion, we restrict attention to the incompressible neo-Hookean material and find general solutions of generalised shear motion and generalised shear. This is presented without contact, but the analysis from the previous section could be applied.

For the deformation of a large-strain and time-dependant body, the Eulerian field equation is

$$\rho\ddot{\mathbf{x}} = \mathrm{div}\boldsymbol{\sigma} + \rho\mathbf{b} \tag{3.3.1}$$

$$\boldsymbol{\sigma} = \boldsymbol{\sigma}^T \tag{3.3.2}$$

where $\mathbf{x} = \chi(\mathbf{X}, t)$ is the motion of the body with respect to time, ρ is the density of the elastic body (constant), $\mathbf{b} = \mathbf{b}(\mathbf{x}, t)$ is body force (assumed to be zero here), $\dot{}$ represents partial derivative w.r.t t and $'$, partial w.r.t X_2 (Newton's notation).

When a cuboid cell wall is subject to generalised shear motion, the deformation takes the form:

$$x_1 = X_1 + f(X_2, t), \qquad x_2 = X_2, \qquad x_3 = X_3, \tag{3.3.3}$$

where $\mathbf{X} = (X_1, X_2, X_3)$ and $\mathbf{x} = (x_1, x_2, x_3)$ are the Cartesian coordinates for the reference (Lagrangian, material) and the deformed (Eulerian, spatial) representa-

tion, respectively, and f is a function to be determined.

The deformation gradient $\mathbf{F}$, the left Cauchy-Green tensor $\mathbf{B}$ and its inverse $\mathbf{B}^{-1}$ is as follows:

$$\mathbf{F} = \begin{bmatrix} 1 & f' & 0 \\ 0 & 1 & 0 \\ 0 & 0 & 1 \end{bmatrix}, \quad \mathbf{B} = \begin{bmatrix} 1+(f')^2 & f' & 0 \\ f' & 1 & 0 \\ 0 & 0 & 1 \end{bmatrix}, \quad \mathbf{B}^{-1} = \begin{bmatrix} 1 & -f' & 0 \\ -f' & 1+(f')^2 & 0 \\ 0 & 0 & 1 \end{bmatrix}. \tag{3.3.4}$$

The Cauchy stress for an incompressible material is

$$\boldsymbol{\sigma} = -p\mathbf{I} + \beta_1\mathbf{B} + \beta_{-1}\mathbf{B}^{-1}, \tag{3.3.5}$$

where p is an undetermined hydrostatic pressure and β_1, β_{-1} are material dependant constants. Then,

$$\boldsymbol{\sigma} = \begin{bmatrix} \beta_1(f')^2 + \beta_1 + \beta_{-1} - p & (\beta_1 - \beta_{-1})f' & 0 \\ (\beta_1 - \beta_{-1})f' & \beta_{-1}(f')^2 + \beta_1 + \beta_{-1} - p & 0 \\ 0 & 0 & \beta_1 + \beta_{-1} - p \end{bmatrix}. \tag{3.3.6}$$

From (3.3.1), in the absence of body forces, the equations of motion must satisfy:

$$\begin{aligned} \frac{\partial \sigma_{11}}{\partial x_1} + \frac{\partial \sigma_{12}}{\partial x_2} &= \rho \ddot{f}, \\ \frac{\partial \sigma_{21}}{\partial x_1} + \frac{\partial \sigma_{22}}{\partial x_2} &= 0, \\ \frac{\partial \sigma_{33}}{\partial x_3} &= 0. \end{aligned} \tag{3.3.7}$$

As generalised shear motion is not a homogeneous deformation, the hydrostatic

stress is not necessarily constant, so the equilibrium equations can be written as

$$\frac{\partial p}{\partial x_1} = (\beta_1 - \beta_{-1})f'' - \rho\ddot{f}, \tag{3.3.8}$$

$$\frac{\partial p}{\partial x_2} = 2\beta_{-1}f'f'', \tag{3.3.9}$$

$$\frac{\partial p}{\partial x_3} = 0. \tag{3.3.10}$$

Restricting our attention to the incompressible neo-Hookean material model, given by

$$\mathcal{W} = \frac{\mu}{2}(I_1 - 3), \tag{3.3.11}$$

we find that (3.3.8-3.3.10) simplifies to

$$\frac{\partial p}{\partial x_1} = \mu f'' - \rho\ddot{f}, \tag{3.3.12}$$

$$\frac{\partial p}{\partial x_2} = 0, \tag{3.3.13}$$

$$\frac{\partial p}{\partial x_3} = 0. \tag{3.3.14}$$

$\frac{\partial p}{\partial x_3} = \frac{\partial p}{\partial x_2} = 0$ implies that p is not dependant on x_2 or x_3, i.e. $p = p(x_1, t)$. Further, if we assume that there is zero net energy in the x_1 direction on the contact boundary Γ_C,

$$\int_{\Gamma_C} \sigma_{11} dx_1 = 0, \tag{3.3.15}$$

then we can conclude that $p = p(t)$.

Surface tractions

The normal and tangential stresses on the vertical cell walls in order to ensure the prescribed deformation are given by

$$P_N = \sigma_{11} - f'\sigma_{12} = \mu - p, \tag{3.3.16}$$

$$\mathbf{P}_T = \begin{bmatrix} 0 \\ \sigma_{21} - f'\sigma_{22} \\ \sigma_{31} - f'\sigma_{32} \end{bmatrix} = \begin{bmatrix} 0 \\ -p \\ 0 \end{bmatrix}. \tag{3.3.17}$$

As it is assumed that $p(t)$ is, at most, a function of time and not on deformation or position, then the tractions could be simply applied in simulation, and holds true for all possible functions f found from solving the BVP.

3.3.1 Solving the boundary value problem

As p is only a function of time, the equilibrium equations reduce to an equation for f, in the form of a one dimensional wave equation,

$$\ddot{f} = \frac{\mu}{\rho} f''. \tag{3.3.18}$$

where $\sqrt{\mu/\rho}$ is the speed of the wave propagation.

The following boundary conditions are used:

$$f(0,t) = 0, \qquad f(L,t) = k, \tag{3.3.19}$$

with initial conditions:

$$f(X_2,0) = f_0(X_2), \qquad \dot{f}(X_2,0) = \dot{f}_0(X_2). \tag{3.3.20}$$

To solve this equation with non-homogeneous boundary conditions, we first

consider a time independent solution $f_E'' = 0$, with boundary conditions $f_E(0) = 0$ and $f_E(L) = k$. The steady state solution is simply

$$f_E = \frac{k}{L} X_2. \tag{3.3.21}$$

Next we introduce $v(X_2, t) = f(X_2, t) - f_E(X_2)$, which is a solution to the problem

$$\ddot{v} = \frac{\mu}{\rho} v'', \tag{3.3.22}$$

with homogeneous boundary conditions

$$v(0, t) = 0, \qquad v(L, t) = 0. \tag{3.3.23}$$

Using separation of variables [69], we find the general solution for $v(x, t)$ has the form

$$v(X_2, t) = \sum_{n=1}^{\infty} [A_n \cos(\omega t) + B_n \sin(\omega t)] \sin(\tau X_2), \tag{3.3.24}$$

where $\omega = (n\pi/L)\sqrt{\mu/\rho}$ and $\tau = n\pi/L$.

Therefore the general solution for $f(X_2, t)$ has the form

$$f(X_2, t) = \frac{k}{L} X_2 + \sum_{n=1}^{\infty} [A_n \cos(\omega t) + B_n \sin(\omega t)] \sin(\tau X_2) \tag{3.3.25}$$

with $\omega = (n\pi/L)\sqrt{\mu/\rho}$ and $\tau = n\pi/L$.

To determine the constants A_n and B_n, consider now the initial conditions,

$$f(X_2, 0) = \frac{k}{L} X_2 + \sum_{n=1}^{\infty} A_n \sin(\tau X_2) = f_0(X_2), \tag{3.3.26}$$

$$\dot{f}(X_2, 0) = \sum_{n=1}^{\infty} B_n \omega \sin(\tau X_2) = \dot{f}_0(X_2). \tag{3.3.27}$$

Using Fourier series, a function $g(x)$ on $0 < x < L$ can be written in the form

$$g(x) = \sum_{n=1}^{\infty} \beta_n \sin(\tau x), \tag{3.3.28}$$

and has constants β_n in the form

$$\beta_n = \frac{2}{L} \int_0^L g(x) \sin(\tau x) dx. \tag{3.3.29}$$

Letting $g(x) = (f_0(X_2) - (k/L)X_2)$ and $A_n = \beta_n$, we find

$$A_n = \frac{2}{L} \int_0^L \left(f_0(X_2) - \frac{k}{L} X_2\right) \sin(\tau X_2) dX_2. \tag{3.3.30}$$

Similarly, letting $g(x) = \dot{f}_0(X_2)$ and $B_n \omega = \beta_n$, we find

$$B_n = \frac{2}{\omega L} \int_0^L \dot{f}_0(X_2) \sin(\tau X_2) dX_2. \tag{3.3.31}$$

3.3.2 The general solution of generalised shear motion

The general solution of generalised shear motion in an incompressible neo-Hookean material is

$$f(X_2, t) = \frac{k}{L} X_2 + \sum_{n=1}^{\infty} [A_n \cos(\omega t) + B_n \sin(\omega t)] \sin(\tau X_2) \tag{3.3.32}$$

with

$$A_n = \frac{2}{L} \int_0^L \left(f_0(X_2) - \frac{k}{L} X_2\right) \sin(\tau X_2) dX_2. \tag{3.3.33}$$

$$B_n = \frac{2}{\omega L} \int_0^L \dot{f}_0(X_2) \sin(\tau X_2) dX_2. \tag{3.3.34}$$

where $\omega = (n\pi/L)\sqrt{\mu/\rho}$ and $\tau = n\pi/L$.

In general there are different modes of oscillations present in generalised time-dependant shear motion. For any mode n and fixed $X_2 = X^*$, $\frac{k}{L} X^* = D_n$ and

$\sin\Big(n\pi X^*/L\Big) = E_n$ where D_n, E_n are constant, giving

$$f_n(X^*,t) = D_n + E_n\Big[A_n\cos\Big(\frac{n\pi t}{L}\sqrt{\frac{\mu}{\rho}}\Big) + B_n\sin\Big(\frac{n\pi t}{L}\sqrt{\frac{\mu}{\rho}}\Big)\Big] \tag{3.3.35}$$

For an increase in t by one second, the argument of cos and sin increases by $(n\pi/L)\sqrt{\mu/\rho}$, so for each mode, there are $(n/2L)\sqrt{\mu/\rho}$ cycles per second. Therefore to increase the frequency of oscillation one can increase the shear modulus μ, decrease the density ρ or decrease the length of the beam L.

Conversely for any mode n and fixed $t = t^*$, $[A_n\cos(\omega t^*) + B_n\sin(\omega t^*)] = C_n$, where C_n is constant, giving

$$f_n(X_2,t^*) = \frac{k}{L}X_2 + C_n\sin\Big(\frac{n\pi X_2}{L}\Big). \tag{3.3.36}$$

$\sin\Big(n\pi X_2/L\Big)$ has n half periods of sin within $0 \le X_2 \le L$, where $n = 0$ recovers simple shear, $n = 1$ is the fundamental tone, $n = 2$ is the first harmonic and $n = 3$, the second harmonic. The possible modes in the shape of the deformed face are given in Figure 3.6 where $L = 1$, $k = 0.5$ and $C_n = 0.05$, for demonstrative purposes.

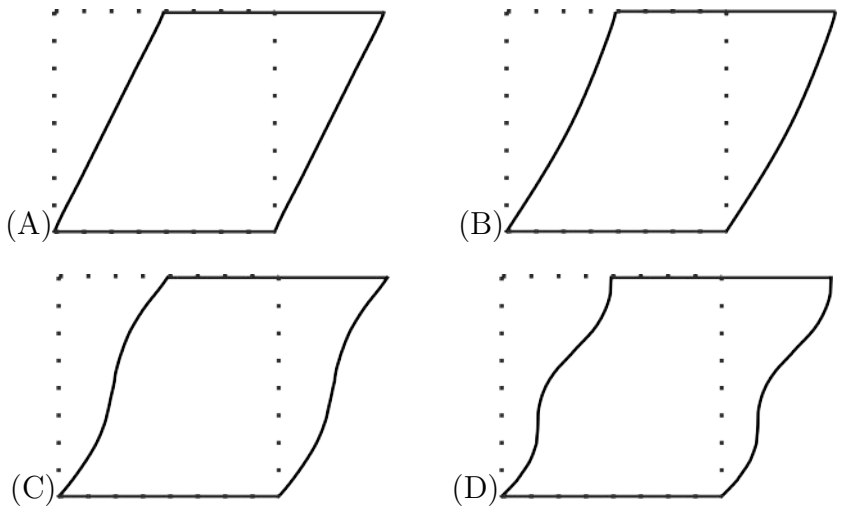

Figure 3.6: Modes of shear deformation in a unit cube (A) simple shear $n = 0$; (B) fundamental tone $n = 1$; (C) first harmonic and $n = 2$; (D) second harmonic $n = 3$.

3.3.3 The general solution of generalised shear

We find the time-independent general solutions by considering $t \to 0$,

$$f_n(X_2, 0) = \frac{k}{L}X_2 + \sin(\tau X_2)\frac{2}{L}\int_0^L \big(f_0(X_2) - \frac{k}{L}X_2\big)\sin(\tau X_2)dX_2. \tag{3.3.37}$$

with $\tau = n\pi/L$. If the initial condition is $f_0(X_2) = \frac{k}{L}X_2$ then the trivial solution is obtained of simple shear, whereas an initial condition of $f_0(X_2) = 0$ gives the solution

$$f_n(X_2, 0) = \frac{k}{L}X_2 + \sin(\tau X_2)\frac{2}{L}\int_0^L \big(-\frac{k}{L}X_2\big)\sin(\tau X_2)dX_2, \tag{3.3.38}$$

$$f_n(X_2, 0) = \frac{k}{L}X_2 + \frac{2k}{\tau^2 L^2}\sin(\tau X_2)(\tau L\cos(\tau L) - \sin(\tau L)), \tag{3.3.39}$$

$$f_n(X_2, 0) = \frac{k}{L}X_2 + \frac{2k}{n^2\pi^2}\sin(\tau X_2)(n\pi\cos(n\pi) - \sin(n\pi)), \tag{3.3.40}$$

giving the general solutions of generalised shear for an incompressible neo-Hookean material,

$$f_n(X_2, 0) = \frac{k}{L}X_2 + (-1)^n\frac{2k}{n\pi}\sin\Big(\frac{n\pi X_2}{L}\Big). \tag{3.3.41}$$

3.4 Summary

Many natural structures are cellular solids at millimetre scale and fibre-reinforced composites at micrometer scale (*e.g.* plant stems, vegetables, fruit). For these structures, physical properties are associated with the mechanical responses of the structural elements under applied forces, and phenomena such as cell separation through debonding of the middle lamella in cell walls is important for perceived behaviour and texture.

To explore such phenomena, we model cellular structures with non-linear hyperelastic cell walls under large shear deformations and incorporate cell wall material anisotropy and unilateral contact between neighbouring cells in our models. Analytically, we show that, for two cuboid walls in unilateral contact and subject

to generalised shear, gaps can appear at the interface between the deforming walls. Although the deformation of transversely isotropic materials has been studied in the literature, they have not been studied in the context of contact mechanics and therefore this research is novel. This work has been published in the Journal of Engineering Mathematics [114].

The semi-inverse method is powerful for obtaining exact analytic solutions. The deformation gradient is assumed and then the material responses and necessary tractions are calculated. Here we found a possible solution which had complex tractions which depend on the X_2 direction, which raises questions about the physical plausibility of the deformation. However, employed in Section 3.3, for time-dependant generalised shear deformation, we consider a simple isotropic incompressible neo-Hookean material and find a plethora of possible behaviours that have not been discussed in the literature, including a general solution for generalised shear. In terms of contact of two cell walls in unilateral contact, the amount of possible forms of f in generalised shear means that gaps are more likely to occur. Choosing two solutions from (3.3.41), the analysis from Section 3.2 could be repeated to find if the solutions are compatible. In addition, if time-dependent solutions were considered, then the frequency of oscillation can vary, if for example the values of μ differ slightly.

In these works on fibre reinforced materials, the fibre angle is deterministic and the maximum and minimum are considered ($\pi/2$ and 0), whereas the fibre direction in a real cell wall is stochastic and the mean fibre direction could be anywhere in the range $0 \leq \theta \leq \pi/2$. Stochastic fibre directions (see [97] for details) could be incorporated into these models, but the results may become complex and intractable. The work could be further expanded for compressible materials and for shear with superimposed triaxial stretch. The transversely isotropic case is currently limited to the case where fibres are much stiffer than the isotropic matrix and this 'middle ground' could be explored further, where $\mathcal{O}(C_4) \approx \mathcal{O}(C_1 + C_2)$.

Chapter 4

Debonding of cellular tissue in shear

4.1 Introduction

Cell separation through debonding of the middle lamella in cell walls is key in explaining the property or behaviour of fruit and legumes during maturation, storage or cooking, and is decisive for the quality of food products [81,91,145]. Fruit tissue is a hydrostatic structure in which individual fluid-filled cells provide resistance to compressive forces, and the fluid pressure may also influence the elastic properties of the cell walls [29, 103]. Physical evidence suggests that the firmness of fruit (apple, pear, tomato) decreases during pre-harvest ripening, when the cell walls of the fruit tissue become softer, and continues to decrease in post-harvest storage due to the loss of cell-to-cell contact, even though the stiffness of the cell walls increases [5,14,168]. Ripening also involves a reduction in turgor pressure, and other physiological and mechanical factors, such as changes in cell size, wall thickness, and composition, may also contribute to changes in the strength and elasticity of the cell walls. For example, during cool storage, cells from high-maturity fruit tend to lose intercellular cohesion but maintain cell wall integrity, while cells from low-maturity fruit tend to maintain relatively high cell-cell cohesion but the strength

of the cell wall declines, so the cells are easily ruptured [53, 70]. Cellular pressure also decreases after harvest which causes cell wall relaxation and could accelerate the process of loss of cohesion. However, both the cell wall strength and the intercellular cohesion decline as fruit enter the over-ripe stage [19].

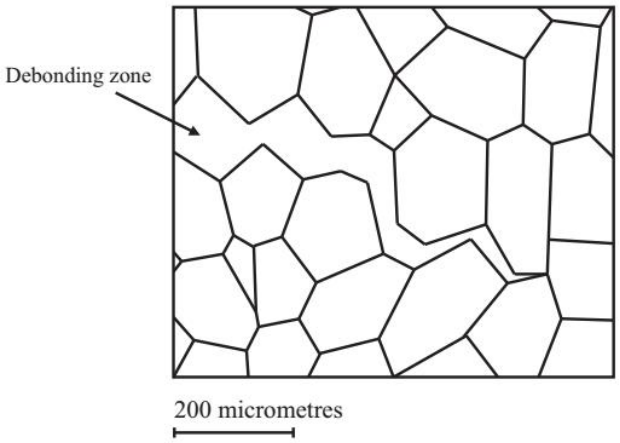

Figure 4.1: Example of debonded fruit cells, leaving cells with their cell walls intact at the fracture surface, or debonding zone.

We extend our analysis from the previous chapter to the investigation of finite element models of periodic structures with hexagonal cells, and find that, when the structures are sheared, gaps appear between adjacent cell walls, causing extensive cell separation diagonally across the structure. To overcome difficulties in the resolution of non-linear equations for contact, we extend the successive deformation decomposition procedure proposed in [111], where seamless cellular structures were treated, to structures with non-penetrative intercellular contact as follows: (i) first, a continuous deformation is computed for the entire structure, as in a compact elastic solid, where only the external boundary conditions and cell-cell pressures are imposed, while the cells remain in mutual contact; (ii) then, for the predeformed structure, the micro-structural properties at individual cell level, such as the unilateral contact between cell walls are taken into account. For the computer simulations, the two-step procedure proved significantly faster and more accurate than when the external boundary conditions and contact constraints were imposed simultaneously in a single step.

Next, we address the question as to what is the influence of the cell-cell cohesion on the intercellular contact where debonding is possible? To answer this question, we impose uniform normal pressure on the contacting cell walls, and find that separation is less likely between cells with high cell pressure than between cells where the internal pressure is low. This is in agreement with physical observations that, under applied force, tissue from high-maturity fruit (apple, pear) breaks down into small clumps of undamaged cells, while cell walls from less mature fruit, which are relatively strongly attached to each other, will rupture [70].

Our computer simulations of cellular bodies with hyperelastic cell walls in mutual non-penetrative contact under large shear deformation, and the two-step strategy which we employ to solve the multibody contact problems more efficiently are novel. In Section 4.4, we present a set of computer models representing groups of hexagonal cells in mutual unilateral contact for which we explore the effects of large-strain deformations.

4.1.1 Summary of FEBio definitions

A number of concepts and definitions are necessary, that are either general for FEM, or particular for FEBio [92], for the implementations in this chapter.

Quasi-static analysis - Structural analysis in FEBio will be achieved in a quasi-static setting, such that deformation happens slowly enough for the system to remain in internal equilibrium. The deformation can equally be considered as instantaneous, with no time-dependence.

Analysis step - One or many analysis steps can be defined, which are collections of all the constraints, such as boundary conditions, loads, contact interfaces, etc. The 'initial' analysis step serves a special purpose since it collects all the constraints that do not depend on a particular step. Additional analysis steps can be added which have constraints specific to that step.

Time step - Within each analysis step, a number of time steps are defined. Not

to be confused with the notion of time, these ordered steps are used for incrementing the constraints, such that, e.g., a boundary condition can be applied in predefined step sizes. For each time step the solution for that step is obtained by a succession of equilibrium iterations using the Newton-Raphson method, where each iteration brings the model (hopefully) closer to the solution for that step. Failure to converge at a particular time step causes a roll-back to an interpolated lower time step. Failure to converge can be caused by a number of reasons, including an element becoming so distorted that it inverts $J \leq 0$, or a convergence tolerance not being reached at a contact interface.

Sliding contact - A sliding contact interface defines a non-penetration constraint between two surfaces. This means that the surfaces are allowed to separate and slide across each other, but are not allowed to penetrate each other. This is equivalent the frictionless unilateral contact conditions defined in Section 2.4.2.

Tied contact - Tied interfaces can be used to tie two non-conforming surfaces together, such that they are attached and do not debond throughout deformation. If both surfaces have compatible nodes and have the same material defined, then they can be considered as deforming together as one continuous material.

4.2 Problem formulation

Computationally, we construct finite element models in FEBio [92] with uniform cells consisting of non-linear hyperelastic cell walls with uniform cell wall thickness, which surround cellular inclusions [103,104]. Adjacent cells are bound together via intercellular pressure [67,73,127] and unilateral contact between cells [88,112,114]. The cell inclusions are represented as an elastic solid with low elastic modulus and zero initial stress. The pressure from the cell core (in the undeformed state) are represented as pressure loads on the internal cell walls. Tissues are subjected to shear of magnitude $\mathbf{u}_X$ (displacement in the X direction) and gaps are created between cells, which are measured and used to quantify debonding.

4.2.1 Geometry and mesh

Within fruit tissues, cells are arranged randomly, as demonstrated in Figure 4.1. Voronoi tessellations (2D and 3D) are packings that represent the randomised aspect of natural cellular materials. Geometric simplifications, such as uniform cell geometry and packing, allow for ordered and repeatable experiment which can be accurately scaled. In a hexagonal prism (or honeycomb) packing, each cell wall has equal length and the cell is in maximum contact with six neighbouring cells, without intercellular spaces. Hexagonal geometry is often used to approximate cellular structures in analysis [63, 66, 174]. Tetrakaidecahedrons (14 sided stackable polyhedra with all edges equal length) can create 3D space filling packings similar to those found in biologically grown cellular materials [65]. Potato parenchyma packings are nearly isotropic with very few empty voids between cells and tetrakaidecahedral modelling has been found to represent this well [79].

As this is a study on the contact between cells and overcoming some of the computational difficulties, hexagonal prism cell geometry is chosen as each cell only has 6 contact interfaces. The cell core is also hexagonal and is fixed to the surrounding cell wall. We refer to the model size by the number of horizontal cells on the bottom row, by the number of vertical cells, for example 3×3, 4×5 and 5×7. On the top and bottom boundaries, extra tabs are added for the application of boundary conditions. Tabs are shown in Figure 4.2 (left). The geometries are created using open source software OpenSCAD, a programming based 3D modelling program, and then imported into FEBio and meshed using the inbuilt 'tetgen' algorithm. Mesh refinements were carried out to assess deformation convergence and found that the mesh, with elements of size 0.2, is sufficient. Adding further mesh complexity adds to computational time greatly, limits potential model sizes and does not refine the results substantially further.

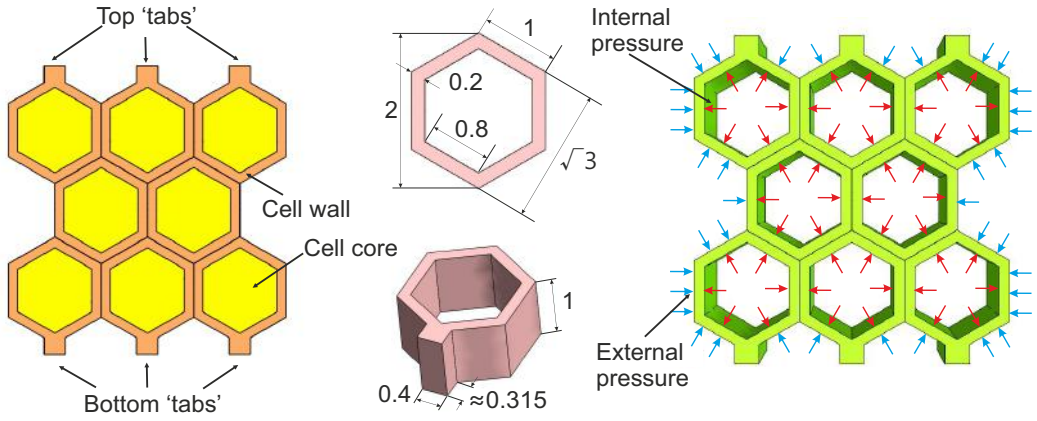

Figure 4.2: Schematic of a 3×3 cell FEM model, indicating the 'tabs' on filled cells where boundary conditions are applied and mesh (left), cell dimensions, which are unitless (middle) and the location of where internal and external pressures are applied, on empty cells (right).

4.2.2 Contact and cohesion

Contact conditions are prescribed on the cell walls which share a common interface. For frictionless, non-penetrative contact, a 'sliding contact interface' is used. Parameter values used for defining this interface can be found in Appendix C. Le Tallec (1994) [88, Chapter VI] provides existence results for the contact formulation (2.4.18) and explains the adaptation to the numerical algorithm to detecting contact. The potential contact surface has a subset where contact actually occurs. A predictor-corrector algorithm predicts the subset and calculates the contact-free equations (2.4.17) excluding this subset. Then it checks for points where the contact conditions (non-penetration, compressive contact and complementarity (2.4.7-2.4.9)) have been violated and adds these points to the contact subset. This process is iterative and ends when the contact subset stays invariant between iterations.

It is possible to create a cohesive contact interface in FEBio by implementing the source code edited by Bronik (2017) [21], but the computational cost is extremely high for multiple contacts. We found a more computationally effective solution to implementing cohesion in our models, as follows: as a cohesive contact interface requires a tensile force over a critical value g to separate faces, we instead

implement balanced normal non-linear surface loads between each pair of contacting walls. In the reference configuration, the pressures are equal and opposite on both sides of the cell wall pairs and thus has zero net force. The result is a force g which must be overcome to separate cell wall pairs. Figure 4.2 (right) shows the application of these surface loads on the internal cell surfaces and the external tissue faces to maintain zero net force. The non-linear pressure load applies in a normal direction to the current state of a surface.

4.2.3 Modelling cell core

The predominant mechanism of cell wall behaviour in empty cells is wall bending but in fluid filled cells this becomes cell wall stretching. Stretching requires more stress than bending and thus increases yield strength of the material [65]. It is common to assume that as cells are compacted together, cell wall bending can be neglected [130, 131]. The effect of having an internal fluid in closed compartments is that when deformation occurs (assuming no rupture of cell walls) the cell's volume is conserved and the densification stage of the stress-strain curve does not happen [103].

As in other studies, fluid viscosity is ignored and the walls are assumed to be impermeable so there is no relaxation of the cell due to fluid migration, which is reasonable in the short time scale where forces are exerted [58, 130]. We also assume initial pressure is equal in all cells.

In [130], the stress in a deformed cell wall of a pressurised cell is decomposed as the sum of (a) the stress in the undeformed cell wall of the pressurised cell and (b) the stress of the deformed cell wall in the unpressurised cell. Similarly here, the cell inclusions are represented in two ways: (a) as a prescribed normal pressure force acting on the surface of the cell walls; (b) as an elastic solid with low elastic modulus and zero initial stress. In Section 3.2.3, it was proved theoretically that modelling cell inclusions by imposing a uniform normal force on the surface of the

cell walls is equivalent to imposing intercellular cohesion.

4.2.4 Material

The cell walls are made from a nearly incompressible isotropic homogeneous Mooney-type hyperelastic material [121, 138],

$$\mathcal{W} = \frac{C_1}{2}(I_1 - 3) + \frac{C_2}{2}(I_2 - 3) + \frac{1}{2}\kappa(\ln J)^2, \tag{4.2.1}$$

where $C_1 = 1$ MPa, $C_2 = 0.1$ MPa and $\kappa = 100$ MPa is the bulk modulus.

We choose to model the fluid also as a homogeneous Mooney-Rivlin material, which is nearly incompressible, with parameters C_1 and C_2 being at least one order of magnitude smaller than the cell wall material, whilst keeping the bulk modulus $\kappa = 100$ MPa for the compressibility restraint.

4.2.5 Boundary conditions

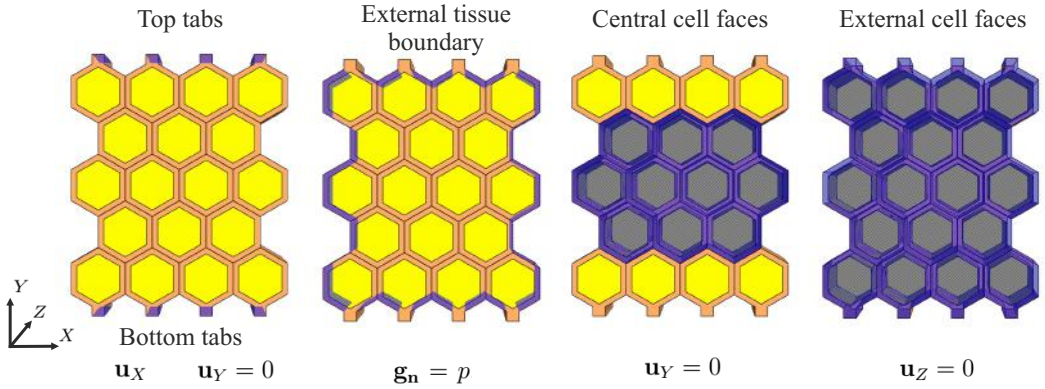

Figure 4.3: 4×5 cell FEM model indicating five groups of geometry faces which have boundary conditions applied. Highlighted in blue are object faces, which are given a group name and the boundary conditions which are applied there.

Shear deformation is applied by the following Dirichlet boundary conditions:

- $\mathbf{u}_X$ shear displacement, on the top tabs ($\mathbf{u}_X^+$) and bottom tabs ($\mathbf{u}_X^-$);
- $\mathbf{u}_Y = 0$ on both top and bottom tabs;

- $\mathbf{u}_Y = 0$ on central cell faces (front and back, excluding boundary layers);
- $\mathbf{u}_Z = 0$ on all external faces and tabs (front and back, including external tissue boundary),

where $\mathbf{u}_i$, $i = X, Y, Z$ denotes displacement in the i^{th} direction. Displacement magnitude is unitless, relative to the cell size, given in Figure 4.2 (middle). Unless otherwise stated, $\mathbf{u}_X$ will imply both $\mathbf{u}_X^+$ and $\mathbf{u}_X^-$ of the same magnitude.

The restrictions $\mathbf{u}_Y = 0$ on cell faces are imposed to restrict rotational deformation of the cells within the tissue and more closely represent simple/generalised shear (and also restrain the solution space). For quantification of parameter interactions, this solution gives tractable results.

Cell pressure and cohesion are applied by the following Neumann boundary conditions:

- $\mathbf{g_n} = p$, normal traction on the contact interfaces and external tissues boundary;
- $\mathbf{g_t} = 0$, tangential traction zero everywhere.

The magnitude of the constant p is measured in MPa. The direction of $\mathbf{g_n}$ is normal relative to the current state of the surface, such that if the angle of the surfaces changes, so does the direction of force.

Traction free boundary conditions are used as an initial assumption (or idealisation) to isolate the shear effect. Later, this assumption will be related and traction will be imposed with cell cohesion for qualitative and quantitative results, with the shear effect already understood.

4.2.6 Preliminary results

For the above geometry and boundary conditions, with shear displacements $\mathbf{u}_X = 0.5$ and $p = 0$ MPa, the simulation results are showed in Figure 4.4B. Here we

can see cells stack into columns (along the diagonal compressive principal axis) and small gaps appear between these columns. These effects propagate from the boundary effects where deformation is generally largest.

We measure the gap between the central cells to quantify debonding, as in Figure 4.4C. The central node positions in the mesh are recorded after deformation, and their relative distance in the X direction is recorded as the *gap size*.

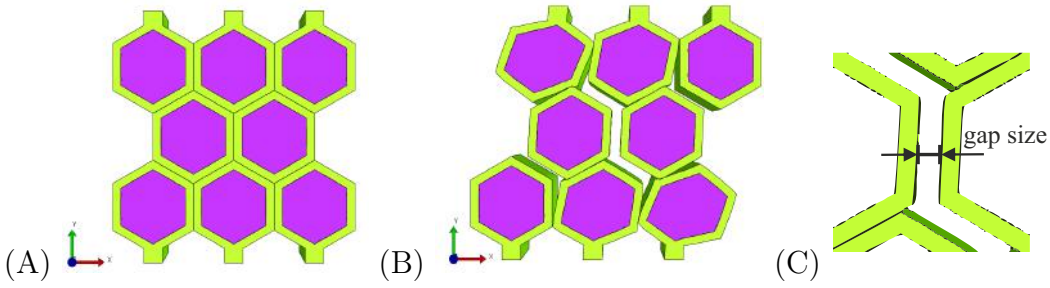

Figure 4.4: Assembly of 3×3 cells in unilateral contact under shear deformation: (A) reference configuration and (B) deformed configuration. (C) shows the *gap size* which is measured for quantification of debonding.

4.3 Improving the modelling procedure

Implementing contact problems in FEBio using a single analysis step results in a suboptimal calculation processes and is prone to divergence problems. We extend and implement methods of increasing computational efficiency, robustness and make the process *scalable*. The idea of scalability, in computing terms, is that the architecture of the calculation process scales well with complexity/size. In the single analysis step implementation, the computation time increases exponentially with the number of cells in the system whereas we aim to use multiple analysis steps to make it scale close to linear in order to handle large numbers of cells competently. In this section we introduce the extended successive deformation decomposition procedure method for contact problems.

Successive Deformation Decomposition Procedure (SDDP)

If $\mathbf{x}' = \boldsymbol{\chi}'(\mathbf{X}) \in \mathbb{R}^3$ describes the first deformation in analysis step (i), and $\mathbf{x} = \boldsymbol{\chi}(\mathbf{X}) \in \mathbb{R}^3$ describes the second deformation in analysis step (ii), written in terms of the $\mathcal{B}_0$ configuration, then the deformation:

$$\mathbf{x}'' = \boldsymbol{\chi}''(\mathbf{x}') = \boldsymbol{\chi}(\boldsymbol{\chi}'^{-1}(\mathbf{x}')) \tag{4.3.1}$$

maps the deformed state $\mathcal{B}'$ to the final configuration $\mathcal{B}$.

Let $\mathbf{F} = d\boldsymbol{\chi}(\mathbf{X})/d\mathbf{X}$, $\mathbf{F}' = d\boldsymbol{\chi}'(\mathbf{X})/d\mathbf{X}$ and $\mathbf{F}'' = d\boldsymbol{\chi}''(\mathbf{X})/d\mathbf{X}$ be the corresponding deformation gradients, such that $\det(\mathbf{F}') > 0$ and $\det(\mathbf{F}'') > 0$, i.e. the mappings $\boldsymbol{\chi}'$ and $\boldsymbol{\chi}''$ are invertible and orientation preserving.

Then, by the chain rule, the following compatible multiplication decomposition holds [103]:

$$\mathbf{F} = \mathbf{F}''\mathbf{F}' \tag{4.3.2}$$

See Figure 4.5 for a diagrammatic representation.

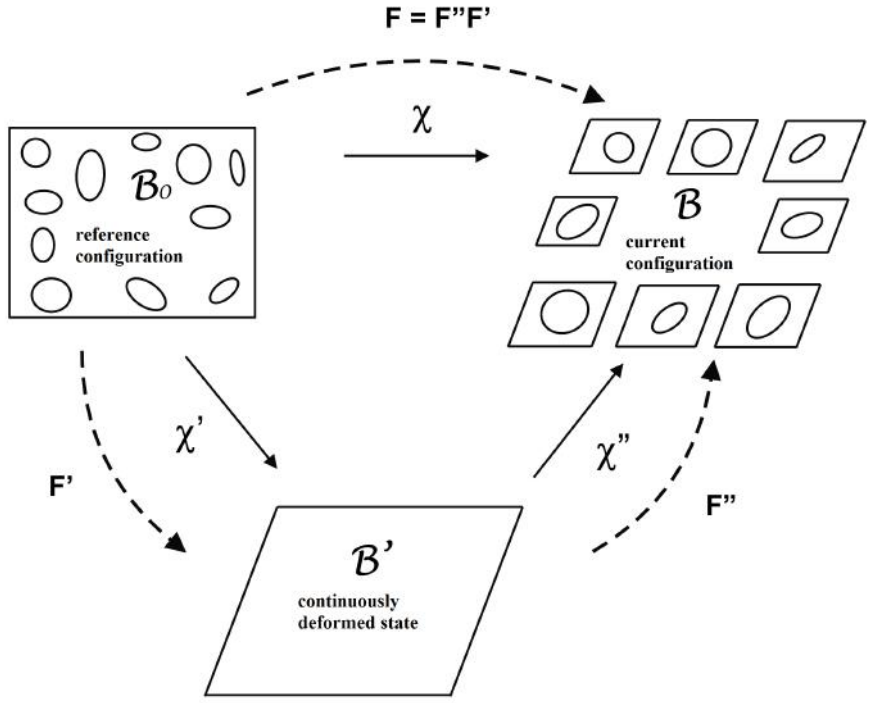

Figure 4.5: Two step Successive Deformation Decomposition Procedure

Application of SDDP in modelling cellular bodies

To improve computational efficiency we employ the SDDP, separating the deformation into successive analysis steps:

- Step (0): In the initial step, impose the boundary conditions $\mathbf{u}_Y$ and $\mathbf{u}_Z$ on the surfaces defined in Section 4.2.5, which are always imposed.
- Step (i): Consider the structure as one continuous, seamless set of cells. This is achieved with *tied contact* conditions between every cell wall pair, such that cells cannot debond and both compressive and tensile forces are transmitted through the interface.
  - (i)a: Incrementally apply the cell and external pressures $\mathbf{g_n}$ upto a prescribed magnitude p.
  - (i)b: Use (i)a as the reference configuration, with $\mathbf{g_n} = p$, and incrementally apply the displacements $\mathbf{u}_X$. This results in a deformed set of cells, without the development of intercellular spaces.
- Step (ii): Finally, consider debonding at the cell interfaces by replacing the tied contact conditions with *sliding contact*, which allows for non-penetrative, cohesionless and frictionless contact. This takes the deformed structure from step (i), with the applied Dirichlet and Neumann boundary conditions, and allows tensile forces to debond neighbouring cell walls. Cohesion is included through application of cell pressures in step (i)a.

The algorithm in step (i) is simple to compute as no iteration sets are added to the process to detect where the contact occurs (as it happens everywhere on the potential contact surface) and therefore forces need to be calculated only once per time step. The change of contact conditions in step (ii) requires a single iteration to calculate the final equilibrium state given by the full contact equation (2.4.18). As a single iteration, this step is performed quickly, as shown in the following section.

An SDDP in a quasi-static deformation means that each step effectively happens simultaneously. The result calculated through SDDP should be the same as one calculated with only sliding contacts, but with a smaller computational cost. SDDP is known to be well determined in a continuous structure [103]. For a discontinuous structure of contacting elastic bodies, the work of Signorini and Fichera can be used to show that this is also well determined [52, 149].

For our simulations of a 5×7 cellular tissue, without cellular inclusions and cohesion, we study the calculation procedures to quantify the power of the successive deformation decomposition procedure.

Analysis of the standard procedure in FEBio

Using the Full-Newton solver, the calculation process is broken down into time steps where the deformation is applied incrementally. The optimal number of time steps was defined in our simulations of shear as 10, but to reach the final deformation 76 steps were used. This indicates that a number of diverging solutions were encountered at the prescribed time steps and rolled back to an interpolated time step.

At each of these time steps, there were an average of 78 equilibrium iterations. At each equilibrium iteration there were exactly 32964 simultaneous equations being solved in the stiffness matrix and the number of non-zero entries changed between each iteration, ranging between $6.89 - 6.98 \times 10^5$.

The calculation process took 3677.18 seconds to execute (a little over one hour). This time is somewhat to do with 73 cell-cell pairs and their contact interfaces (between the 32 cells in the 5×7 tissue) which are evaluated at each time step. The contact interfaces are iteratively calculated at each step to find the points which are in contact and their reaction forces.

The process is parameter sensitive (interpenetration penalty, deformation size, material stiffness), but likelihood of success of the calculations is not bounded by

a set of parameter limits, as small perturbations can fix or break the process. The time at which failure occurs is later in the calculation process, which can be 40 minutes in.

Analysis of the SDDP in FEBio

Step (i) The first step deformed the tissue with tied contacts with optimal number of iteration steps defined as 10, and to reach the final deformation exactly 10 steps were used. This indicates that the computation was relatively stable.

At each time step, there were an average of 6 equilibrium iterations. At each equilibrium iteration there were exactly 32964 equations being solved in the stiffness matrix and the number of non-zero entries was always 5.81×10^5.

Step (ii) The second step took the first step as its reference state and had a change of boundary conditions. As there was no boundary condition to be successively applied, only one iteration step was needed to find a new equilibrium state. The optimal number of iteration steps is therefore 1. Under normal circumstances if there is a problem and the particular step cannot be calculated, a smaller iteration step would be used. However, in this case a smaller step has identical boundary conditions so if it fails to be calculated the first time, then it will fail every time. In some ways, this makes the calculation more sturdy as divergent solutions are found earlier in the calculation process and can be restarted with different $\mathbf{u}_X$ or $\mathbf{g_n}$ values.

In this one time step, there were 34 equilibrium iterations. At each equilibrium iteration there were exactly 32964 equations being solved in the stiffness matrix and the number of non-zero varied at each equilibrium iteration in the range $6.89 - 7.0 \times 10^5$.

The calculation process took 36.87 seconds to execute.

Comparison of calculation methods

Here we will refer to the single step method as *standard* to avoid confusion.

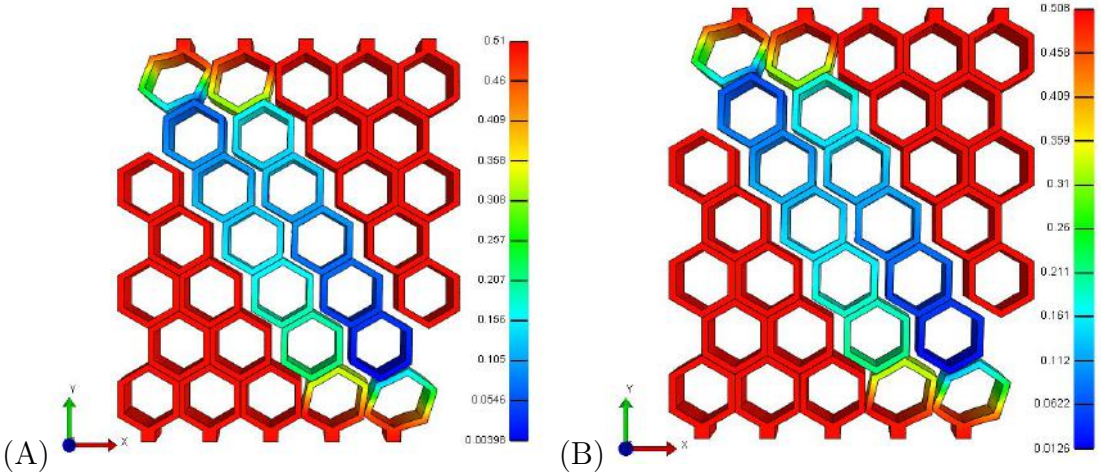

Figure 4.6: Final deformation states of (A) the standard implementation and (B) the SDDP. The colour bar represents total displacement in the X direction.

Comparison of calculation procedures in FEBio				
	Standard	SDDP	Step (i)	Step (ii)
Time steps	76	11	10	1
Equilibrium iterations (avg per step)	78	8.5 (avg)	6	34
Equations being solved (at each equilibrium step)	32964	32964	32964	32964
Non-zeros in stiffness matrix (avg at each equilibrium step)	6.94×10^5		5.81×10^5	6.95×10^5
Calculation time (hours:minutes:seconds)	1:01:17	0:0:37	0:0:20	0:0:17
Gap size	0.232	0.239		

Table 4.1: Comparison of FEBio calculation breakdown

Visual inspection of the colour map of displacements in X, Figure 4.6, shows a clear general agreement with seemingly identical cell position and colour distribution between the normal and SDDP simulations. To quantify the similarity,

a comparison is performed on nodal positions in the final state. The maximum difference in X displacements is 1.8×10^{-2}, with average difference 3.6×10^{-3}. For perspective, the maximum difference 1.8×10^{-2} is approximately 1/10 of the cell wall thickness. The gap size is measured between the initially contacting central nodes between the inner-most middle cells. The gap size differs by 7×10^{-3}.

In terms of calculation time there is a huge difference, from one hour to less than one minute for the SDDP. The distribution of time taken over deformation size is not linear for the normal procedure as it starts fast and progressively gets slower (and may level off). The SDDP reliably takes the same amount of time to calculate.

Calculation reliability is poor for the standard procedure, it can run for a long time and then fail, for example running for 45 minutes then failing at 72% deformation. For the SDDP due to the second step calculating in a single iteration it is clear after the first attempt at solving if it will succeed or fail which means there is a faster turnaround for building models.

Clearly there are strong advantages for using the successive deformation decomposition procedure.

Validation of cohesive cell-cell bonding

A tensile test has been performed to see how well cohesive pressure stops tissue failure under tensile deformation. Failure is quantified by debonding between neighbouring cells, where the distance between any initially contacting nodes exceeds 0.05.

The SDDP is used and the cell walls are made from Mooney-Rivlin material with material constants $C_1 = 1$ MPa, $C_2 = 0.1$ MPa and cohesive pressure $p = 0.1$ MPa.

Tensile deformation is applied by the following boundary conditions:

- $\mathbf{u}_Y^+ = 0.5$ displacement on the top tabs and $\mathbf{u}_Y^- = 0$ on the bottom tabs;

- $\mathbf{u}_X = 0$ on top and bottom tabs;
- $\mathbf{u}_Z = 0$ displacement on all external faces.

Cell pressure and cohesion are applied by the following Neumann boundary conditions:

- $\mathbf{g_n} = p$, normal traction on the contact interfaces and external tissue boundaries;
- $\mathbf{g_t} = 0$, tangential traction zero everywhere.

The direction of $\mathbf{g_n}$ is normal relative to the current state of the surface, such that if the angle of the surfaces changes, so does the direction of force.

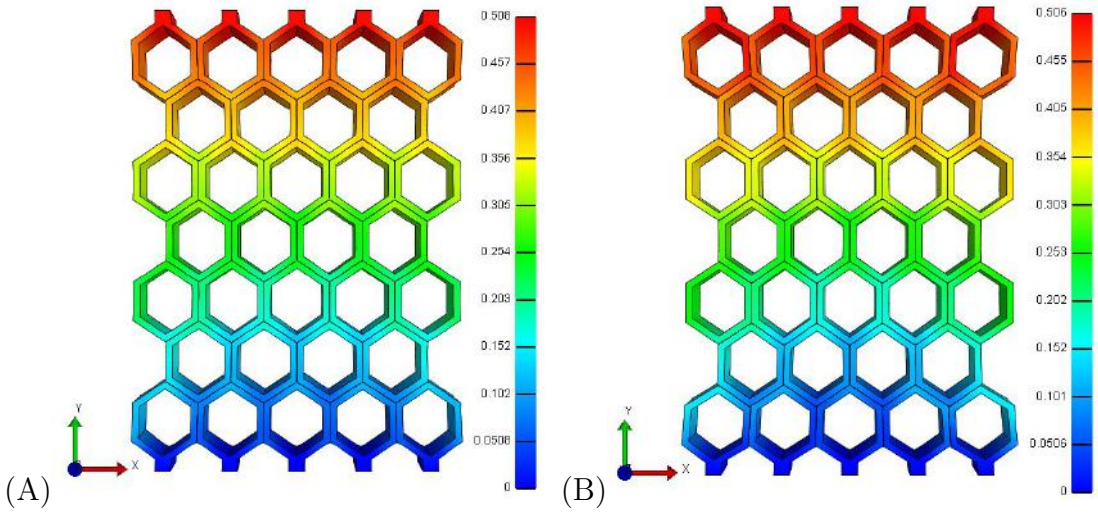

Figure 4.7: Tensile deformation of cellular tissue with intercellular cohesion $p = 0.05$ MPa using SDDP: (A) continuously deformed and (B) separation allowed. The colour bar represents total displacement in the Y direction.

Figure 4.7A shows tissue deformation for cells that have tied contacts and in Figure 4.7B the cells are able to debond, where the high pressure within the cells stop debonding from occurring. For a deformation of $\mathbf{u}_Y^+ = 0.3$, failure occurs for $p < 0.01$ MPa and for $\mathbf{u}_Y^+ = 0.5$, failure occurs for $p < 0.018$ MPa. This supports the results for pressure simulating the effects of cohesive contact interfaces and further validates the usefulness of the SDDP.

4.4 Parameter investigation

4.4.1 Number of cells

The number of cells within the model tissue is explored here. In Figure 4.8 we have 3×3, 4×5 and 5×7 tissues in the deformed state. The boundary conditions are as set out in Section 4.2.5, with $\mathbf{u}_X = 0.5$ and $p = 0$.

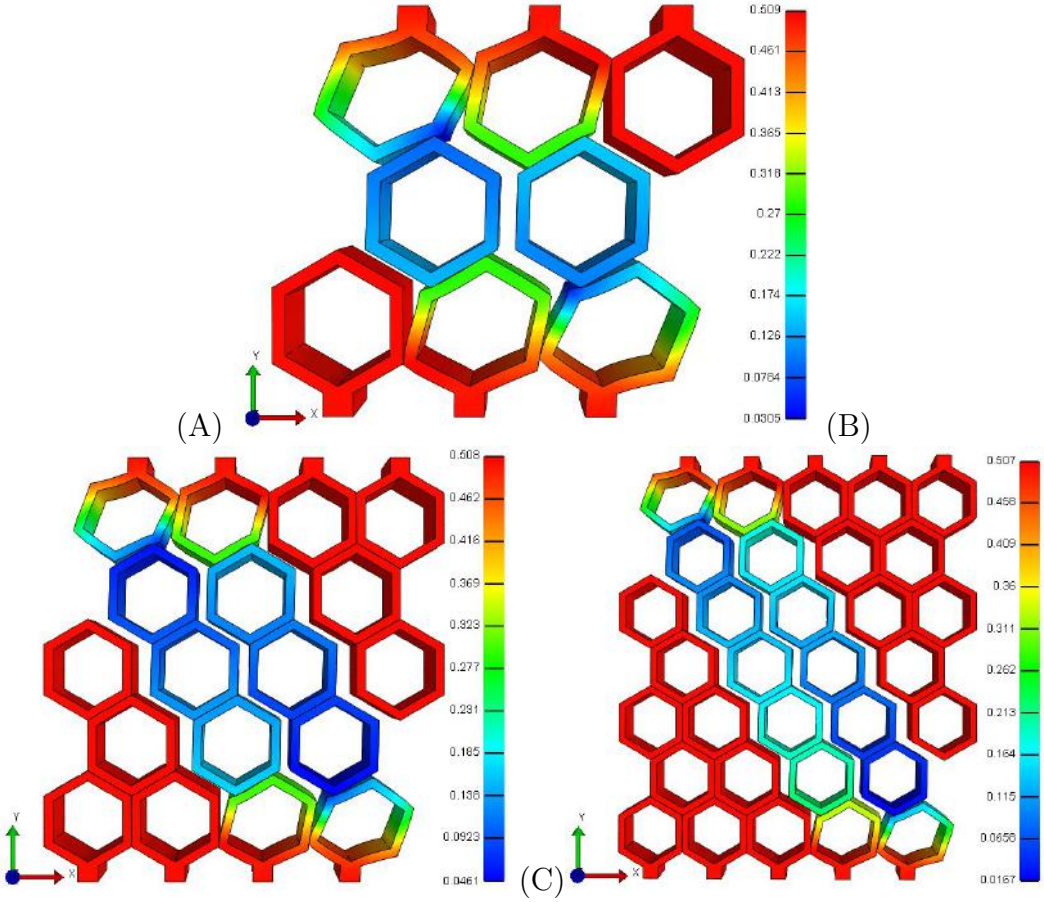

Figure 4.8: Cellular tissues under shear deformation $\mathbf{u}_X = 0.5$: (A)3×3, (B) 4×5 and (C) 5×7. The colour bar represents displacement in the X direction.

In each model the cells are the same size and distribution, the difference being that there are more cells - making the tissue larger. Here the magnitude of the shear deformation is scaled to the size of the cell, not the tissue. Gap sizes are shown in Figure 4.9 for the three tissue scales. Even with a small cell number in the 3×3 model, the gap opening is close to that of the 4×5 and 5×7 models. The main difference between the models is the size of the X deformation possible for simulation before computational failure. The 3×3 model shows deformations up to a magnitude of 0.5, the 4×5 upto 0.8 and the 5×7 upto 1.2.

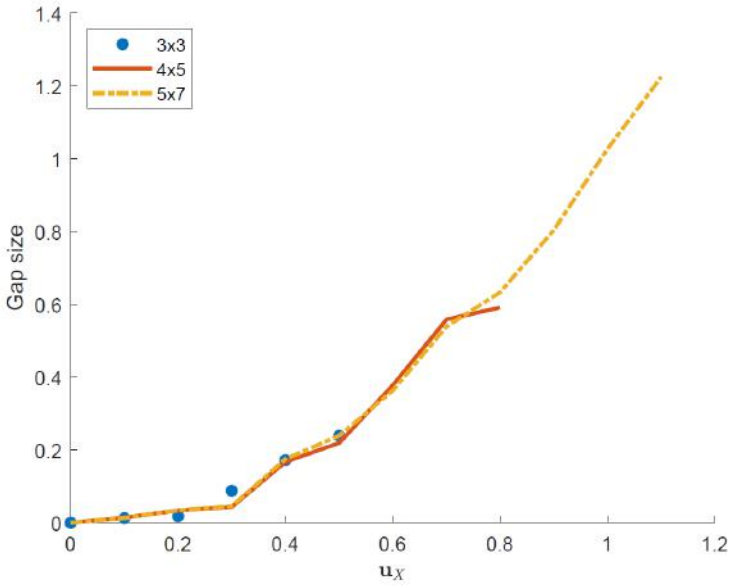

Figure 4.9: Comparison of gap sizes for multiple tissue sizes.

4.4.2 Cell wall material models

We investigate the difference between the Mooney-Rivlin material and comparable a linear elastic material by converting the material parameters ($C_1 = 1$ MPa, $C_2 = 0.1$ MPa and $\kappa = 100$ MPa) to the Young's modulus E and Poisson's Ratio ν, using the following identities,

$$C_1 + C_2 = \mu \qquad E = \frac{9\kappa\mu}{3\kappa + \mu} \qquad \nu = \frac{3\kappa - 2\mu}{2(3\kappa + \mu)} \tag{4.4.1}$$

We now find the linear elastic coefficients for models comparable to previous examples to be:

$$E = 3.29 \text{ MPa} \qquad \nu = 0.49 \tag{4.4.2}$$

Comparing the Isotropic Elastic material model in FEBio the simulation, a deformation of $0 \leq \mathbf{u}_X \leq 0.3$ shows the gap size matching within a tolerance of 10^{-3}. Matching results at small strain is exactly what is to be expected by the definition of the finite and small strain regimes. For larger $\mathbf{u}_X$, the results start to diverge.

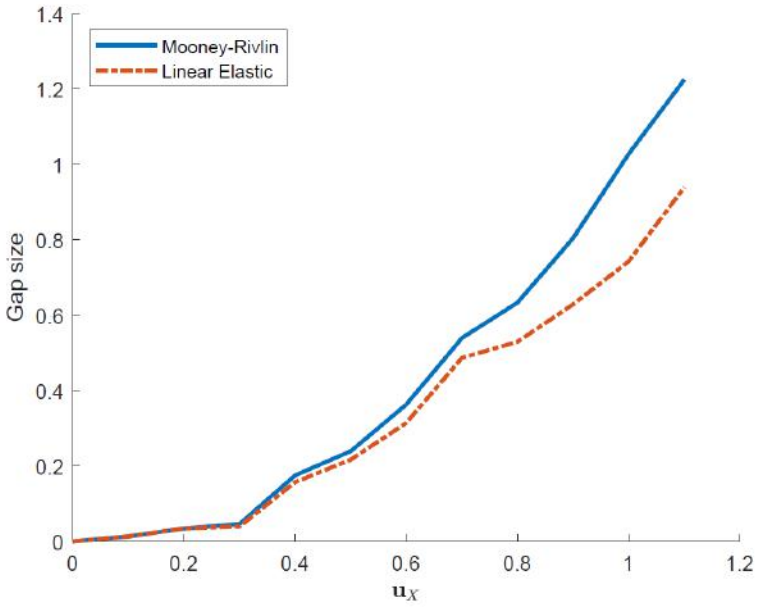

Figure 4.10: Relationship between $\mathbf{u}_X$ and gap size for different materials - hyperelastic Mooney-Rivlin and Linear Elastic, in a 5×7 tissue. This model is not subject to cohesive pressure.

4.4.3 Cohesion

We vary both shear magnitude $\mathbf{u}_X$ and intercellular pressures p on a 5×7 tissue to measure how these affect cell separation.

Figure 4.11 shows a plot of the gap size for $0 \leq \mathbf{u}_X \leq 1.1$ and pressures $0 \leq p \leq 0.015$ MPa. The data clearly shows that increasing pressure delays the initiation of gaps. For zero pressure the rate of increase in gap size seems to follow

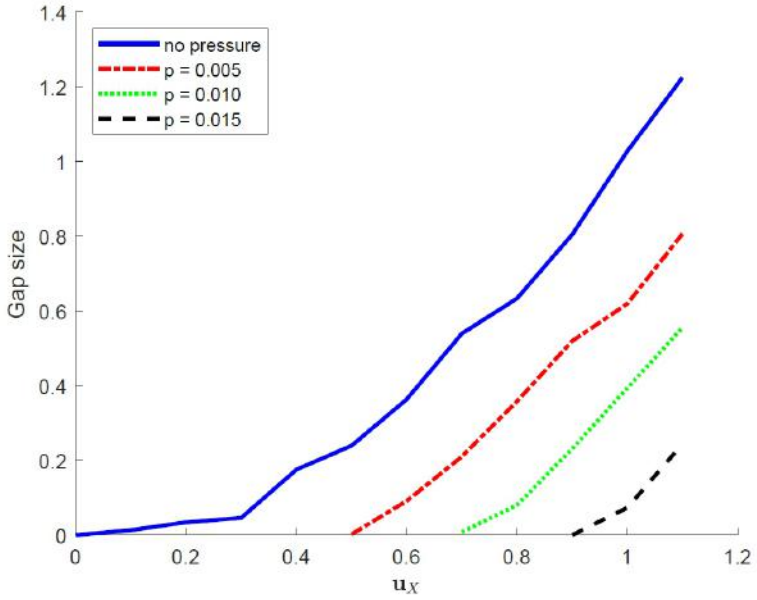

Figure 4.11: Relationship between shear magnitude $\mathbf{u}_X$ and gap size for different cohesive pressures, in a 5×7 tissue.

a non-linear curve. The slope of the gap size seems to be consistent once the gap has been initiated.

Figure 4.12 shows the final deformation state (step (ii)) with $0.4 \leq \mathbf{u}_X \leq 0.8$ and $0 \leq p \leq 0.01$ MPa. It is clear that gaps increase in size with greater deformation (from left to right) and gaps decrease with increased cohesive pressure (from top to bottom). The gap size seems to correlate with large deformation of the corner cells.

4.4.4 Revisited: cell wall with cohesion

Again we investigate the difference between Mooney-Rivlin material and linear isotropic material. Now we also include intercellular cohesion, shown in Figures 4.13 and 4.14.

The gap opening in the linear elastic case initiates at a higher deformation and then grows at a similar rate. The difference in behaviour is similar to that of the higher deformations in the previous linear/Mooney comparison (Figure 4.10).

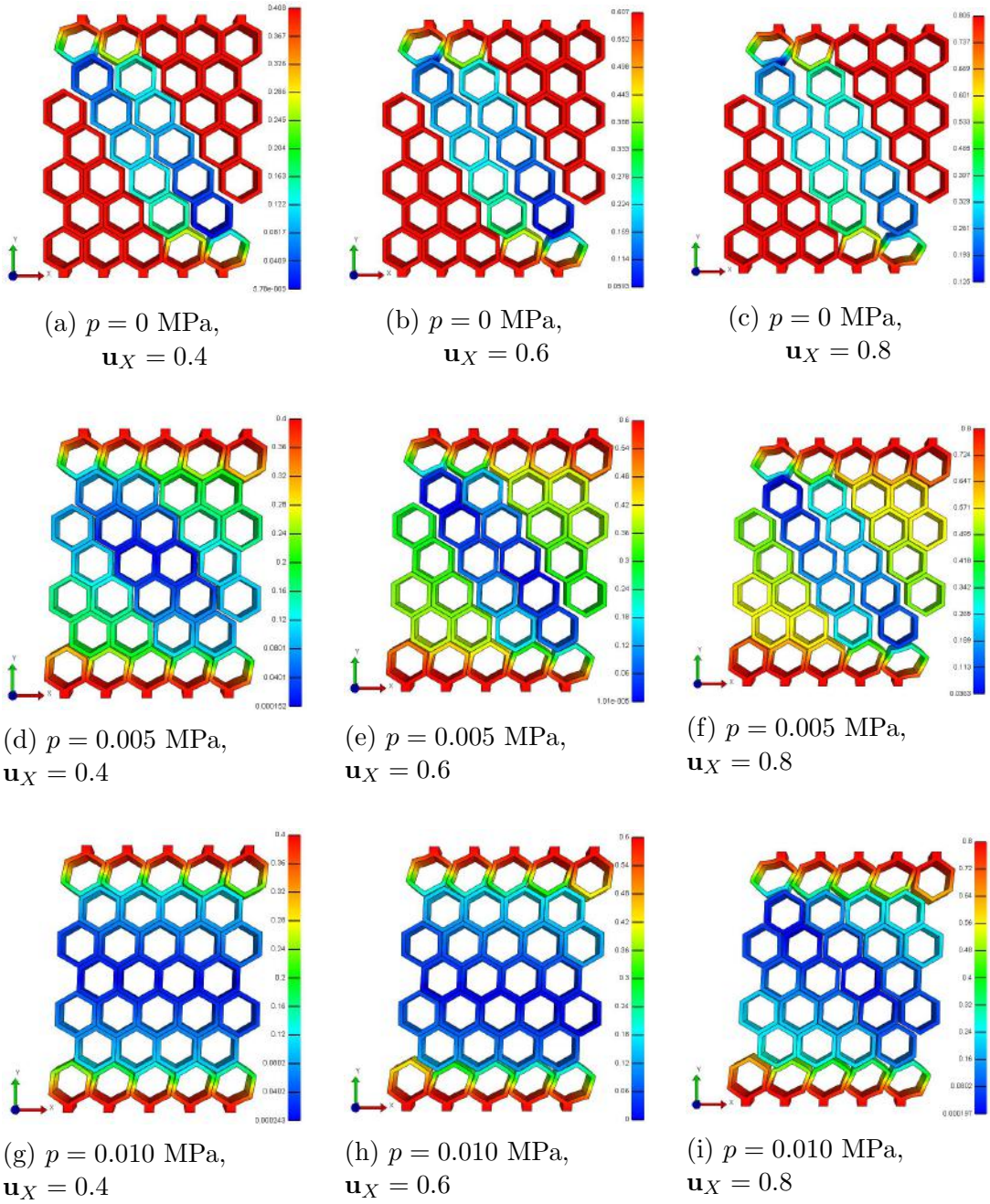

(a) $p = 0$ MPa, $\mathbf{u}_X = 0.4$

(b) $p = 0$ MPa, $\mathbf{u}_X = 0.6$

(c) $p = 0$ MPa, $\mathbf{u}_X = 0.8$

(d) $p = 0.005$ MPa, $\mathbf{u}_X = 0.4$

(e) $p = 0.005$ MPa, $\mathbf{u}_X = 0.6$

(f) $p = 0.005$ MPa, $\mathbf{u}_X = 0.8$

(g) $p = 0.010$ MPa, $\mathbf{u}_X = 0.4$

(h) $p = 0.010$ MPa, $\mathbf{u}_X = 0.6$

(i) $p = 0.010$ MPa, $\mathbf{u}_X = 0.8$

Figure 4.12: 5×7 cellular tissue under varying shear deformation ($\mathbf{u}_X$ fixed in columns) and varying cohesive pressure (p fixed in rows). The colour bar represents total displacement in the X direction.

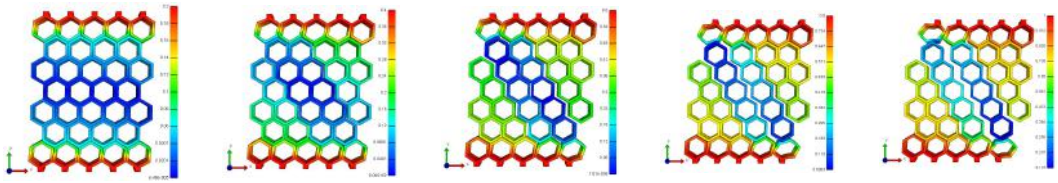

(a) $X = \pm 0.2$ (b) $X = \pm 0.4$ (c) $X = \pm 0.6$ (d) $X = \pm 0.8$ (e) $X = \pm 1.0$

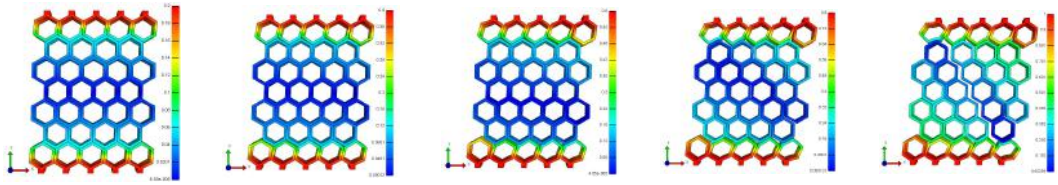

(f) $\mathbf{u}_X = 0.2$ (g) $\mathbf{u}_X = 0.4$ (h) $\mathbf{u}_X = 0.6$ (i) $\mathbf{u}_X = 0.8$ (j) $\mathbf{u}_X = 1.0$

Figure 4.13: 5×7 cellular tissue under varying shear deformation $\mathbf{u}_X$ for Mooney-Rivlin (top row) and Linear Elastic material (bottom row). The colour bar represents total displacement in the X direction.

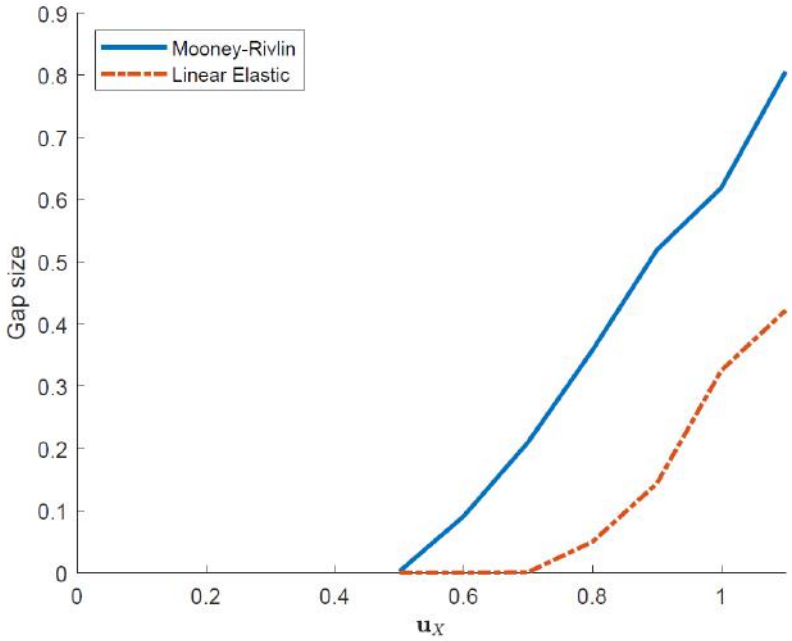

Figure 4.14: Relationship between shear magnitude $\mathbf{u}_X =$ and gap size for different materials in a 5×7 tissue, with cohesive pressure of $p = 0.005$ MPa.

4.4.5 Cell core

We now consider the soft elastic inserts embedded within the cell walls and study the effect of its relative stiffness compared to the cell walls.

Figure 4.15 shows very similar deformation to that of the empty cells. The volume restriction and elasticity of the inclusion has decreased gap size noticeably at this deformation. Figure 4.16 shows a comparison of the gap sizes for inclusions which have Mooney-Rivlin material parameters $10\times, 20\times, 40\times$ and $1000\times$ smaller than the cell walls. The gap size of the cellular tissue with empty cell contents is also shown. The first part of the deformation shows all gap sizes growing at the same rate, but the rate of increase in gap size is delayed with the presence of an inclusion. The closer the inclusion parameters are to the cell wall material, the later the onset of this gap increase. After the gap increase begins, it happens at a much faster rate than the empty case. The inclusion material $1000\times$ smaller shows that after this increase, the size of gap and the rate at which it expands converge with the empty structure.

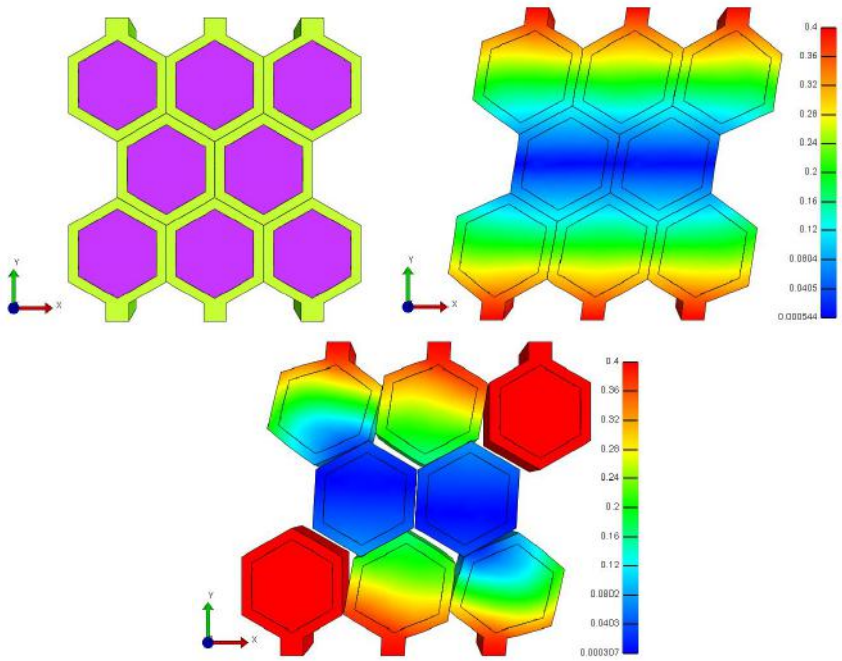

Figure 4.15: 3×3 cellular tissue with cellular inclusions under shear deformation. Elasticity of cellular inclusions are 10% softer than cell walls. The colour bar represents total displacement in the X direction.

The behaviour here is an interplay between volume restriction and inclusion elasticity. As the elasticity constants decrease away from that of the cell wall the behaviour will converge somewhere close to the 1000× case. Conversely, as the material properties increase towards that of the cell wall then the cells will become homogeneous granules. Thus empty cellular tissues and homogeneous granules provide an upper and lower bound for debonding behaviour.

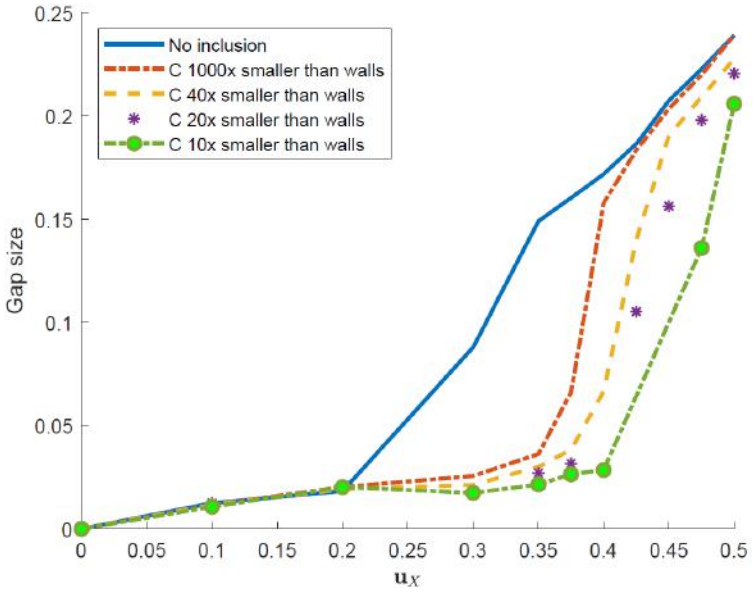

Figure 4.16: Comparison of gap sizes for varying core stiffness's in a 3×3 tissue.

4.5 Summary

Numerically, when finite element models of periodic structures with hexagonal cells are sheared, significant cell separation is captured diagonally across the structure. To obtain the numerical results, we employ a successive deformation decomposition technique, whereby: (i) first, a continuous deformation is assumed throughout the structure; (ii) then, for the predeformed structure the unilateral contact between cell walls are taken into account. The two-step procedure proves significantly faster and more accurate than a one-step approach where the external boundary conditions and contact constraints are imposed simultaneously.

Our analysis further indicates that, under large deformations, separation is less likely between cells with high internal cell pressure than between cells where the internal pressure is low. This is in agreement with the physical observations that plant tissue under high turgor pressure (*e.g.* in fresh and growing fruit and vegetables) failed by cell wall rupture, whereas tissue under low turgor (*e.g.* in cooked or ageing plants) failed by cell separation. The way cells separate or break and release their content is critical for horticultural qualities, such as fruit texture, which is of major interest to producers around the world. As markets impose increasingly stringent quality standards, there is a demand for development of models that predict changes in fruit texture so that these processes can be managed and controlled more effectively. Even though, in most cases, it is at a cellular level that the structural basis of texture is best addressed, due to the inherent complexity and diversity of cellular structures, the explicit representation of all individual cells and their contact constraints in a structure with a very large number of cells is not feasible computationally. Nonetheless, since local changes can generate changes in the overall structural properties, the micro-structural model with non-penetrative intercellular contact proposed here can be incorporated in a multiple scale approach suitable for use in large-scale finite element computations.

Our simulations of non-penetrative contact within cellular bodies with hyper-elastic cell walls, and the computational strategy which we employ is novel. This work has been the subject of many talks, most notably presented at the 25th Conference of the UK Association for Computational Mechanics, where the author received the Mike Crisfield Award, for best presenter of all PhD and post doctoral researchers. The author also won sizeable sponsorship to communicate these findings at an international conference on 'biological soft matter and agricultural food challenges' in Sao Paulo, Brazil - which also then lead to an invited talk in the Food Sciences group at the University of Nottingham, to discuss possible collaboration.

Chapter 5

Multiscale analysis of cellular structures

5.1 Introduction

Solid cellular structures are widespread in nature and in an ever increasing number of biomedical and engineering applications [22, 42, 55, 65, 66, 103, 114, 145, 161]. For example, engineered tissue scaffolds provide an environment for growth and regeneration of biological cells [20, 39, 43, 45, 47, 129, 143, 164, 166, 171], while natural materials generally incorporate several levels of structural hierarchy, which contribute to their macroscopic physical properties [51, 54, 134, 160, 173]. From the modelling point of view, a sub-level in the structural hierarchy can be treated either as a substructure with its own geometry, or as a continuum described by a suitable material model.

When studying cellular structures, the common assumption is that cell walls are linearly elastic with a geometrically non-linear behaviour. In this case, if the cell walls bend, then the elastic response can be determined from the linear-elastic deflection of a beam [65, 66]. However, in many cellular structures, when loaded, the cell walls stretch axially rather than bend. The dominant mechanical behaviour is determined by the architecture and depends on whether the cells are

open or closed [30,160]. Stretch-dominated cellular structures, such as octet-truss and body-centred cubic geometries, for example (see Figure 5.1), have a higher stiffness-to-weight ratio than bending-dominated ones [23, 30, 31, 44, 54, 66, 101, 159, 160]. In addition, biological and bio-inspired materials are often non-linearly elastic under large strains, and a finite elasticity approach is needed to understand them [67, 73, 127, 157].

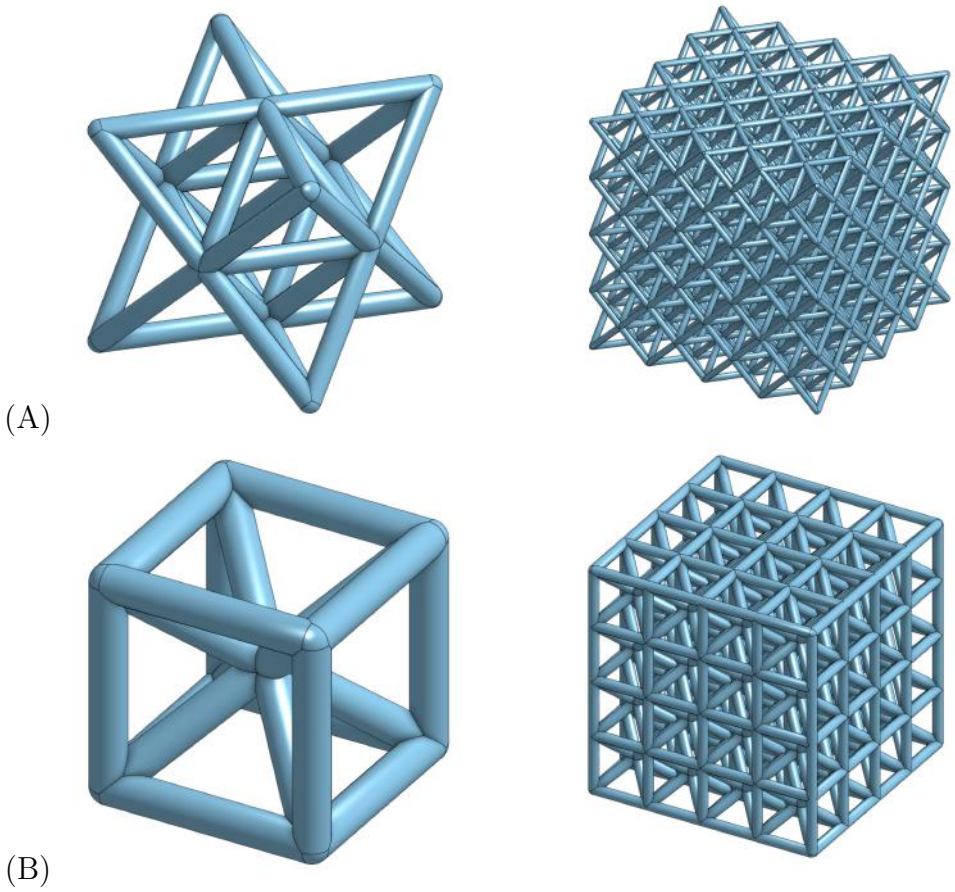

Figure 5.1: Examples of stretch-dominated architectures: (A) octet-truss and (B) body-centred cubic, at the cell level (left) and at the mesoscopic structural level (right), respectively.

Microstructure-based models for a cellular solid with open cells of isotropic linearly-elastic material were first proposed by Gent & Thomas (1959) [61], where infinitesimal stretches were assumed. In [62], these models were extended to structures with closed cells containing an ideal gas. For these models, effective Young's modulus and Poisson's ratio under infinitesimal deformations were derived explic-

itly from the constitutive equations [11,13]. For cellular structures of non-linearly elastic material under finite strain deformations, a phenomenological continuum model was proposed by Blatz & Ko (1962) [15]. This model reduces to the Gent-Thomas model in the small strain limit [10, 12]. Later, it was noted in [153] that Hill's energy functional of hyperelasticity [72] can be used to describe the simple special case of structures where the principal stresses are uncoupled, i.e. depend only on the stretch ratio in the corresponding principal direction. These approaches are based on Ogden-type strain-energy functions for compressible materials extending the incompressible strain-energy functions defined in [126].

For stretch-dominated structures with open or closed cells made from non-linear elastic materials, in [118,119], novel continuum isotropic hyperelastic models, at a mesoscopic level, where the number of cells was finite and the size of the structure was comparable to the size of the cells, were constructed analytically from the structural architecture and the material properties at the cell level. For these structures, the cell walls, which were equal in size and arbitrarily oriented, were under finite triaxial deformations, while the joints between adjacent walls were not elastically deformed. The elastic responses at different scales were related by the assumption that, when the structure is subject to a triaxial stretch, each cell wall deforms also by a triaxial stretch, without bending or buckling, and the stretches of the structure and of the cell walls were related by a rotation. Possible instability effects due to cell wall buckling, for example, which could also occur under large deformations, were discussed in [118].

In this chapter, we bring new insight into the constitutive behaviour of the stretch-dominated, open- and closed-cell models introduced in [118,119], by providing a systematic derivation of their non-linear elastic parameters in the theoretical framework of [113]. As the focus of this study is the formal derivation of non-linear elastic parameters, for which finite homogeneous deformations are required, possible damage or instability effects are not discussed here. We start

with a summary of the hyperelastic models and specialise these models to the case with neo-Hookean cell components (Section 5.2), which we then analyse explicitly as follows. For each model, first, the *non-linear shear modulus* is calculated under the multiaxial deformation consisting of simple shear superposed on finite uniaxial stretch (Section 5.3.1). Then, the *non-linear Poisson's ratio* is computed under uniaxial stretch, and the corresponding *non-linear stretch modulus* is obtained from a *universal relation* involving the shear modulus as well (Section 5.3.2). A universal relation is valid for a class of strain energy density functions, in this case, isotropic hyperelastic materials. The role of the non-linear shear and stretch moduli is to reflect stiffening or softening in a material under increasing loads. Volume changes are quantified by the *non-linear bulk modulus* under hydrostatic pressure (Section 5.3.3). To illustrate the theoretical results, we present and discuss the non-linear elastic parameters of open- or closed-cell models where the material and geometric parameters at the cell level are specified (Sections 5.3.4).

The strength of this model is highlighted is Section 5.4 by being applied 'backwards' to experimental data to predict cell wall behaviour, using an incompressible Fung type model to capture cell wall stiffening. Finally, in Section 5.5.1 the model based on neo-Hookean cell walls is implemented as a new material model in FEBio.

5.2 Hyperelastic models for stretch-dominated architectures

In this section, first we summarise the general formulation of the continuum hyperelastic models for stretch-dominated architectures with open or closed cells proposed in [118, 119]. We then specialise these models to the particular case of structures with neo-Hookean cell components, which we analyse in detail in the next sections.

5.2.1 Geometric assumptions

The geometric assumptions are as follows: all cell walls are equal, with undeformed thickness t and length L; the walls are thin, with the thickness-to-length ratio $0 < k = t/L < 1$; and cell walls meet at joints with thickness t.

The representative volume fraction, ρ_w, signifies the fraction of cell wall material in the structure, excluding the volume of the joint. This can be calculated explicitly if the geometry is known. Here, we make further assumptions which let us express a general ρ_w only as a function of k.

Open-cell structures. For the open-cell structure [118], we consider the case where all cell walls meet at spherical joints (Figure 5.2A). It is assumed that the entire surface of the joint is covered by cell walls (such that no red cell joint is visible in Figure 5.2), then the volume of cell walls surrounding a joint is a function of the joint's surface area $4\pi(t/2)^2 = 4\pi(kL/2)^2$. Half of each cell wall $L/2$ is assumed to belong to each joint, giving

$$V_{wall} = \frac{\pi k^2 L^3}{2} \tag{5.2.1}$$

Taking the unit volume as the volume of the sphere with radius $R = (L+t)/2 = L(1+k)/2$, which is centred at a joint and contains half of the length of each cell wall connected to that joint (see Figure 5.2B),

$$V_{unit} = \frac{\pi L^3 (1+k)^3}{6} \tag{5.2.2}$$

Thus, the representative volume fraction of solid material contained in the cell walls, included in this sphere, is

$$\rho_w^{(o)} = \frac{V_{wall}}{V_{unit}} = \frac{3k^2}{(1+k)^3}. \tag{5.2.3}$$

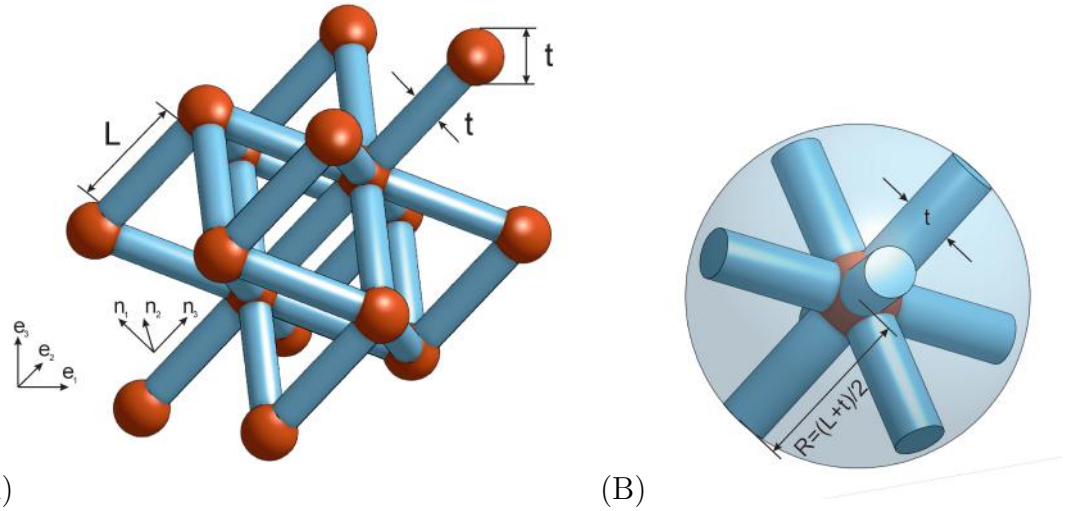

(A) (B)

Figure 5.2: Example stretch-dominated open-cell structure: (A) geometric assumptions and (B) unit sphere.

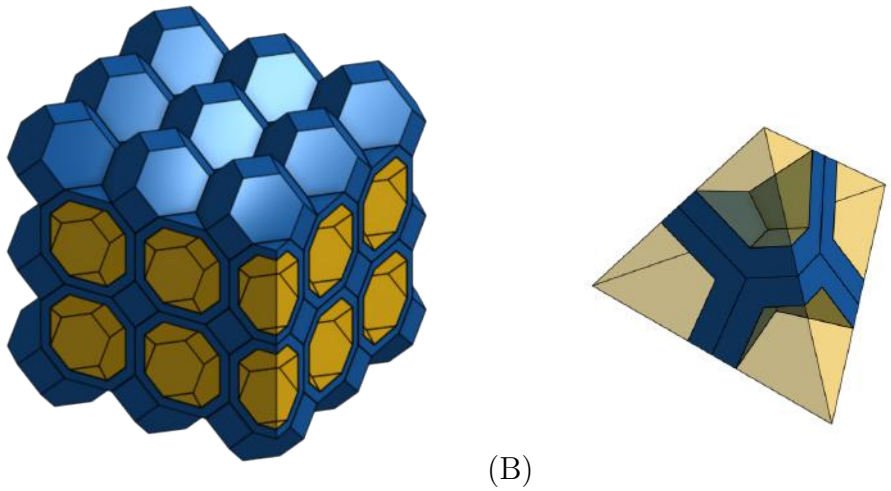

(A) (B)

Figure 5.3: Example stretch-dominated closed-cell structure: (A) tetrakaidecahedral packing and (B) representative volume based around a four cell junction.

Closed-cell structures. For the closed-cell structures [119], all cell walls have flat faces and adjacent cell walls meet along cell edges of length L, while adjacent cell edges meet at spherical joints. In this case, setting the unit volume as the volume of a sphere with radius $R = (L + t)/2 = L(1 + k)/2$, centred at a joint, the representative volume fraction of solid material contained the cell walls (faces and edges) included in this sphere, is equal to

$$\rho_w^{(c)} = \frac{3k}{(1+k)^2}, \tag{5.2.4}$$

while the remaining volume fraction, taken by the cell core, is

$$\rho_c^{(c)} = \frac{1}{(1+k)^3}. \tag{5.2.5}$$

See [119] for detailed derivation.

5.2.2 Kinematic assumptions

Stretch-dominated open-cell structures. When the structure is deformed homogeneously with the principal stretches $\{\alpha_i\}_{i=1,2,3}$, each cell wall deforms by a triaxial stretch with the principal stretches $\{\lambda_i\}_{i=1,2,3}$. Let $(\mathbf{e}_1, \mathbf{e}_2, \mathbf{e}_3)$ be the usual orthonormal vectors for the Cartesian coordinates in the principal directions in which the structure deforms, and $(\mathbf{n}_1, \mathbf{n}_2, \mathbf{n}_3)$ denote the orthonormal vectors in the principal direction of a deforming cell wall, satisfying:

$$\begin{aligned}
\mathbf{n}_1 =& -\mathbf{e}_1 \cos\theta\cos\phi - \mathbf{e}_2 \cos\theta \sin\phi + \mathbf{e}_3 \sin\theta, \\
\mathbf{n}_2 =& \mathbf{e}_1 \sin\phi - \mathbf{e}_2 \cos\phi, \\
\mathbf{n}_3 =& \mathbf{e}_1 \sin\theta\cos\phi + \mathbf{e}_2 \sin\theta \sin\phi + \mathbf{e}_3 \cos\theta.
\end{aligned} \tag{5.2.6}$$

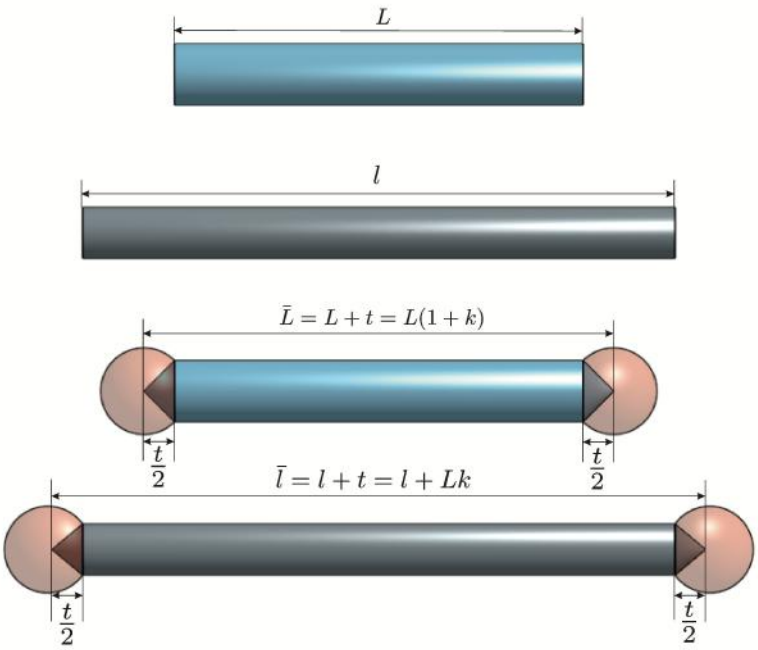

Figure 5.4: Cell wall and cell element before and after deformation in a stretch-dominated open-cell structure.

- For the cell wall, the deformation gradient is the stretch tensor $\mathbf{F} = \text{diag}(\lambda_1, \lambda_2, \lambda_3)$ and the Cauchy-Green tensor is equal to $\mathbf{C} = \text{diag}(\lambda_1^2, \lambda_2^2, \lambda_3^2)$. We denote the principal invariants of the stretch tensor, $\mathbf{F}$, by

$$\begin{aligned} \iota_1 &= \lambda_1 + \lambda_2 + \lambda_3, \\ \iota_2 &= \lambda_1\lambda_2 + \lambda_2\lambda_3 + \lambda_3\lambda_1, \\ \iota_3 &= \lambda_1\lambda_2\lambda_3, \end{aligned} \tag{5.2.7}$$

and the principal invariants of the Cauchy-Green tensor, $\mathbf{C}$, by

$$\begin{aligned} I_1 &= \lambda_1^2 + \lambda_2^2 + \lambda_3^2, \\ I_2 &= \lambda_1^2\lambda_2^2 + \lambda_2^2\lambda_3^2 + \lambda_3^2\lambda_1^2, \\ I_3 &= \lambda_1^2\lambda_2^2\lambda_3^2. \end{aligned} \tag{5.2.8}$$

From (5.2.7) and (5.2.8), we obtain

$$\begin{aligned} I_1 &= \iota_1^2 - 2\iota_2, \\ I_2 &= \iota_2^2 - 2\iota_1\iota_3, \\ I_3 &= \iota_3^2. \end{aligned} \tag{5.2.9}$$

- Assuming that the cell joints do not deform, if L and l are the lengths of a cell wall before and after the deformation, respectively, and t is the width of a joint between adjacent walls, we denote by $\overline{L} = L + t = (1+k)L$ and $\bar{l} = l + t = l + kL$ the corresponding lengths of a cell element comprising a cell wall and a joint (or a cell wall and half of each joint situated at the ends of the wall) before and after the deformation (Figure 5.4). Then the principal stretches for a cell element are

$$\overline{\lambda}_i = \frac{\lambda_i + k}{1+k}, \qquad i = 1, 2, 3. \tag{5.2.10}$$

Due to the structure undergoing homogeneous deformation, the cell element is assumed to deform in the same manner as the structure, relating the principal stretches of the cell element $\{\overline{\lambda}_i\}_{i=1,2,3}$ to the principal stretches of the structure $\{\alpha_i\}_{i=1,2,3}$ by

$$\begin{aligned} \overline{\lambda}_1^2 =& \alpha_1^2 \cos^2\theta \cos^2\phi + \alpha_2^2 \cos^2\theta \sin^2\phi + \alpha_3^2 \sin^2\theta, \\ \overline{\lambda}_2^2 =& \alpha_1^2 \sin^2\phi + \alpha_2^2 \cos^2\phi, \\ \overline{\lambda}_3^2 =& \alpha_1^2 \sin^2\theta \cos^2\phi + \alpha_2^2 \sin^2\theta \sin^2\phi + \alpha_3^2 \cos^2\theta. \end{aligned} \tag{5.2.11}$$

Denoting the principal invariants of the stretch tensor $\overline{\mathbf{F}} = \mathrm{diag}(\overline{\lambda}_1, \overline{\lambda}_2, \overline{\lambda}_3)$ by

$$\begin{aligned} \bar{\imath}_1 &= \overline{\lambda}_1 + \overline{\lambda}_2 + \overline{\lambda}_3, \\ \bar{\imath}_2 &= \overline{\lambda}_1\overline{\lambda}_2 + \overline{\lambda}_2\overline{\lambda}_3 + \overline{\lambda}_3\overline{\lambda}_1, \\ \bar{\imath}_3 &= \overline{\lambda}_1\overline{\lambda}_2\overline{\lambda}_3, \end{aligned} \tag{5.2.12}$$

the following relations hold between the stretch invariants (5.2.7) and (5.2.12), of the cell wall and of the cell element, respectively,

$$\begin{aligned}
\iota_1 &= (1+k)\bar{i}_1 - 3k, \\
\iota_2 &= (1+k)^2\bar{i}_2 - 2k(1+k)\bar{i}_1 + 3k^2, \\
\iota_3 &= (1+k)^3\bar{i}_3 - k(1+k)^2\bar{i}_2 + k^2(1+k)\bar{i}_1 - k^3.
\end{aligned} \tag{5.2.13}$$

Then, by (5.2.9) and (5.2.13),

$$\begin{aligned}
I_1 &= \left[(1+k)\bar{i}_1 - 3k\right]^2 - 2\left[(1+k)^2\bar{i}_2 - 2k(1+k)\bar{i}_1 + 3k^2\right], \\
I_2 &= \left[(1+k)^2\bar{i}_2 - 2k(1+k)\bar{i}_1 + 3k^2\right]^2 \\
&\quad - 2\left[(1+k)\bar{i}_1 - 3k\right]\left[(1+k)^3\bar{i}_3 - k(1+k)^2\bar{i}_2 + k^2(1+k)\bar{i}_1 - k^3\right], \\
I_3 &= \left[(1+k)^3\bar{i}_3 - k(1+k)^2\bar{i}_2 + k^2(1+k)\bar{i}_1 - k^3\right]^2.
\end{aligned} \tag{5.2.14}$$

- For the structure, the principal invariants of the stretch tensor are

$$\begin{aligned}
i_1 &= \alpha_1 + \alpha_2 + \alpha_3, \\
i_2 &= \alpha_1\alpha_2 + \alpha_2\alpha_3 + \alpha_3\alpha_1, \\
i_3 &= \alpha_1\alpha_2\alpha_3.
\end{aligned} \tag{5.2.15}$$

Stretch-dominated closed-cell structures. For the closed-cell structures, the kinematic assumptions on the cell walls and the cell joints are the same as for the open-cell case. In addition, when the cells are filled with an isotropic hyperelastic core, it is assumed that the cell core deforms homogeneously with the cell walls and remains in full active contact with the adjacent cell walls throughout the deformation, i.e., no internal gaps occur.

Remark 5.2.1 *We note that, in order for the kinematic assumptions to be satisfied, and in particular, that the deformation of the cell walls can be approximated by a triaxial stretch, while the elastic deformation of the joints may be neglected, it is reasonable to assume that the thickness of the walls, t, is much smaller than the*

length of the walls, L, and hence $k = t/L$ is sufficiently small, i.e. $0 < k \ll 1$. In practice, the upper limit for k, such that the kinematic assumptions are reasonably satisfied, will depend on both the cell wall material and cell geometry. In particular, under the geometric and kinematic assumptions described above, in [118], numerical examples show that the mesoscopic models capture the behaviour of cellular structures with a fixed number of cells and increasing wall thickness more accurately for the structures with thinner walls, where the deformation of the walls is closer to the triaxial stretch and the joints deform less significantly, as assumed theoretically, than for those with thicker walls, where the theoretical assumptions fail to be satisfied. In the numerical examples presented in Section 5.3.4, we compare numerically the non-linear material properties of the mesoscopic models, by taking $k \in \{0.1, 0.2, 0.3\}$ and the cell wall material parameters fixed, or varying the cell core material parameters while the cell wall material is fixed, with $k = 0.1$.

5.2.3 Constitutive models

First, we recall that, for a homogeneous isotropic hyperelastic material, the following principles hold:

- Material objectivity (frame indifference), which states that the constitutive equation must be invariant under changes of frame of reference, i.e. the scalar strain-energy function, $\mathcal{W} = \mathcal{W}(\mathbf{F})$, depending only on the deformation gradient $\mathbf{F}$, with respect to the reference configuration, is unaffected by a superimposed rigid-body transformation (which involves a change of position) after deformation, i.e. $\mathcal{W}(\mathbf{R}^T\mathbf{F}) = \mathcal{W}(\mathbf{F})$, where $\mathbf{R} \in SO(3)$ is a proper orthogonal tensor (rotation).

- Material isotropy, which requires that the strain-energy function is unaffected by a superimposed rigid-body transformation prior to deformation, i.e. $\mathcal{W}(\mathbf{FQ}) = \mathcal{W}(\mathbf{F})$, where $\mathbf{Q} \in SO(3)$.

Assuming that the cell walls are made from a homogeneous isotropic hyperelastic material, it follows from the kinematic assumptions in Section 5.2.2 that the following strain-energy functions can be equivalently expressed:

- By (5.2.9) the strain-energy of the wall $\mathcal{W}_w$ can be expressed in terms of the principal invariants of $\mathbf{C}$ or $\mathbf{F}$ of the cell wall deformation

$$\mathcal{W}_w(I_1, I_2, I_3) = \mathcal{W}_w(\iota_1, \iota_2, \iota_3). \tag{5.2.16}$$

- By (5.2.13), the strain-energy of the wall can be related to the strain-energy of the cell element $\overline{\mathcal{W}}_w$

$$\mathcal{W}_w(\iota_1, \iota_2, \iota_3) = \overline{\mathcal{W}}_w(\bar{i}_1, \bar{i}_2, \bar{i}_3) \tag{5.2.17}$$

- By (5.2.11), (5.2.12),(5.2.15) and the principals of material objectivity and isotropy, the strain-energy of the element can be equivalently written in terms of the the structure's principal invariants

$$\overline{\mathcal{W}}_w(\bar{i}_1, \bar{i}_2, \bar{i}_3) = \overline{\mathcal{W}}_w(i_1, i_2, i_3). \tag{5.2.18}$$

Open-cell model. For the open-cell model, the strain-energy function per unit volume is defined by taking the mean value of the cell wall energy over the unit sphere [118],

$$\begin{aligned} \mathcal{W}^{(o)}(i_1, i_2, i_3) &= \rho_w^{(o)} \frac{2}{\pi} \int_0^{\pi/2} \int_0^{\pi/2} \overline{\mathcal{W}}_w(i_1, i_2, i_3) \sin\theta \mathrm{d}\theta \mathrm{d}\phi \\ &= \rho_w^{(o)} \overline{\mathcal{W}}_w(i_1, i_2, i_3). \end{aligned} \tag{5.2.19}$$

Then, the principal components of the corresponding Cauchy stress tensor are

$$\begin{aligned}\sigma_i^{(o)} &= J_o^{-1}\alpha_i\frac{\partial \mathcal{W}^{(o)}}{\partial \alpha_i} \\ &= J_o^{-1}\frac{\partial \mathcal{W}^{(o)}}{\partial\left(\ln \alpha_i\right)}, \qquad i=1,2,3,\end{aligned} \tag{5.2.20}$$

where $\{\alpha_i\}_{i=1,2,3}$ the principal stretches of the structure and $J_o = i_3 = \alpha_1\alpha_2\alpha_3$.

A consequence of this formulation is that if a cell wall is incompressible, so will the structure. This relationship would not be true in a bending-dominated structure, where the cell wall bending allows for a high level of compressibility. However this assumption fits for stretch-dominated structures, especially in tension where relatively little buckling should occur, as discussed in [118].

Closed-cell model. For the closed-cell model, the strain-energy function is equal to [119]

$$\mathcal{W}^{(c)}(i_1,i_2,i_3) = \rho_w^{(c)}\overline{\mathcal{W}}_w(i_1,i_2,i_3) + \rho_c^{(c)}\mathcal{W}_c(i_1,i_2,i_3), \tag{5.2.21}$$

where $\overline{\mathcal{W}}_w(i_1,i_2,i_3)$ and $\mathcal{W}_c(i_1,i_2,i_3)$ are the strain-energy functions for the cell walls and the cell core, respectively. When the cells are empty, the hyperelastic model defined by (5.2.21) simplifies to

$$\mathcal{W}^{(e)}(i_1,i_2,i_3) = \rho_w^{(c)}\overline{\mathcal{W}}_w(i_1,i_2,i_3). \tag{5.2.22}$$

For the general closed-cell model given by (5.2.21), the principal components of the associated Cauchy stress tensor are

$$\begin{aligned}\sigma_i^{(c)} &= J_c^{-1}\alpha_i\frac{\partial \mathcal{W}^{(c)}}{\partial \alpha_i} \\ &= J_c^{-1}\frac{\partial \mathcal{W}^{(c)}}{\partial\left(\ln \alpha_i\right)}, \qquad i=1,2,3,\end{aligned} \tag{5.2.23}$$

where $J_c = i_3 = \alpha_1\alpha_2\alpha_3$.

5.2.4 The particular case with neo-Hookean cell components

To investigate formally the non-linear elastic behaviour of the constitutive models (5.2.19) and (5.2.21), we specialise to the case where the cell wall material is described by the compressible neo-Hookean model

$$\mathcal{W}_w(I_1, I_2, I_3) = \frac{\mu_w}{2}\left(I_1 - 3 - \ln I_3\right) + \frac{\lambda_w}{2}\left(\ln I_3^{1/2}\right)^2, \tag{5.2.24}$$

with $\mu_w > 0$ and $\lambda_w > 0$ constants.

Open cells with neo-Hookean cell walls. The strain-energy function for the open-cell model (5.2.19) with the cell wall material described by (5.2.24) is equal to [118]

$$\begin{aligned}\mathcal{W}^{(o)}(i_1, i_2, i_3) = {} & \frac{\mu_w \rho_w^{(o)}}{2}\left[(1+k)^2\left(i_1^2 - 2i_2\right) - 2k(1+k)i_1 - 3\left(1-k^2\right)\right] \\ & - \mu_w \rho_w^{(o)} \ln\left[(1+k)^3 i_3 - k(1+k)^2 i_2 + k^2(1+k)i_1 - k^3\right] \\ & + \frac{\lambda_w \rho_w^{(o)}}{2}\left\{\ln\left[(1+k)^3 i_3 - k(1+k)^2 i_2 + k^2(1+k)i_1 - k^3\right]\right\}^2.\end{aligned} \tag{5.2.25}$$

The associated principal Cauchy stress components, given by (5.2.20), are

$$\begin{aligned}\sigma_i^{(o)} = {} & \mu_w \rho_w^{(o)}(1+k)\frac{\alpha_i}{\alpha_1\alpha_2\alpha_3}\left[\alpha_i(1+k) - k - \frac{1}{\alpha_i(1+k) - k}\right] \\ & + \lambda_w \rho_w^{(o)}(1+k)\frac{\alpha_i}{\alpha_1\alpha_2\alpha_3}\frac{\ln\left[(1+k)^3 i_3 - k(1+k)^2 i_2 + k^2(1+k)i_1 - k^3\right]}{\alpha_i(1+k) - k}, \qquad i = 1, 2, 3.\end{aligned} \tag{5.2.26}$$

Closed cells with neo-Hookean components. For the closed-cell structures, if the cells are filled, we further assume that the cell core is characterised by the

neo-Hookean model

$$\mathcal{W}_c(I_1, I_2, I_3) = \frac{\mu_c}{2}\left(I_1 - 3 - \ln I_3\right) + \frac{\lambda_c}{2}\left(\ln I_3^{1/2}\right)^2, \tag{5.2.27}$$

with $\mu_c > 0$, $\lambda_c > 0$ constants. Then, the strain-energy function for the closed-cell model (5.2.21) takes on the form [119]

$$\begin{aligned}\mathcal{W}^{(c)}(i_1, i_2, i_3) = {} & \frac{\mu_w \rho_w^{(c)}}{2}\left[(1+k)^2\left(i_1^2 - 2i_2\right) - 2k(1+k)i_1 - 3\left(1-k^2\right)\right] \\ & - \mu_w \rho_w^{(c)} \ln\left[(1+k)^3 i_3 - k(1+k)^2 i_2 + k^2(1+k)i_1 - k^3\right] \\ & + \frac{\lambda_w \rho_w^{(c)}}{2}\left\{\ln\left[(1+k)^3 i_3 - k(1+k)^2 i_2 + k^2(1+k)i_1 - k^3\right]\right\}^2 \\ & + \rho_c^{(c)}\left[\frac{\mu_c}{2}\left(i_1^2 - 2i_2 - 3 - 2\ln i_3\right) + \frac{\lambda_c}{2}\left(\ln i_3\right)^2\right].\end{aligned} \tag{5.2.28}$$

The associated principal Cauchy stresses, given by (5.2.23), are

$$\begin{aligned}\sigma_i^{(c)} = {} & \mu_w \rho_w^{(c)}(1+k)\frac{\alpha_i}{\alpha_1\alpha_2\alpha_3}\left[\alpha_i(1+k) - k - \frac{1}{\alpha_i(1+k) - k}\right] \\ & + \lambda_w \rho_w^{(c)}(1+k)\frac{\alpha_i}{\alpha_1\alpha_2\alpha_3}\frac{\ln\left[(1+k)^3 i_3 - k(1+k)^2 i_2 + k^2(1+k)i_1 - k^3\right]}{\alpha_i(1+k) - k} \\ & + \frac{\rho_c^{(c)}}{\alpha_1\alpha_2\alpha_3}\left[\mu_c\left(\alpha_i^2 - 1\right) + \lambda_c \ln i_3\right], \qquad i = 1, 2, 3.\end{aligned} \tag{5.2.29}$$

5.3 Non-linear elastic moduli

5.3.1 Shear modulus

In this section, for the hyperelastic models (5.2.25) and (5.2.28), we determine explicit *non-linear shear moduli*, as discussed in [113]. Consider the following multiaxial homogeneous deformation [49, 147], consisting of simple shear super-

posed on finite uniaxial stretch (Figure 5.5) [35, 113, 132],

$$\begin{aligned} x_1 &= \alpha(a)X_1 + \gamma a X_3, \\ x_2 &= \alpha(a)X_2, \\ x_3 &= aX_3, \end{aligned} \tag{5.3.1}$$

where (X_1, X_2, X_3) and (x_1, x_2, x_3) are the Cartesian coordinates for the Lagrangian (reference) and the Eulerian (current) configuration, respectively, and a and γ are positive constants.

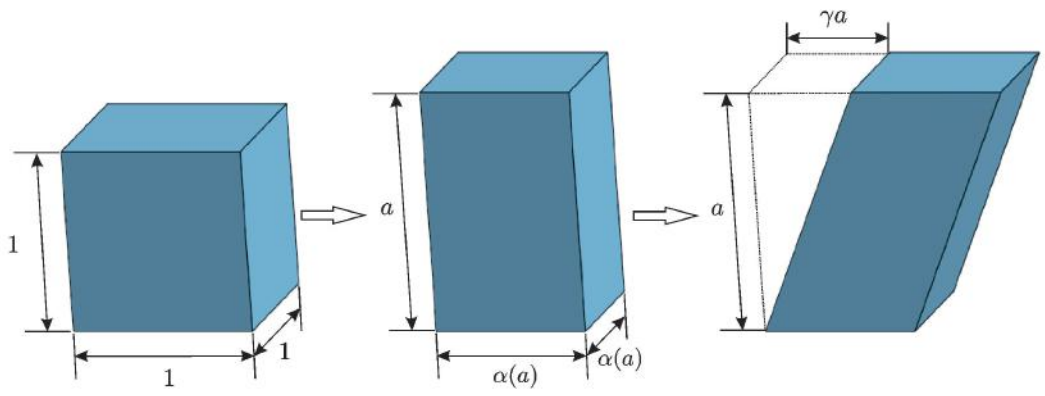

Figure 5.5: Cube (left) deformed by uniaxial stretch (middle) followed by simple shear (right).

For this deformation, the principal stretches $\{\alpha_i\}_{i=1,2,3}$ satisfy

$$\begin{aligned} \alpha_1^2 &= \frac{\alpha(a)^2 + a^2\left(1+\gamma^2\right) + \sqrt{\left[\alpha(a)^2 + a^2\left(1+\gamma^2\right)\right]^2 - 4a^2\alpha(a)^2}}{2}, \\ \alpha_2^2 &= \frac{\alpha(a)^2 + a^2\left(1+\gamma^2\right) - \sqrt{\left[\alpha(a)^2 + a^2\left(1+\gamma^2\right)\right]^2 - 4a^2\alpha(a)^2}}{2}, \\ \alpha_3^2 &= \alpha(a)^2. \end{aligned} \tag{5.3.2}$$

Then, $J = \alpha_1\alpha_2\alpha_3 = a\alpha(a)^2$.

The *non-linear shear modulus* is defined as [113],

$$\mu(a,\gamma) = \frac{\sigma_1 - \sigma_2}{\alpha_1^2 - \alpha_2^2}, \tag{5.3.3}$$

where $\{\sigma_i\}_{i=1,2,3}$ are the principal components of the Cauchy stress tensor associated with the deformation (5.3.1).

Remark 5.3.1 *Note that the non-linear shear modulus* (5.3.3) *is positive if the Baker-Ericksen (BE) inequalities hold. These inequalities state that the greater principal stress occurs in the direction of the greater principal stretch and take on the form*

$$(\sigma_i - \sigma_j)(\alpha_i - \alpha_j) > 0 \quad \textit{if} \quad \alpha_i \neq \alpha_j, \quad i, j = 1, 2, 3, \tag{5.3.4}$$

with "$\geq$" replacing the strict inequality "$>$" if any two principal stretches are equal [8, 93].

For the neo-Hookean models (5.2.24) and (5.2.27), the non-linear shear modulus (5.3.3) is constant and equal to μ_w and μ_c, respectively.

When $a \to 1$, i.e., for simple shear superposed on infinitesimal axial stretch, the non-linear shear modulus given by (5.3.3) converges to the non-linear shear modulus for simple shear,

$$\widehat{\mu}(\gamma) = \lim_{a \to 1} \mu(a, \gamma), \tag{5.3.5}$$

and the principal stretches satisfy

$$\begin{aligned}
\widehat{\alpha}_1^2 &= 1 + \frac{\gamma^2 + \gamma\sqrt{\gamma^2 + 4}}{2} = \alpha^2, \\
\widehat{\alpha}_2^2 &= 1 + \frac{\gamma^2 - \gamma\sqrt{\gamma^2 + 4}}{2} = \alpha^{-2}, \\
\widehat{\alpha}_3^2 &= 1.
\end{aligned}$$

Similarly, when $\gamma \to 0$, i.e., for infinitesimal shear superposed on finite axial stretch, the non-linear shear modulus, given by (5.3.3), converges to

$$\widetilde{\mu}(a) = \lim_{\gamma \to 0} \mu(a, \gamma). \tag{5.3.6}$$

If $a \to 1$ and $\gamma \to 0$, then these shear moduli converge to the linear shear

modulus of the infinitesimal theory, i.e.,

$$\begin{aligned}\overline{\mu} &= \lim_{a\to 1}\lim_{\gamma\to 0}\mu(a,\gamma)\\ &= \lim_{\gamma\to 0}\widehat{\mu}(\gamma)\\ &= \lim_{a\to 1}\widetilde{\mu}(a).\end{aligned} \tag{5.3.7}$$

Open-cell model. For the open-cell model (5.2.25), the non-linear shear modulus (5.3.3) is

$$\begin{aligned}\mu^{(o)}(a,\gamma) = \frac{\mu_w\rho_w^{(o)}(1+k)}{\alpha_1\alpha_2\alpha_3\,(\alpha_1+\alpha_2)}\left[(\alpha_1+\alpha_2)\,(1+k)-k+\frac{k}{[\alpha_1(1+k)-k]\,[\alpha_2(1+k)-k]}\right]\\ -\frac{\lambda_w\rho_w^{(o)}k(1+k)}{\alpha_1\alpha_2\alpha_3\,(\alpha_1+\alpha_2)}\frac{\ln[\alpha_1(1+k)-k]+\ln[\alpha_2(1+k)-k]+\ln[\alpha_3(1+k)-k]}{[\alpha_1(1+k)-k]\,[\alpha_2(1+k)-k]}.\end{aligned} \tag{5.3.8}$$

When $a\to 1$, the non-linear shear modulus given by (5.3.5) is equal to

$$\widehat{\mu}^{(o)}(\gamma) = \lim_{a\to 1}\mu^{(o)}(a,\gamma), \tag{5.3.9}$$

and if $\gamma\to 0$, then the non-linear shear modulus defined by (5.3.6) is

$$\widetilde{\mu}^{(o)}(a) = \lim_{\gamma\to 0}\mu^{(o)}(a,\gamma). \tag{5.3.10}$$

In the linear elastic limit [118], $a\to 1$ and $\gamma\to 0$, by (5.2.3), these shear moduli converge to

$$\begin{aligned}\overline{\mu}^{(o)} &= \lim_{a\to 1}\lim_{\gamma\to 0}\mu^{(o)}(a,\gamma)\\ &= \mu_w\rho_w^{(o)}(1+k)^2\\ &= \mu_w\frac{3k^2}{1+k}.\end{aligned} \tag{5.3.11}$$

Closed-cell model. Similarly, for the closed-cell model (5.2.28), the non-linear shear modulus (5.3.3) is equal to

$$\begin{aligned}\mu^{(c)}(a,\gamma) = {} & \frac{\mu_w \rho_w^{(c)}(1+k)}{\alpha_1\alpha_2\alpha_3\,(\alpha_1+\alpha_2)}\left[(\alpha_1+\alpha_2)\,(1+k) - k + \frac{k}{[\alpha_1(1+k)-k]\,[\alpha_2(1+k)-k]}\right] \\ & - \frac{\lambda_w \rho_w^{(c)} k(1+k)}{\alpha_1\alpha_2\alpha_3\,(\alpha_1+\alpha_2)}\,\frac{\ln[\alpha_1(1+k)-k] + \ln[\alpha_2(1+k)-k] + \ln[\alpha_3(1+k)-k]}{[\alpha_1(1+k)-k]\,[\alpha_2(1+k)-k]} \\ & + \frac{\mu_c \rho_c^{(c)}}{\alpha_1\alpha_2\alpha_3}.\end{aligned} \tag{5.3.12}$$

When $a \to 1$, the non-linear shear modulus (5.3.5) is

$$\widehat{\mu}^{(c)}(\gamma) = \lim_{a\to 1} \mu^{(c)}(a,\gamma), \tag{5.3.13}$$

and if $\gamma \to 0$, then the non-linear shear modulus (5.3.6) is

$$\widetilde{\mu}^{(c)}(a) = \lim_{\gamma\to 0} \mu^{(c)}(a,\gamma). \tag{5.3.14}$$

In the linear elastic limit [119], $a \to 1$ and $\gamma \to 0$, by (5.2.4) and (5.2.5), these moduli converge to

$$\begin{aligned}\overline{\mu}^{(c)} &= \lim_{a\to 1}\lim_{\gamma\to 0} \mu^{(c)}(a,\gamma) \\ &= \mu_w \rho_w^{(c)}(1+k)^2 + \mu_c \rho_c^{(c)} \\ &= 3k\mu_w + \mu_c \frac{1}{(1+k)^3}.\end{aligned} \tag{5.3.15}$$

When the closed cells are empty, we obtain the corresponding non-linear shear moduli, $\mu^{(e)}$, $\widehat{\mu}^{(e)}$, $\widetilde{\mu}^{(e)}$, and their linear elastic limit, $\overline{\mu}^{(e)}$, by setting $\rho_c^{(c)} = 0$ in (5.3.12), (5.3.13), (5.3.14), and (5.3.15), respectively.

5.3.2 Stretch modulus and Poisson function

Next, we focus on the simple extension (or contraction) $\mathrm{diag}(\alpha_1, \alpha_2, \alpha_3)$, with $\alpha_3 = a > 1$ ($a < 1$ for contraction) and $\alpha_1 = \alpha_2 = \alpha(a)$ (as in Figure 5.5 middle), for which the associated Cauchy stress tensor is equal to $\boldsymbol{\sigma} = \mathrm{diag}\,(0, 0, N)$, with $N > 0$ for uniaxial tension ($N < 0$ for uniaxial compression).

Remark 5.3.2 *We recall that, for a hyperelastic body subject to uniaxial tension (or compression), the deformation is a simple extension (contraction) in the direction of the tensile (compressive) force if and only if the BE inequalities* (5.3.4) *hold [8, 93]. If the BE inequalities are valid for the cell wall material, then these inequalities are valid also for the open- and closed-cell models (see details in [119]).*

The *non-linear Poisson's ratio*, defined in terms of the logarithmic (or Hencky, or true) strain, is equal to the following Poisson function [10, 113]

$$\nu(a) = -\frac{\ln \alpha(a)}{\ln a}. \tag{5.3.16}$$

Then, the *non-linear stretch modulus* satisfies the following *universal relation* (valid for all isotropic hyperelastic materials) [113],

$$E(a) = \widetilde{\mu}(a)\frac{a^2 - a^{-2\nu(a)}}{(1+\nu(a))\ln a}\left(1 + \nu(a) + a\nu'(a)\ln a\right), \tag{5.3.17}$$

where $\widetilde{\mu}(a)$ and $\nu(a)$ are given by (5.3.6) and (5.3.16), respectively, and $\nu'(a) = d\nu(a)/da$ is the derivative of $\nu(a)$ with respect to a.

We note that, for the neo-Hookean models (5.2.24) and (5.2.27), the non-linear Poisson's ratio given by (5.3.16) is not constant (see Section 5.3.2 for a proof). We denote by $\nu_w(a)$ and $E_w(a)$ the non-linear Poisson function and stretch modulus for the cell wall, respectively, and similarly, by $\nu_c(a)$ and $E_c(a)$ the non-linear Poisson function and stretch modulus for the cell core, respectively. Then, the

respective linear elastic limits are as follows:

$$\begin{aligned} \overline{\nu}_w &= \lim_{a\to 1} \nu_w(a) \\ &= \frac{\lambda_w}{2\,(\mu_w + \lambda_w)}, \\ \overline{E}_w &= \lim_{a\to 1} E_w(a) \\ &= 2\mu_w(1+\overline{\nu}_w), \end{aligned} \tag{5.3.18}$$

and

$$\begin{aligned} \overline{\nu}_c &= \lim_{a\to 1} \nu_c(a) \\ &= \frac{\lambda_c}{2\,(\mu_c + \lambda_c)}, \\ \overline{E}_c &= \lim_{a\to 1} E_c(a) \\ &= 2\mu_c(1+\overline{\nu}_c). \end{aligned} \tag{5.3.19}$$

Open-cell model. For the open-cell model (5.2.25) under the deformation $\mathrm{diag}(\alpha_1, \alpha_2, \alpha_3)$, such that $\alpha_3 = a$ and $\alpha_1 = \alpha_2 = \alpha(a)$ in the Cartesian directions $(\mathbf{e}_1, \mathbf{e}_2, \mathbf{e}_3)$, we assume that some of the cell walls are aligned with these Cartesian directions. Then, their deformation is $\mathrm{diag}(\lambda_1, \lambda_2, \lambda_3)$, where $\lambda_3 = a(1+k) - k$, $\lambda_1 = \lambda_2 = \lambda(a) = \lambda_3^{-\nu_w(\lambda_3)} = [a(1+k)-k]^{-\nu_w(a(1+k)-k)}$, and $\alpha(a) = (\lambda(a)+k)/(1+k)$. In this case, the non-linear Poisson's ratio, defined by (5.3.16), is equal to

$$\nu^{(o)}(a) = -\frac{\ln\left\{[a(1+k)-k]^{-\nu_w(a(1+k)-k)} + k\right\} - \ln(1+k)}{\ln a}. \tag{5.3.20}$$

In the linear elastic limit [118], the Poisson function given by (5.3.20) converges to

$$\begin{aligned} \overline{\nu}^{(o)} &= \lim_{a\to 1} \nu^{(o)}(a) \\ &= \overline{\nu}_w. \end{aligned} \tag{5.3.21}$$

The corresponding non-linear stretch modulus satisfies the following relation similar to (5.3.17),

$$E^{(o)}(a) = \widetilde{\mu}^{(o)}(a)\frac{a^2 - a^{-2\nu^{(o)}(a)}}{(1+\nu^{(o)}(a))\ln a}\left(1 + \nu^{(o)}(a) + a(\nu^{(o)})'(a)\ln a\right), \tag{5.3.22}$$

with $\widetilde{\mu}^{(o)}(a)$ given by (5.3.10). In the linear elastic limit [118], the non-linear stretch modulus defined by (5.3.22) converges to

$$\begin{aligned}\overline{E}^{(o)} &= \lim_{a\to 1} E^{(o)}(a)\\ &= \overline{E}_w \rho_w^{(o)}(1+k)^2\\ &= \overline{E}_w \frac{3k^2}{1+k}.\end{aligned} \tag{5.3.23}$$

Closed-cell model. Similarly, for the closed-cell model (5.2.28), if the cells are empty or the Poisson's ratios for the cell walls and the cell core are equal, i.e., $\nu_w = \nu_c$, then the Poisson function and stretch modulus are, respectively,

$$\nu^{(c)}(a) = -\frac{\ln\left\{[a(1+k)-k]^{-\nu_w(a(1+k)-k)} + k\right\} - \ln(1+k)}{\ln a} \tag{5.3.24}$$

and

$$E^{(c)}(a) = \widetilde{\mu}^{(c)}(a)\frac{a^2 - a^{-2\nu^{(c)}(a)}}{(1+\nu^{(c)}(a))\ln a}\left(1 + \nu^{(c)}(a) + a(\nu^{(c)})'(a)\ln a\right), \tag{5.3.25}$$

with $\widetilde{\mu}^{(c)}(a)$ given by (5.3.14). In the linear elastic limit [119],

$$\begin{aligned}\overline{\nu}^{(c)} &= \lim_{a\to 1} \nu^{(c)}(a)\\ &= \overline{\nu}_w\end{aligned} \tag{5.3.26}$$

and

$$\begin{aligned}\overline{E}^{(c)} &= \lim_{a\to 1} E^{(c)}(a) \\ &= \overline{E}_w \rho_w^{(c)}(1+k)^2 + \overline{E}_c \rho_c^{(c)} \\ &= 3k\overline{E}_w + \overline{E}_c \frac{1}{(1+k)^3}.\end{aligned} \tag{5.3.27}$$

Non-linear Poisson function for neo-Hookean material

Here we prove that the non-linear Poisson's ratio defined by (5.3.16) is not constant for an elastic body characterised by the generalised neo-Hookean model

$$\mathcal{W}(\alpha_1,\alpha_2,\alpha_3) = \frac{\mu}{2}\left[\alpha_1^2+\alpha_2^2+\alpha_3^2-3-\ln(\alpha_1^2\alpha_2^2\alpha_3^2)\right] + \frac{\lambda}{2}\left[\ln(\alpha_1\alpha_2\alpha_3)\right]^2, \tag{5.3.28}$$

where $\mu > 0$ and $\lambda > 0$ are constants.

Proof: Under simple tension or compression, $\mathrm{diag}(\alpha_1,\alpha_2,\alpha_3)$, with $\alpha_3 = a > 0$ and $\alpha_1 = \alpha_2 = \alpha(a)$, the associated Cauchy stress tensor is equal to $\boldsymbol{\sigma} = \mathrm{diag}\,(0,0,N)$, where $N \neq 0$ and the diagonal components satisfy

$$\sigma_i = J^{-1}\alpha_i \frac{\partial \mathcal{W}}{\partial \alpha_i}, \qquad i = 1,2,3, \tag{5.3.29}$$

with $J = \alpha_1\alpha_2\alpha_3$. For the constitutive model (5.3.28), under the given deformation, (5.3.29) reduces to

$$\begin{aligned}\frac{1}{\alpha_1^2\alpha_3}\left[\mu(\alpha_1^2-1)+\lambda\ln\left(\alpha_1^2\alpha_3\right)\right] &= 0, \\ \frac{1}{\alpha_1^2\alpha_3}\left[\mu(\alpha_3^2-1)+\lambda\ln\left(\alpha_1^2\alpha_3\right)\right] &= N.\end{aligned} \tag{5.3.30}$$

Equivalently, by subtracting the first from the second equation in (5.3.30), we obtain

$$\begin{aligned} \mu(\alpha_1^2 - 1) + \lambda \ln\left(\alpha_1^2 \alpha_3\right) &= 0, \\ \frac{\mu(\alpha_3^2 - \alpha_1^2)}{\alpha_1^2 \alpha_3} &= N. \end{aligned} \tag{5.3.31}$$

Next, using the definition of the Poisson function given by (5.3.16), if $\alpha_3 = a$, then $\alpha_1 = \alpha_3^{-\nu(a)}$, and (5.3.31) takes on the form

$$\begin{aligned} \mu(a^{-2\nu(a)} - 1) + \lambda\,(1 - 2\nu(a)) \ln a &= 0, \\ \frac{\mu(a^2 - a^{-2\nu(a)})}{a^{1-2\nu(a)}} &= N. \end{aligned} \tag{5.3.32}$$

Assuming constant Poisson function, $\nu(a) = \overline{\nu} = \lambda/(2(\mu + \lambda))$, then $\lambda = 2\mu\overline{\nu}/(1 - 2\overline{\nu})$ and (5.3.32) reduces to

$$\begin{aligned} a^{-2\overline{\nu}} + 2\nu \ln a &= 1, \\ \frac{\mu(a^2 - a^{-2\overline{\nu}})}{a^{1-2\overline{\nu}}} &= N. \end{aligned} \tag{5.3.33}$$

Next, noting that the first equation in (5.3.33) has the unique solution $a = 1$, we conclude that only under infinitesimal strain the Poisson function can be constant, but not under finite strain in general.

5.3.3 Bulk modulus

Volume changes in the isotropic hyperelastic models (5.2.25) and (5.2.28) can be quantified by the following *non-linear bulk modulus* [113], defined under the equitriaxial stretch $\mathrm{diag}(\alpha_1, \alpha_2, \alpha_3)$, with $\alpha_1 = \alpha_2 = \alpha_3 = a > 0$ (Figure 5.6),

$$\kappa = \frac{1}{3} \frac{\partial\,(\sigma_1 + \sigma_2 + \sigma_3)}{\partial(J - 1)}, \tag{5.3.34}$$

where $\{\sigma_i\}_{i=1,2,3}$ are the principal Cauchy stresses and $J = \alpha_1\alpha_2\alpha_3 = a^3$.

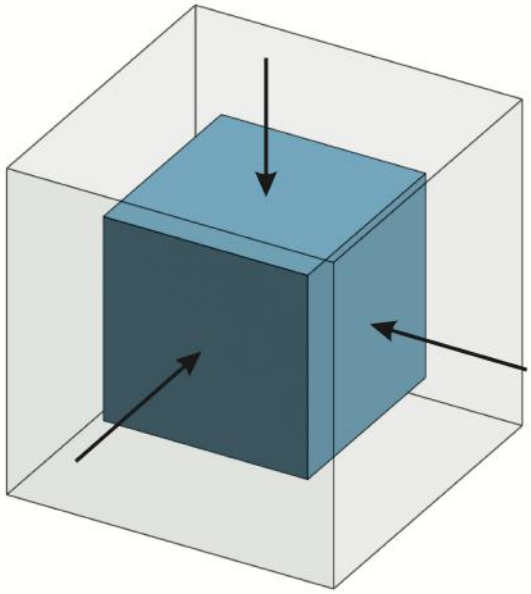

Figure 5.6: Cube deformed by hydrostatic compression.

Remark 5.3.3 *For a compressible isotropic material, the fact that the volume of the material is decreased by hydrostatic compression and increased by hydrostatic tension is expressed by the the pressure-compression (PC) inequalities stating that each principal stress is a tension or a compression if the corresponding principal stretch is an extension or a contraction, i.e.,* $\sigma_i (\alpha_i - 1) > 0$, $i = 1, 2, 3$ *[157, p. 155]. Physically, either or both of the following mean versions of the PC conditions are more realistic,*

$$\sigma_1 (\alpha_1 - 1) + \sigma_2 (\alpha_2 - 1) + \sigma_3 (\alpha_3 - 1) > 0, \tag{5.3.35}$$

or

$$\sigma_1 \left(1 - \frac{1}{\alpha_1}\right) + \sigma_2 \left(1 - \frac{1}{\alpha_2}\right) + \sigma_3 \left(1 - \frac{1}{\alpha_3}\right) > 0, \tag{5.3.36}$$

if not all principal stretches are equal to 1*. By [119], if the PC inequalities hold for the cell wall material, then these inequalities hold also for the open- and closed-cell models.*

As J quantifies the relative change of volume from the reference to the current configuration, assuming that J is close to 1 (i.e., for small or incremental volume changes), and setting $\sigma_1 = \sigma_2 = \sigma_3 = \sigma$, the non-linear bulk modulus (5.3.34) simplifies as follows,

$$\kappa = \lim_{J\to 1} \frac{\sigma}{J-1}. \tag{5.3.37}$$

For the neo-Hookean models (5.2.24) and (5.2.27), the respective bulk moduli given by (5.3.37) are constant and equal to

$$\begin{aligned} \kappa_w &= \frac{2\mu_w + 3\lambda_w}{3}, \\ \kappa_c &= \frac{2\mu_c + 3\lambda_c}{3}. \end{aligned} \tag{5.3.38}$$

Open-cell model. For the open-cell model (5.2.25), expressing the principal components of the Cauchy stress tensor as

$$\begin{aligned} \sigma_i^{(o)} = {} & \frac{\mu_w \rho_w^{(o)}(1+k)}{J_o^{2/3}} \left[J_o^{1/3}(1+k) - k - \frac{1}{J_o^{1/3}(1+k) - k} \right] \\ & + \frac{\lambda_w \rho_w^{(o)}(1+k)}{J_o^{2/3}} \frac{\ln\left[(1+k)^3 J_o - 3k(1+k)^2 J_o^{2/3} + 3k^2(1+k) J_o^{1/3} - k^3\right]}{J_o^{1/3}(1+k) - k}, \qquad i = 1,2,3, \end{aligned} \tag{5.3.39}$$

where $J_o = a^3$, and the non-linear bulk modulus given by (5.3.37) takes on the form

$$\begin{aligned} \kappa^{(o)} &= \lim_{J_o \to 1} \left\{ \frac{\mu_w \rho_w^{(o)}(1+k)}{J_o^{2/3}(J_o - 1)} \left[J_o^{1/3}(1+k) - k - \frac{1}{J_o^{1/3}(1+k) - k} \right] \right. \\ &\quad \left. + \frac{\lambda_w \rho_w^{(o)}(1+k)}{J_o^{2/3}(J_o - 1)} \frac{\ln\left[(1+k)^3 J_o - 3k(1+k)^2 J_o^{2/3} + 3k^2(1+k) J_o^{1/3} - k^3\right]}{J_o^{1/3}(1+k) - k} \right\} \\ &= \kappa_w \rho_w^{(o)} (1+k)^2 \\ &= \kappa_w \frac{3k^2}{1+k}. \end{aligned} \tag{5.3.40}$$

Note that $\overline{\mu}^{(o)}$ and $\kappa^{(o)}$ scale by the same factor, such that

$$\frac{\kappa^{(o)}}{\overline{\mu}^{(o)}} = \frac{\kappa_w}{\mu_w}. \tag{5.3.41}$$

This result is to be expected in the linear elastic limit since $\overline{\nu}^{(o)} = \nu_w$.

Closed-cell model. Similarly, for the closed-cell model (5.2.28), the non-linear bulk modulus defined by (5.3.37) is equal to

$$\begin{aligned}
\kappa^{(c)} &= \lim_{J_c\to 1}\left\{\frac{\mu_w\rho_w^{(c)}(1+k)}{J_c^{2/3}(J_c-1)}\left[J_c^{1/3}(1+k)-k-\frac{1}{J_c^{1/3}(1+k)-k}\right]\right. \\
&+\frac{\lambda_w\rho_w^{(c)}(1+k)}{J_c^{2/3}(J_c-1)}\frac{\ln\left[(1+k)^3J_c-3k(1+k)^2J_c^{2/3}+3k^2(1+k)J_c^{1/3}-k^3\right]}{J_c^{1/3}(1+k)-k} \\
&\left.+\frac{\rho_c^{(c)}}{J_c}\left(\mu_c\frac{J_c^{2/3}-1}{J_c-1}+\lambda_c\frac{\ln J_c}{J_c-1}\right)\right\} \\
&= \kappa_w\rho_w^{(c)}(1+k)^2+\kappa_c\rho_c^{(c)} \\
&= 3k\kappa_w+\kappa_c\frac{1}{(1+k)^3}.
\end{aligned} \tag{5.3.42}$$

Hence, for the open- and the closed-cell models with neo-Hookean cell walls, the non-linear bulk moduli given by (5.3.40) and (5.3.42), respectively, are constant.

5.3.4 Examples

For the the isotropic hyperelastic models (5.2.25) and (5.2.28), we illustrate the non-linear elastic behaviour under the studied deformations as follows:

- In Figure 5.7, for the open-cell models, defined by (5.2.25), with varying thickness-to-length ratio of the cell wall, $k \in \{0.1, 0.2, 0.3\}$, and fixed cell wall material parameters, $\mu_w = 1$ and $\nu_w = 0.49$, we plot: (A) the non-linear shear modulus $\widehat{\mu}^{(o)}(\gamma)$, given by (5.3.9), evaluated under varying simple shear, with $0 < \gamma < 0.5$, superposed on infinitesimal axial stretch, and (B) the non-linear shear

modulus $\widetilde{\mu}^{(o)}(a)$, given by (5.3.10), evaluated under infinitesimal shear superposed on varying compression or tension, with $0.75 < a < 1.25$.

- In Figure 5.8, for the open-cell models (5.2.25), with varying thickness-to-length ratio of the cell wall, $k \in \{0.1, 0.2, 0.3\}$, and fixed material parameters, $\mu_w = 1$ and $\nu_w = 0.49$, we show: (A) the non-linear stretch modulus $E^{(o)}(a)$, given by (5.3.22), and (B) the non-linear Poisson's ratio $\nu^{(o)}(a)$, given by (5.3.20), both evaluated under varying compression or tension, with $0.75 < a < 1.25$.

- In Figure 5.9, for the closed-cell models, given by (5.2.28), with varying shear modulus of the cell core, $\mu_c \in \{0.01, 0.05, 0.1\}$, and fixed cell wall parameters, $\mu_w = 1$, $\nu_w = \nu_c = 0.49$, and $k = 0.1$, we plot: (A) the non-linear shear modulus $\widehat{\mu}^{(c)}(\gamma)$, given by (5.3.13), evaluated under varying simple shear, with $0 < \gamma < 0.5$, superposed on infinitesimal stretch, and (B) the non-linear shear modulus $\widetilde{\mu}^{(c)}(a)$, given by (5.3.14), evaluated under infinitesimal shear superposed on varying compression or tension, with $0.75 < a < 1.25$.

- In Figure 5.10, for the closed-cell models (5.2.28), with varying shear modulus of the cell core, $\mu_c \in \{0.01, 0.05, 0.1\}$, and fixed cell wall parameters, $\mu_w = 1$, $\nu_w = \nu_c = 0.49$, and $k = 0.1$, we show: (A) the non-linear stretch modulus $E^{(c)}(a)$, defined by (5.3.25), and (B) the non-linear Poisson's ratio $\nu^{(c)}(a)$, defined by (5.3.24), both evaluated under varying compression or tension, with $0.75 < a < 1.25$.

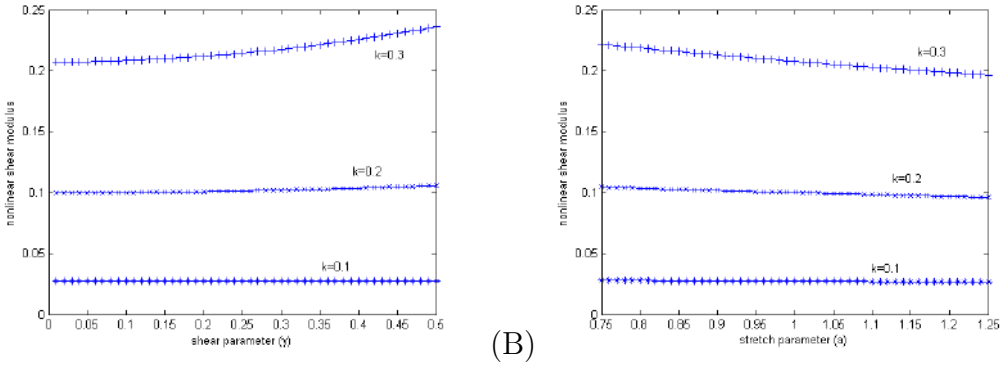

(A) (B)

Figure 5.7: Open-cell models (5.2.25) with varying thickness-to-length ratio of cell wall, $k \in \{0.1, 0.2, 0.3\}$, and fixed $\mu_w = 1$, $\nu_w = 0.49$, showing: (A) non-linear shear modulus $\widehat{\mu}^{(o)}(\gamma)$ of (5.3.9), evaluated under varying simple shear ($0 < \gamma < 0.5$) superposed on infinitesimal stretch, and (B) non-linear shear modulus $\widetilde{\mu}^{(o)}(a)$ of (5.3.10), evaluated under infinitesimal shear superposed on varying compression or tension ($0.75 < a < 1.25$).

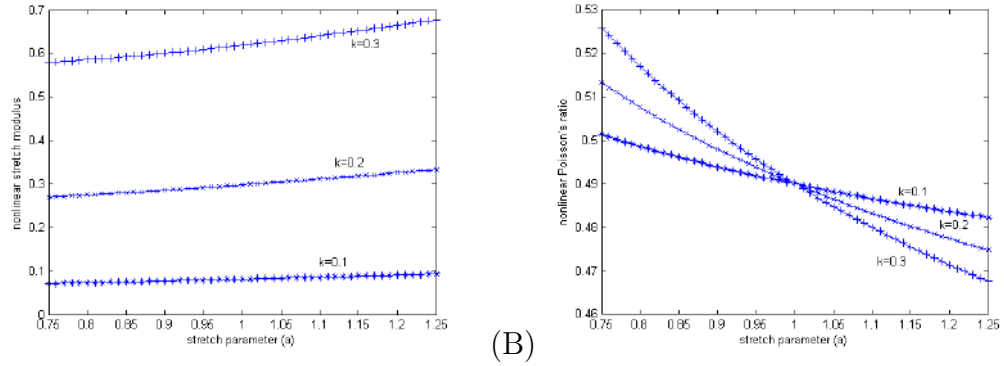

(A) (B)

Figure 5.8: Open-cell model (5.2.25) with varying thickness-to-length ratio of cell wall, $k \in \{0.1, 0.2, 0.3\}$, and fixed $\mu_w = 1$, $\nu_w = 0.49$, showing: (A) non-linear stretch modulus $E^{(o)}(a)$ of (5.3.22), and (B) non-linear Poisson's ratio $\nu^{(o)}(a)$ of (5.3.20), both evaluated under varying compression or tension ($0.75 < a < 1.25$).

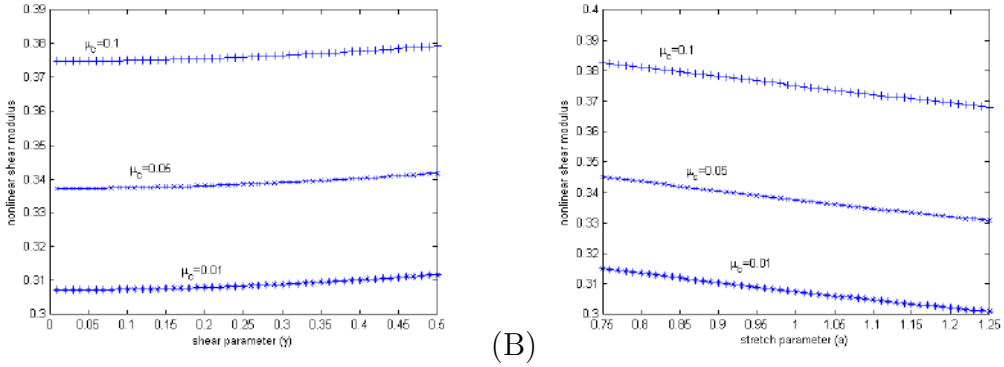

(A) (B)

Figure 5.9: Closed-cell model (5.2.28) with varying shear modulus of cell core, $\mu_c \in \{0.01, 0.05, 0.1\}$ and fixed $\mu_w = 1$, $\nu_w = \nu_c = 0.49$, and $k = 0.1$, showing: (A) non-linear shear modulus $\widehat{\mu}^{(c)}(\gamma)$ of (5.3.13), evaluated under varying simple shear ($0 < \gamma < 0.5$) superposed on infinitesimal stretch, and (B) non-linear shear modulus $\widetilde{\mu}^{(c)}(a)$ of (5.3.14), evaluated under infinitesimal shear superposed on varying compression or tension ($0.75 < a < 1.25$).

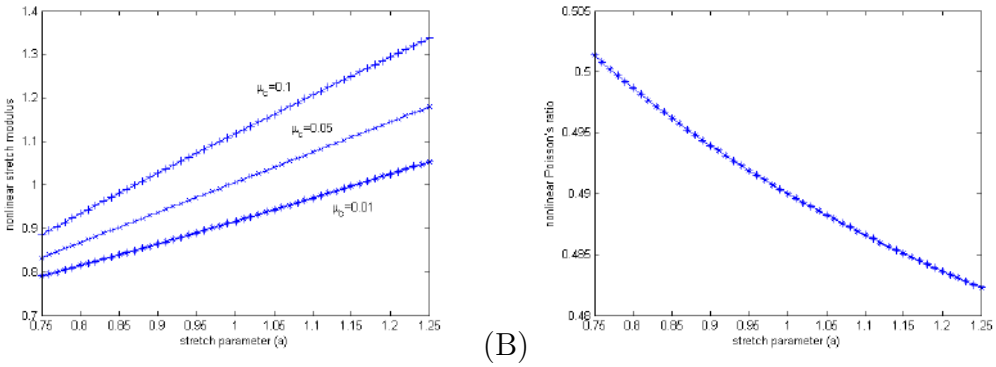

(A) (B)

Figure 5.10: Closed-cell model (5.2.28) with varying shear modulus of cell core, $\mu_c \in \{0.01, 0.05, 0.1\}$ and fixed $\mu_w = 1$, $\nu_w = \nu_c = 0.49$, and $k = 0.1$, showing: (A) non-linear stretch modulus $E^{(c)}(a)$ of (5.3.25), and (B) non-linear Poisson's ratio $\nu^{(c)}(a)$ of (5.3.24), both evaluated under varying compression or tension ($0.75 < a < 1.25$).

Discussion of examples

Our illustrative examples show that, for the open-cell model:

- Under simple shear superposed on infinitesimal stretch, the non-linear shear modulus increases slightly or remains almost constant as the shear parameter, satisfying $0 < \gamma < 0.5$, increases (Figure 5.7A).

- Under infinitesimal shear superposed on finite axial stretch, the non-linear shear modulus decreases or remains almost constant as the stretch ratio, satisfying $0.75 < a < 1.25$, increases (Figure 5.7B).

- Under increasing finite axial stretch, the non-linear stretch modulus increases, while the Poisson function decreases (Figure 5.8).

- As the thickness-to-length ratio of the cell wall, k, increases, the non-linear shear and stretch parameters increase, while the non-linear Poisson's ratio decreases in tension and increases in compression (Figures 5.7 and 5.8).

Analogous properties were found for the closed-cell model with empty cells (results not shown). In addition, when the closed cells are filled with an elastic core that has the same Poisson's ratio as the cell walls:

- The non-linear shear and stretch moduli increase as the shear modulus of the cell core, μ_c, increases (Figures 5.9 and 5.10A).

- When the Poisson's ratios for the cell wall and for the different cell core materials are equal, the non-linear Poisson's ratio for the closed-cell model does not change with the cell core (Figure 5.10B).

Note the bulk modulus is only defined in the linear elastic limit and is constant, whereas the other elastic moduli are functions of deformation. Hence, no plots of the bulk modulus are given.

5.4 Backwards multiscale method

There are many experimental difficulties in recording accurate cell wall stiffness for biological cellular materials. These difficulties arise from: (i) the size of the cell walls and the testing equipment required for measuring non-linear behaviour accurately; (ii) changes in properties between in vivo and in vitro - an extracted cell wall will have a different stiffness if it is within a tissue, as environmental conditions (such as hydration) will change. The power of using the multiscale framework [119] as a 'backwards multiscale method' is that it is able to extract information from macroscopic tests and predict cell wall properties that may be otherwise impossible to find.

In this section, we will apply the multiscale framework in reverse to experimental data for the Jonagord apple, Figure 5.11 [125], to derive the cell wall properties. The advantage of this data is that three sets of measurements were taken, for varying cell core pressures (manipulated by absorption of mannitol solution, with different osmotic potentials). This means that we can distinguish the cell core effect and find the common cell wall data between the data sets. No experimental data could be found to give a complete validation of the derived cell wall material, so we highlight that this cell wall derivation is for illustrative purposes only.

The experimental test [125] was performed on a rectangular specimen ($11 \times 5 \times 2$mm) bonded by an adhesive at the ends to a tensile test rig. Three cycles of uniaxial tensile loading and unloading, to zero stress, were performed, then elongation until tissue failure. Tensile loading happened at a rate of $6.6\mu ms^{-1}$. Results are shown in Figure 5.11 [1].

[1]Reprinted from Postharvest Biology and Technology, 44, Oey ML *et al.*, Effect of turgor on micromechanical and structural properties of apple tissue: a quantitative analysis, 240-247, Copyright (2007), with permission from Elsevier.

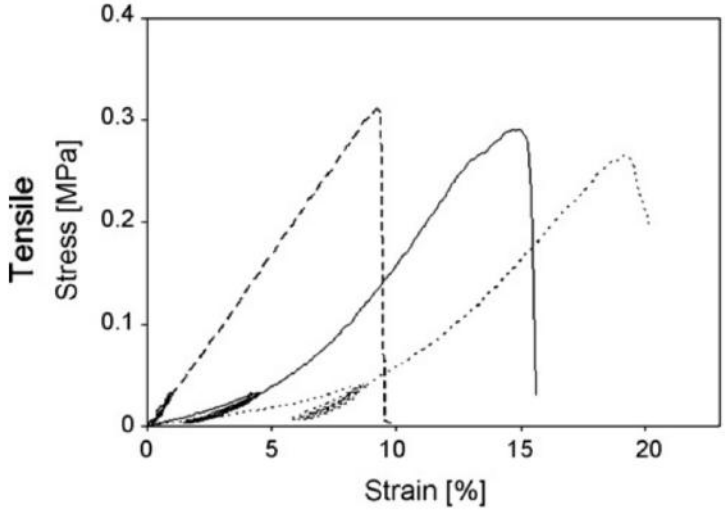

Figure 5.11: Jonagord apple [125] tensile data for three apple tissues, oversaturated, fresh and overripe (from left to right).

5.4.1 Model derivation

The isotropic incompressible Fung strain energy density function [57] has the capacity to capture the strain stiffening effects caused by the fibres within the cell walls, so we will use it for our cell wall material. This is then incorporated in the mesoscopic model, which we then calibrate against the experimental data. The cell wall strain energy density function is

$$\mathcal{W}_w = \frac{\mu_w}{2b}\left[e^{b(I_1-3)} - 1\right], \tag{5.4.1}$$

where μ_w is the infinitesimal shear modulus of the cell wall, b is the stiffening factor, and I_1 is the first strain invariant of the deformation.

We assume that the cell core can be represented with a simple incompressible neo-Hookean model

$$\mathcal{W}_c = \frac{\mu_c}{2}\big(I_1 - 3\big), \tag{5.4.2}$$

where μ_c is the infinitesimal shear modulus of the cell core.

The mesoscopic strain energy density function for the closed cell model is then

$$\begin{aligned}\mathcal{W}^{(c)} =& \frac{\mu_w \rho_w^{(c)}}{2b}\left\{e^{b[(1+k)^2(i_1^2-2i_2)-2k(1+k)i_1-3(1-k^2)]}-1\right\}\\ &+\frac{\mu_c\rho_c^{(c)}}{2}\big(i_1^2-2i_2-3\big),\end{aligned} \tag{5.4.3}$$

where $\rho_w^{(c)}$ and $\rho_c^{(c)}$ are the volume fractions of cell wall and cell core material in a representative unit volume (note that $\rho_w^{(c)}$ does not include the volume of nodes), respectively, k is the wall width-to-length ratio, and i_1 and i_2 are the first and second deformation invariants.

In terms of principal stretches, α_i, for the mesoscopic structure, this takes the form

$$\begin{aligned}\mathcal{W}^{(c)} =& \frac{\mu_w \rho_w^{(c)}}{2b}\left\{e^{b[(1+k)^2(\alpha_1^2+\alpha_2^2+\alpha_3^2)-2k(1+k)(\alpha_1+\alpha_2+\alpha_3)-3(1-k^2)]}-1\right\}\\ &+\frac{\mu_c\rho_c^{(c)}}{2}\big(\alpha_1^2+\alpha_2^2+\alpha_3^2-3\big).\end{aligned} \tag{5.4.4}$$

The corresponding principal stresses are

$$\begin{aligned}\sigma_i =& \mu_w\rho_w^{(c)}\left[(1+k)^2\alpha_i^2-k(1+k)\alpha_i\right]e^{b[(1+k)^2(\alpha_1^2+\alpha_2^2+\alpha_3^2)-2k(1+k)(\alpha_1+\alpha_2+\alpha_3)-3(1-k^2)]}\\ &+\mu_c\rho_c^{(c)}\alpha_i^2-p.\end{aligned} \tag{5.4.5}$$

As we assume the cell walls, core and joints are all incompressible, the mesoscopic bulk material is also incompressible and therefore $\alpha_1\alpha_2\alpha_3 = 1$. The mesoscopic material is also isotropic and subject to uniaxial stretch, then $\alpha_1 = \alpha$ and $\alpha_2 = \alpha_3 = \frac{1}{\sqrt{\alpha}}$. A common assumption is that the out of plane stresses are zero, i.e.

$$\begin{aligned}\sigma_3 =& \mu_w\rho_w^{(c)}\left[(1+k)^2\frac{1}{\alpha}-k(1+k)\frac{1}{\sqrt{\alpha}}\right]e^{b[(1+k)^2(\alpha^2+\frac{2}{\alpha})-2k(1+k)(\alpha+\frac{2}{\sqrt{\alpha}})-3(1-k^2)]}\\ &+\mu_c\rho_c^{(c)}\frac{1}{\alpha}-p=0.\end{aligned} \tag{5.4.6}$$

In this case, we can calculate the hydrostatic pressure

$$p = \mu_w \rho_w^{(c)} \left[(1+k)^2 \frac{1}{\alpha} - k(1+k) \frac{1}{\sqrt{\alpha}} \right] e^{b[(1+k)^2(\alpha^2+\frac{2}{\alpha})-2k(1+k)(\alpha+\frac{2}{\sqrt{\alpha}})-3(1-k^2)]} + \mu_c \rho_c^{(c)} \frac{1}{\alpha}, \tag{5.4.7}$$

and obtain an expression for stress in the direction of the tensile force

$$\sigma_1 = \mu_w \rho_w^{(c)} \left[(1+k)^2 (\alpha^2 - \frac{1}{\alpha}) - k(1+k)(\alpha - \frac{1}{\sqrt{\alpha}}) \right] e^{b[(1+k)^2(\alpha^2+\frac{2}{\alpha})-2k(1+k)(\alpha+\frac{2}{\sqrt{\alpha}})-3(1-k^2)]} + \mu_c \rho_c^{(c)} (\alpha^2 - \frac{1}{\alpha}). \tag{5.4.8}$$

We can calibrate (5.4.8) to the experimental data, and find values for cell wall material parameters (μ_w and b) for each of the three cases provided. For each dataset, the values for the cell core stiffness μ_c can vary.

5.4.2 Experimental parameters

Average cell area over 2D cross sections have been recorded for high, normal and low pressure. This allows for an approximation of the cell radius and volume. Cell thickness was not recorded in this experiment, but [96] uses transmission electron microscopy and MatLab analysis to calculate the cell wall thickness of the Jonagord apple, thus a recording of $1.67 + -0.71 \mu m$ is used here. In order to approximate the cell wall thickness to length ratio k and the volume fractions $\rho_w^{(c)}$ and $\rho_c^{(c)}$, an idealised geometric assumption is made. An optimal, ordered, cell packing in three dimensions, with full cell-cell contact (no gaps) is a tetrakaidecahedral packing [65]. The resulting geometric parameters are summarised in the table below.

Jonagord apple parameters			
Parameter	Symbol	Value	Calculation
Cell wall pair thickness	t	$3.34\mu m$	Double recorded thickness (cell wall pair) [96]
Cell volume	V_T	$2.74\times10^6\mu m^3$	As recorded [125]
Edge length	$\overline{L}$	$62.33\mu m$	$V_T = 8\sqrt{2}\overline{L}^3$
Effective edge length	L	$58.99\mu m$	$L = \overline{L} - t$
Thickness to edge ratio	κ	0.0536	$\kappa = t/\overline{L}$
Thickness to effective edge ratio	k	0.0566	$l = t/L$
RVF of cell walls	ρ_w	0.0566	From geometry
RVF of cell core	ρ_c	0.9434	From geometry

5.4.3 Model calibration

A built-in procedure is used in MatLab to calibrate the mesoscopic material model against the experimental data. The absolute residual norm is minimised, where the norm is given as

$$||r||_2^2 = \sum[\sigma_1(\lambda) - \sigma_{exp}]^2, \tag{5.4.9}$$

where σ_{exp} is the experimentally recorded stress in the first direction, extracted from Figure 5.11 using 'grabit' in MatLab.

The residual norms for each dataset (relating to the low, medium and high core stiffness) is combined in the minimisation process with equal weighting, such that the three samples relate to a shared shear modulus μ_w and stiffening factor b.

Examining the data of Figure 5.11, sudden changes in the slope indicate some sort of damage or failure, so these data points should be excluded. Further, there

are cyclic tests included in these data sets which are also excluded. There are two logical approaches to analysing the given data sets, which are both explored:

(i) Consider only data points up to the onset of damage,

(ii) Consider only data points up to a prescribed stretch.

Approach (i)

Here the data is resampled, so there are 100 data points in each data set, shown in Figure 5.12. Excluded data points are shown in black. The 'fminsearch' MatLab function is used as the data sets do not have the same λ range. An objective function produces an error, dictated by (5.4.9), with equal weighting for each data set. Penalties are included to enforce positive parameters.

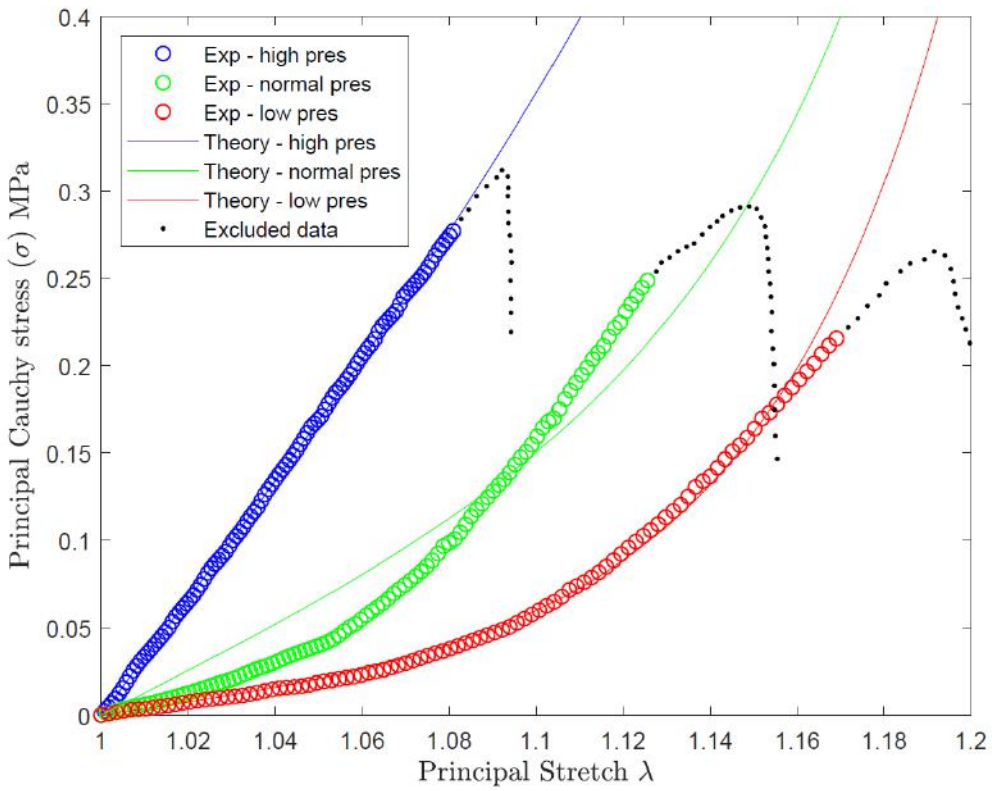

Figure 5.12: Experimental data (excluding damage) fitted with the multiscale Fung model, where black points are excluded in the fit.

The optimised parameters are $\mu_w = 1.9767$, $b = 16.057$, and for the cell cores (low pres) $\mu_c = 0$, (med pres) $\mu_c = 0.3189$ and (high pres) $\mu_c = 1.044$, with

residual norm $||r||_2^2 = 0.039$. The fit works well for both low and high pressures, where either the Fung or neo-Hookean models dominate. However, for the normal pressure the fit is not so good.

Approach (ii)

The data is resampled, such that there are 100 data points in the data range $1 \leq \lambda \leq 1.08$ and 8% deformation is the maximum deformation considered, as shown in Figure 5.13. Excluded data points are shown in black. The more appropriate 'lsqcurvefit' MatLab function is used as the data sets share the same λ range and a single, combined objective function can be used, with equal weighting for each data set. Lower limits are used to enforce positive parameters.

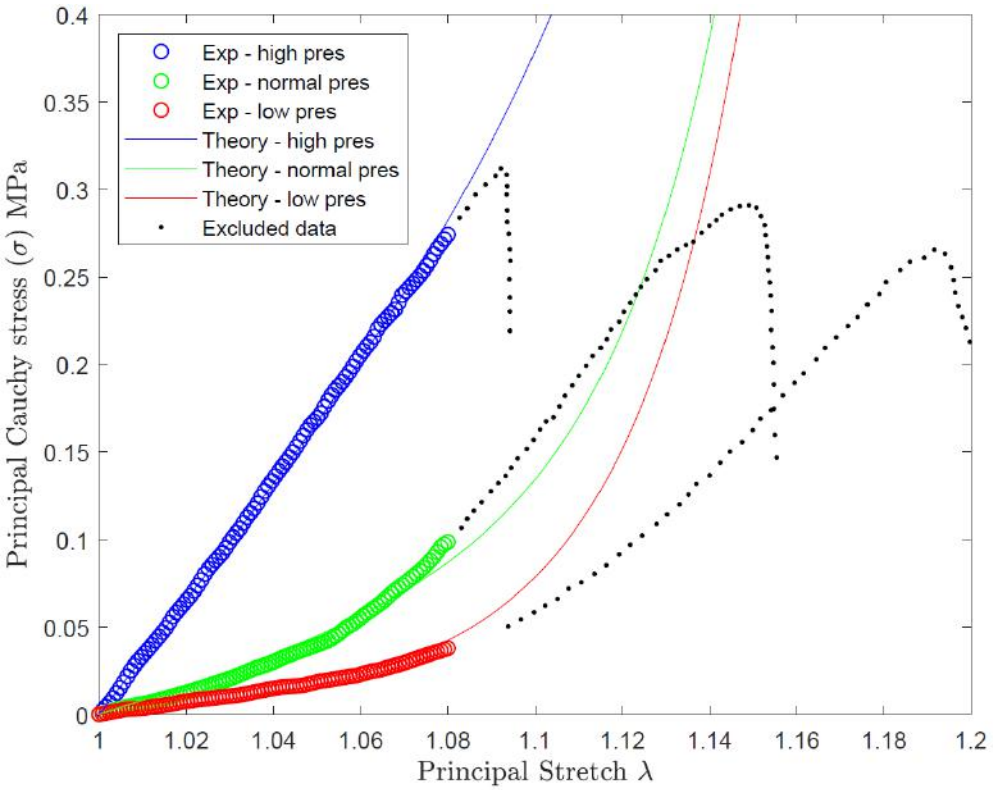

Figure 5.13: Experimental data ($\lambda \leq 1.08$) fitted with the multiscale Fung model, where black points are excluded in the fit.

The optimised parameters are $\mu_w = 1.3760$, $b = 36.6717$ and for the cell cores (low pres) $\mu_c = 0.006$, (med pres) $\mu_c = 0.1976$ and (high pres) $\mu_c = 1.0590$, with residual norm $||r||_2^2 = 0.0031$. Within the data range, there is strong agreement

between the fit and experimental results, given by a norm which is of one order of magnitude smaller than case (i). Outside of this range, stiffness increases more sharply than the experimental data due to a higher stiffening factor.

5.4.4 Cell wall approximation

With the Fung cell wall material model approximation and the fitted parameters from the mesoscopic material model, we now have functions and parameter values for both the cell wall and the continuum material, which could be used and validated in further study. The Fung models for case (i) and (ii) are given by

$$\mathcal{W}_w = \frac{\mu_w}{2b}\left[e^{b(I_1-3)} - 1\right], \tag{5.4.10}$$

with $\mu_w = 1.9767$, $b = 16.057$ for case (i) and $\mu_w = 1.3760$, $b = 36.6717$ for case (ii). Assuming no out of plane stress, Figure 5.14 shows a stress plot of these functions, given by

$$\sigma_w = \mu_w\Big(\lambda_1^2 - \frac{1}{\lambda_1}\Big)e^{b(\lambda_1^2+\frac{2}{\lambda_1}-3)}. \tag{5.4.11}$$

5.5 New material models in FEBio

The open and closed cell mesoscopic material models have been implemented in FEBio. This was written in C++ code and compiled into a .dll plugin, which can be downloaded and used by other FEBio users. For validation, the computational results are compared to the analytical predictions. We find that in uniaxial deformation, the axial stress from the theory and simulation agree with accuracy 10^{-6}. This was tested with neo-Hookean cell wall material $\mu_w = 1, \lambda_w = 4$ (which corresponds to $\nu = 0.4$ in the infinitesimal limit) and for closed cell - a soft neo-Hookean cell core $\mu_c = 0.01, \lambda_c = 0.49$ (which corresponds to $\nu = 0.49$ in the infinitesimal

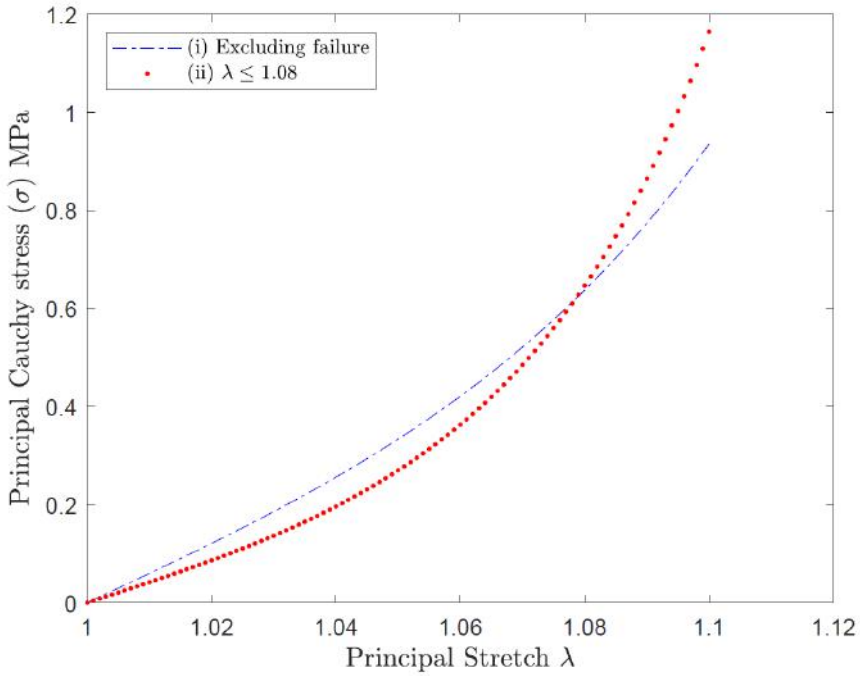

Figure 5.14: Predicted cell wall behaviour from the Fung multiscale model.

limit). The boundary conditions were as follows: bottom face is fixed in the Z direction and prescribed in the Z direction on the top. All faces are free in the X and Y plane, however small cubes are attached to the top and bottom faces with fixed X and Y to avoid multiple solutions. Clearly, with such strong agreement between theory and simulation, the boundary conditions suffice for a homogeneous deformation.

5.5.1 Derivation of the spatial elasticity tensor

The spatial elasticity tensor $\mathbb{C}$ is required for the linearisation of elasticity problems and is calculated here in order for a new hyperelastic material to be implemented in FEBio. $\mathbb{C}$ is of rank four and possesses major symmetries such that [73]

$$\mathbb{C} = \mathbb{C}^T \quad \text{or} \quad \mathbb{C}_{ABCD} = \mathbb{C}_{CDAB}, \tag{5.5.1}$$

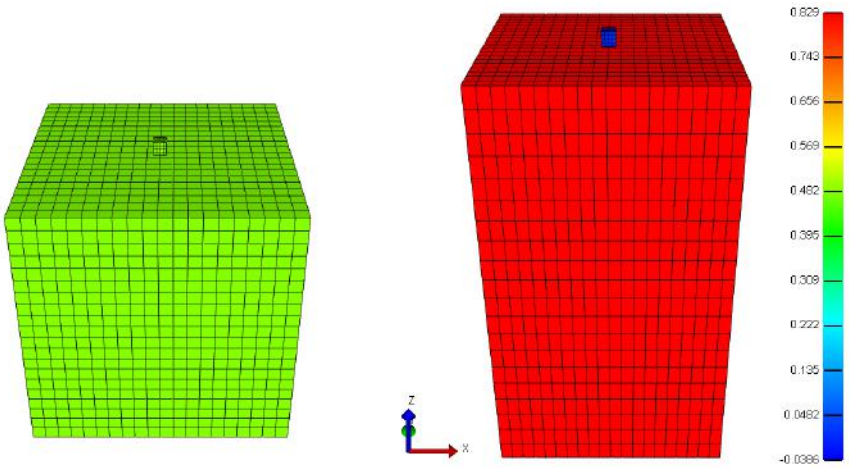

Figure 5.15: Unit cube of closed cell material (left) subject to uniaxial tension $\alpha_3 = 1.5$ (right), where colour bar represents stress in Z direction (in right only).

leaving 21 independent components, but then also minor symmetries such that

$$\mathbb{C}_{ABCD} = \mathbb{C}_{BACD} = \mathbb{C}_{ABDC}, \tag{5.5.2}$$

leaving only 9 independent components.

In spectral form the spatial tensor can be expressed in terms of the principal stretches

$$\begin{aligned}\mathbb{C} = &\sum_{a,b=1}^{3} J_m^{-1}\alpha_a^2\alpha_b\frac{\partial S_a}{\partial \alpha_b}\hat{\mathbf{n}}_a\otimes\hat{\mathbf{n}}_a\otimes\hat{\mathbf{n}}_b\otimes\hat{\mathbf{n}}_b \\ &+\sum_{\substack{a,b=1\\a\neq b}}^{3} J_m^{-1}\frac{\sigma_a\alpha_a^2-\sigma_a\alpha_b^2}{\alpha_b^2-\alpha_a^2}(\hat{\mathbf{n}}_a\otimes\hat{\mathbf{n}}_b\otimes\hat{\mathbf{n}}_a\otimes\hat{\mathbf{n}}_b+\hat{\mathbf{n}}_a\otimes\hat{\mathbf{n}}_b\otimes\hat{\mathbf{n}}_b\otimes\hat{\mathbf{n}}_a),\end{aligned} \tag{5.5.3}$$

where S_a is the second Piola Kirchhoff stress $S_a = \sigma_a J/\alpha_a^2$ and $\hat{\mathbf{n}}_a$ are the principal spatial directions, which are the orthonormal eigenvectors of $\mathbf{B}$. In the case where $\alpha_a^2 = \alpha_b^2$ we find $\frac{0}{0}$ so we apply l'Hôpital's rule as follows:

$$\begin{aligned}\lim_{\alpha_b\to\alpha_a}\frac{\sigma_a\alpha_a^2-\sigma_a\alpha_b^2}{\alpha_b^2-\alpha_a^2} &= \Big(\frac{\partial\sigma_b}{\partial\alpha_b}\alpha_a^2-\frac{\partial\sigma_a}{\partial\alpha_b}\alpha_b^2-2\alpha_b\sigma_a\Big)\frac{1}{2\alpha_b} \\ &= \frac{1}{2}\alpha_a\Big(\frac{\partial\sigma_b}{\partial\alpha_b}-\frac{\partial\sigma_a}{\partial\alpha_b}\Big)-\sigma_a.\end{aligned} \tag{5.5.4}$$

5.5.2 Example with neo-Hookean cell walls

For the mesoscopic model with neo-Hookean beams our base strain energy density function will take the form

$$\mathcal{W}(I_1, I_2, I_3) = \frac{\mu}{2}(I_1 - 3) - \mu \ln I_3^{1/2} + \frac{\lambda}{2}\left(\ln I_3^{1/2}\right)^2, \tag{5.5.5}$$

where μ and λ are real positive constants.

From Section 5.2.4, we can calculate the strain energy density function for the mesoscopic cellular structure as (in terms of principal stretches)

$$\begin{aligned}\mathcal{W}^{(o)}(\alpha_1, \alpha_2, \alpha_3) = \frac{\rho_w \mu}{2}\Big[&(1+k)^2(\alpha_1^2 + \alpha_2^2 + \alpha_3^2) - 2k(1+k)(\alpha_1 + \alpha_2 + \alpha_3) \\ &+ 3k^2 - 3\Big] \\ &- \rho_w \mu \ln\Big[(1+\rho)^3(\alpha_1\alpha_2\alpha_3) - k(1+k)^2(\alpha_1\alpha_2 + \alpha_1\alpha_3 + \alpha_2\alpha_3) \\ &+ k^2(1+k)(\alpha_1 + \alpha_2 + \alpha_3) - k^3\Big] \\ &+ \frac{\rho_w \lambda}{2}\Big\{\ln\big[(1+k)^3(\alpha_1\alpha_2\alpha_3) - k(1+k)^2(\alpha_1\alpha_2 + \alpha_1\alpha_3 + \alpha_2\alpha_3) \\ &+ k^2(1+k)(\alpha_1 + \alpha_2 + \alpha_3) - k^3\big]\Big\}^2.\end{aligned} \tag{5.5.6}$$

The principal Cauchy stress is then calculated as

$$\sigma_i = \rho_w(1+k)\alpha_i J_m^{-1}\left[\mu\left(c_i - \frac{1}{c_i}\right) + \lambda\left(\frac{\ln C}{c_i}\right)\right], \tag{5.5.7}$$

where for brevity,

$$c_i = (1+k)\alpha_i - k \tag{5.5.8}$$

and

$$C = \sum_{i=1}^{3} c_i = (1+k)^3 i_3 - k(1+k)^2 i_2 + k^2(1+k)i_1 - k^3. \tag{5.5.9}$$

Spatial elasticity tensor $\mathbb{C}$:

$$\mathbb{C}_{iiii} = J_m^{-1}\alpha_i^3\frac{\partial S_i}{\partial \alpha_i} \tag{5.5.10}$$

$$= \rho_w(1+\rho)\alpha_i J_m^{-1}\Big[\mu\left(\rho + \frac{2c_i+\rho}{c_i^2}\right) \tag{5.5.11}$$

$$+ \lambda\frac{\alpha_i(\rho+1) - (2c_i+\rho)\ln C}{c_i^2}\Big], \tag{5.5.12}$$

$$\mathbb{C}_{iijj} = J_m^{-1}\alpha_i^2\alpha_j\frac{\partial S_i}{\partial \alpha_j} \tag{5.5.13}$$

$$= \rho_w(1+\rho)\alpha_i\alpha_j J_m^{-1}\lambda\frac{\rho+1}{c_i c_j}, \tag{5.5.14}$$

$$\mathbb{C}_{ijij} = \mathbb{C}_{ijji} = \frac{\sigma_j\alpha_i^2 - \sigma_i\alpha_j^2}{\alpha_j^2 - \alpha_i^2} \tag{5.5.15}$$

$$= \rho_w(1+\rho)J_m^{-1}\alpha_j\alpha_i\Big[\mu\left(\alpha_i c_j - \alpha_j c_i + \frac{\alpha_j}{c_i} - \frac{\alpha_i}{c_j}\right) \tag{5.5.16}$$

$$+ \lambda\left(\frac{\alpha_i\ln C}{c_j} - \frac{\alpha_j\ln C}{c_i}\right)\Big]\frac{1}{\alpha_j^2 - \alpha_i^2}. \tag{5.5.17}$$

When $\alpha_j^2 = \alpha_i^2$, applying l'Hôpital's rule, we have

$$\mathbb{C}_{ijij} = \mathbb{C}_{ijji} = 0.5\alpha_i\left(\frac{\partial\sigma_j}{\partial\alpha_j} - \frac{\partial\sigma_i}{\partial\alpha_j}\right) - \sigma_i, \tag{5.5.18}$$

where

$$\frac{\partial\sigma_i}{\partial\alpha_i} = \rho_w(1+\rho)\left[\mu\left(c_i + \rho + \frac{\rho}{c_i^2} + \frac{1}{c_i}\right) + \lambda\frac{(c_i+\rho)(1-\ln C)}{c_i^2}\right]J_m^{-1}, \tag{5.5.19}$$

and, for $i \neq j$,

$$\frac{\partial\sigma_i}{\partial\alpha_j} = \rho_w(1+\rho)\left\{\mu\left(\frac{\alpha_i}{c_i\alpha_j} - \frac{\alpha_i c_i}{\alpha_j}\right) + \lambda\left[\frac{\alpha_i(\rho+1)}{c_i c_j} - \frac{\ln C\alpha_i}{c_i\alpha_j}\right]\right\}J_m^{-1}. \tag{5.5.20}$$

5.6 Summary

For stretch-dominated cellular structures with open or closed cells made from an arbitrary homogeneous isotropic hyperelastic material, continuum isotropic hyperelastic models at a mesoscopic level were constructed analytically in [118,119]. To gain further insight into the non-linear elastic behaviour of these models, here, we specialised to the case with neo-Hookean cell components, and derived explicitly the non-linear shear, stretch, and bulk moduli and Poisson function defined in [113].

For the continuum models of stretch-dominated structures with open or closed cells investigated here, the non-linear elastic parameters were predicted analytically from the material and geometric parameters at the cell level, which were provided a priori. Conversely, continuum models with specific non-linear elastic properties may be designed by selecting suitable material and geometric properties of the components, or these cell level parameters can be derived from experimental measurements on cellular tissues, as in Section 5.4. The limitations in our ability to perform validation tests for the open-cell model, is explored in Appendix A.

The exploration of the non-linear parameters has been published in the International Journal of Non-linear Mechanics [144] and has been presented (along with the backwards multiscale method) at the 10th European Solid Mechanics Conference, Bologne, Italy (July 2018).

Chapter 6

Conclusions and perspectives

6.1 Overview

The aim of this thesis was to illuminate some of the behaviours of deforming cellular materials and the links to their composition such as the cell wall, cell core and cohesive middle lamella. This aim was achieved by studying cell wall pairs and complex cellular tissues under shear deformation, in addition to exploring multi-scale models built from microscopic observations. The use of non-linear materials and large deformation frameworks allows for changes in material properties as the deformation progresses, which is readily observed in soft biological material, especially fibrous composites. Our results match experimental observations and are useful in directing further research.

Simple and generalised shear have been mathematically analysed for over half a century, yet this is the first time they have been put in the context of contact mechanics, where the permissible forms of deformed walls are combined with the complementarity conditions of gap size and contact pressure. The exercise with isotropic Mooney-Rivlin cell walls is omitted from the thesis, however this gives detail on the possible quadratic forms of the deformed walls which do not conflict with the complementarity conditions. By including transverse isotropy, the theoretical results depend on a fibre direction and a stiffness in this direction. If

the fibre direction is parallel to the direction of shear, the isotropic case is recovered. For simplified solutions, we assume the fibres to be much stiffer than the surrounding matrix, but the role of the relative stiffness and a general fibre angle could be further explored. In addition, the presence of intracellular pressure is proven to have a cohesive effect on contacting cell wall pairs.

In many soft fruits it is desirable for the tissue to fail by cell bursting rather than cell-cell debonding, as it is the cell cytoplasm which contains the flavour and juices. There is relatively little literature on the debonding failure mode as this is harder to test and decipher from mixed mode results. A limit of the finite elasticity approach is that no damage can occur in the cell walls, such that cell-cell debonding can only be explored and not the transition from cell bursting as the primary failure mode. However, as the information on debonding is limited, our investigation provides valuable insights. Finite element simulations of multibody contact problems are usually inefficient due to the algorithms that detect and resolve contact. As debonding cellular materials can quickly become cumbersome, a two step procedure is developed to increase speed and reliability. In this case, the boundary conditions play an important role in limiting the solution space to allow tractable, measurable results. Frictionless non-penetrative contact is employed between cells and cohesion is implemented through normal pressure on the cell walls. Cohesion delays the onset of debonding, but once the debonding force has overcome a certain limit, the opening increases in size at a constant rate. The cell core affects the structure through its stiffness (approximated by a soft elastic inclusion) and a normal pressure acting on the cell walls. The volumetric constraint in the cell core also delays gap initiation, but here the opening does not increases in size at the same rate, as the softer the core, the more quickly the gap grows. Therefore, dehydrating cells will both cause a pull at the intercellular bonds and increase the speed of gap growth. This is in agreement with the experimental observations that ageing and cooked plants debond more readily.

Expanding the scale of our focus further, we consider continuum approaches for isotropic cellular materials using the frameworks of [118,119]. The assumptions here are that the cell walls primarily deform by triaxial stretch, due to the structural architecture, and that the cell joints do not deform significantly. This framework extends any hyperelastic isotropic material model to a mesoscopic scale, but only the compressible neo-Hookean strain-energy function is formally explored. In this case, the non-linear shear modulus, stretch modulus, Poisson's function and bulk modulus are explicitly derived for the cellular material comprising of neo-Hookean cell walls. These moduli, which quantify multiscale relationships between the structure and cell wall properties, are the most mathematically 'pure' elastic characteristics of a soft material, and are in the process of being adopted within the materials testing community. However, it will be some time before they are adopted within food sciences. Possibly the most useful aspect of the multiscale method (to experimentalists) is the backward multiscale process proposed in this thesis, as this can enlighten us to the possible cell wall properties of a biological structure when only the bulk tissue behaviour is known. Although this method is powerful, there are currently limitations in our ability to perform experimental validation. This is either due to the restrictions imposed by the modelling assumptions, or the limitations of experimental processes. In Appendix A, these limitations are explored for a 3D printed octet-truss geometry. Using this information, new mathematical/computational/experimental models could be designed which provide end-to-end validation. However, this was outside the context of this thesis as it would require new multiscale hyperelastic material models, as mentioned in Section 6.2.5. The newly implemented material models in FEBio allows for new finite element simulations that could represent soft cellular tissues, for example to see the effect of body forces on an apple's geometry, or as part of hybrid approach where discrete cells are modelled in high stress areas and continuum material where debonding does not occur, as discussed in Section 6.2.3.

6.2 Further work

6.2.1 Cell size effect

Not discussed in the body of this thesis is the impact of cell size. Cell size is explored in a collaboration project (included in Appendix B) where we test several silicone structures in homogeneous deformation, with the same beam thickness-to-length ratio. This study highlights that smaller, but more numerous cells of hyperelastic material will increase sample stiffness. However, within the multiscale framework, each of these structures would give the same elastic properties. Often in multiscale frameworks the cell size is assumed to be much smaller than the sample size, yet here we do not enforce this constraint and there may be some way to include the effects of cell size.

6.2.2 Stochastic material parameters

Accounting for the inherent variability in material properties is one of the next stages in research for hyperelastic materials [115]. This could be the result of variation between samples, within individual samples, and from experimental error/uncertainty. In this case, the standard deterministic model parameters and equilibria are replaced by stochastic parameters and 'likely equilibria', defined in terms of probability distributions. Several papers, where stochastic elasticity problems are treated analytically, have been recently published [105–107,116,117], which contain new and useful findings, and answer important questions such as 'what is the influence of the random model parameters on the predicted nonlinear elastic responses?' and 'what are the possible equilibrium states and how does their stability depend on the material constitutive law?'. These problems, can offer significant insight into how the stochastic formulation can be incorporated into the nonlinear field theory. Similar stochastic models can be developed for other mechanical systems.

6.2.3 Hybrid models and generative modelling

Cell-cell dissociation, or debonding, along specific zones is a fundamental process in the growth, reproduction and ageing of plants. Seed pods and pollen anthers open along specific contours (dehiscence) [94, 95, 133], whereas leaves and fruits are shed from prescribed connection points (abscission) [139,140,146]. Dehiscence and abscission occur through zones which are only a few cells thick. As with fruit, the cell-cell bonds degrade, but in addition, here, the cells outside of this zone lignify and become stiffer. Mechanical stimulation is often necessary to initiate the disassociation between the cells, which may come from harvesting machinery, human touch or environmental conditions such as wind. In some cases, the disassociation is violent as it releases residual stresses in the material, such as in 'pod shatter' where the seeds get widely scattered [151]. We may want to delay, disable or promote the onset of this process of debonding. By better understanding the fundamental processes, from a mechanical perspective, we can better direct agricultural research efforts for increasing productivity and reduce waste.

So far, we have constructed finite element models for the plant tissue as an assembly of discrete closed cells with intercellular cohesion, and as a representative continuum material (developed in [118, 119]). Now we can combine these approaches to show a more efficient hybrid method that can be used to describe tissues with different debonding areas, such as in dehiscence and abscission. In areas where debonding does not occur, a multiscale hyperelastic material model can be used. This can have different properties to the debonding area, such as increased wall stiffness and cellular pressure. In the areas where debonding can occur, discrete cells can be modelled with hexagonal cell walls containing a soft elastic inclusion and bounded together by an intercellular pressure, as previously studied. The successive deformation decomposition procedure can also be implemented here.

Hybrid example

The cell walls and cell core are made from a neo-Hookean material described by the strain-energy function

$$\mathcal{W}(I_1, I_2, I_3) = \frac{\mu}{2}\left(I_1 - 3 - \ln I_3\right) + \frac{\lambda}{2}\left(\ln I_3^{1/2}\right)^2, \tag{6.2.1}$$

with $\mu_w, \lambda_w, \mu_c, \lambda_c$ representing the cell walls and the core, where the parameters for the cell core are at least one order of magnitude smaller than the cell wall.

The continuum material, built from the above material model, has the strain energy density function

$$\begin{aligned}\mathcal{W}^{(o)}(i_1, i_2, i_3) = {} & \frac{\mu_w \rho_w^{(o)}}{2}\left[(1+k)^2\left(i_1^2 - 2i_2\right) - 2k(1+k)i_1 - 3\left(1-k^2\right)\right] \\ & - \mu_w \rho_w^{(o)} \ln\left[(1+k)^3 i_3 - k(1+k)^2 i_2 + k^2(1+k)i_1 - k^3\right] \\ & + \frac{\lambda_w \rho_w^{(o)}}{2}\left\{\ln\left[(1+k)^3 i_3 - k(1+k)^2 i_2 + k^2(1+k)i_1 - k^3\right]\right\}^2,\end{aligned} \tag{6.2.2}$$

which has been implemented in FEBio [92] as a new material model, as discussed in Section 5.5.1.

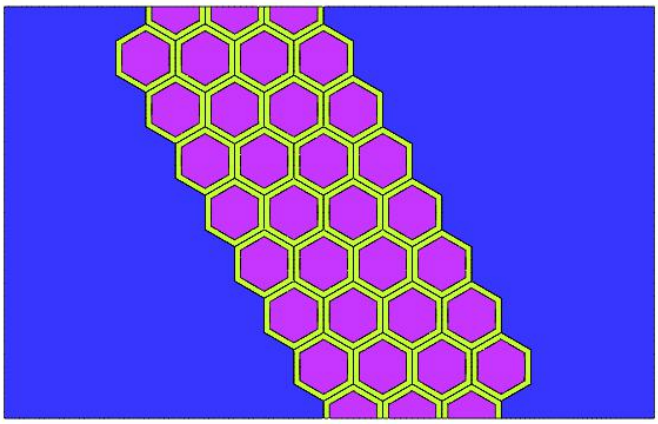

Figure 6.1: Geometry of a hybrid model of cohesive cells in unilateral contact. Blue indicates areas where the continuum material (6.2.2) is used. Yellow and pink indicates cell walls and cell cores, respectively, where neo-Hookean material (6.2.1) is used, with the cell core much softer than the cell walls.

In the example FEBio simulation, Figure 6.1, structures are subject to shear deformation through the following Dirichlet boundary conditions:

- $\mathbf{u}_X = 1$ displacements, with $\mathbf{u}_X^+ = 1$ on the top face and $\mathbf{u}_X^- = -1$ on the bottom face;
- $\mathbf{u}_Y = 0$ on both top and bottom faces and additionally on all non-boundary cell faces;
- $\mathbf{u}_Z = 0$ displacement on all external faces.

$\mathbf{u}_i$, $i = X, Y, Z$, indicates displacement in the i^{th} direction, of unitless dimension, relative to the length of one cell face.

Cell pressure and cohesion are applied by the following Neumann boundary conditions:

- $\mathbf{g_n} = 0.005$ MPa, normal traction on the contact interfaces;
- $\mathbf{g_t} = 0$, tangential traction zero everywhere.

The direction of $\mathbf{g_n}$ is normal relative to the current state of the surface, such that if the angle of the surfaces changes, so does the direction of force.

We can vary the cell wall stiffness parameter μ_w inside the debonding zone and in the continuum material. Stiffening in the continuum material (or softening within the debonding zone) is indicative of the differential stiffness between lignified areas and non-lignified cells in the debonding zone.

With these tools we can create complex, but efficient numerical simulations and hope the approach and resulting mechanical insights are used in experimental investigation of phenomenological processes such as: coordinating the falling of fruits at harvest; suppressing behaviours such as pod shatter in oilseed rape and the premature shedding of petals in ornamental flowers; and promoting cell-cell separation for 'easy-peel' fruit.

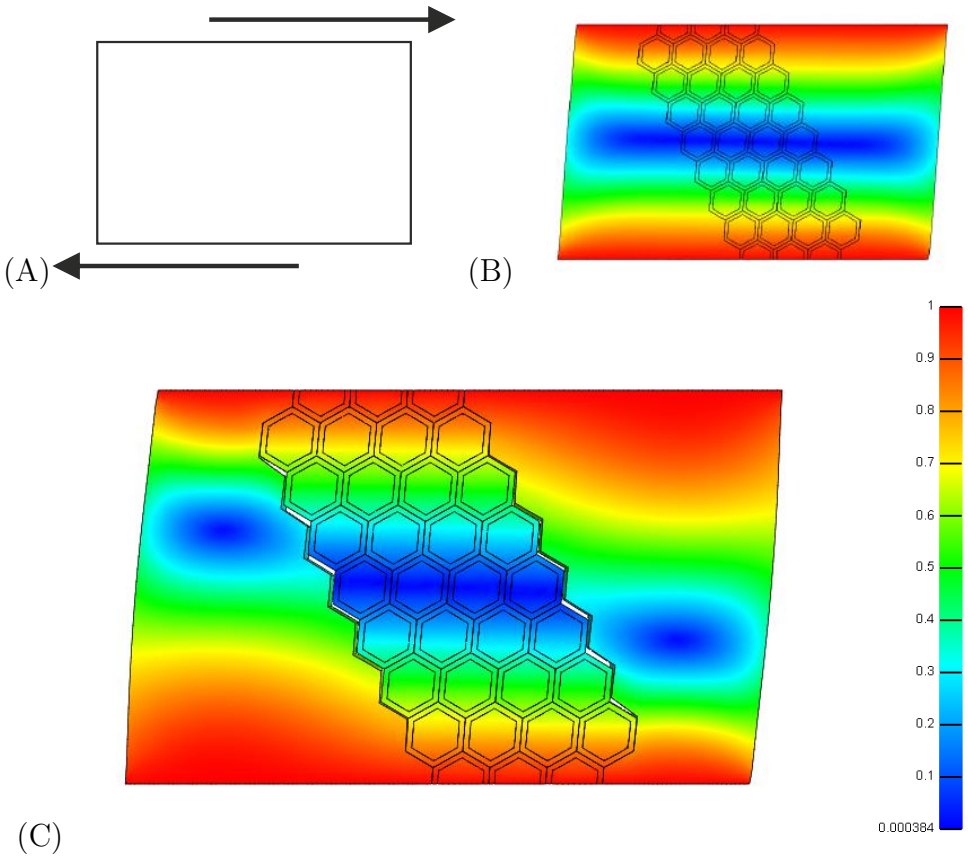

Figure 6.2: FEBio output of the SDDP applied to a hybrid model of cohesive cells in unilateral contact, surrounded by mesoscopic continuum material, under shear deformation: (A) schematic of the direction of shear deformation applied; (B) deformed configuration after the first SDDP analysis step; (C) deformed configuration after the second step SDDP analysis step where cells can debond. Colour scale indicates total (absolute) displacement in the X direction.

Generative modelling

These hybrid models can be incorporated in an adaptive multiscale approach for the analysis of cellular bodies that can handle a large numbers of cells. In a multiscale process, a continuum hyperelastic model can be used first to describe the structure at the macroscopic level, then, after the loading is increased, the areas where the contact forces reach critical values can be remodelled at the microscopic level to predict important local effects. The open source MatLab interface for FEBio, Gibbon [120] is a strong candidate for this iterative remodelling process.

6.2.4 Hierarchical structures

Advancements in manufacturing techniques are also enabling the creation of new types of materials with several nested hierarchical levels [4, 44, 172, 173]. Such structures promise to explore uncharted territory in materials research [54,65,160], while the recursive nature of their hierarchies brings up questions about self-similar and fractal behaviours [1, 4, 48, 87, 134].

As the strain-energy functions for the isotropic hyperelastic cell wall and cell core materials can be chosen arbitrarily, the mesoscopic models for open- or closed-cell structures given by (5.2.19) and (5.2.21), respectively, can be applied iteratively to create hierarchical or self-similar structures. In this case, the cell walls would consist of stretch-dominated architectures with open or closed cells. For a model to be classified as self-similar, the geometric and kinematic assumptions must hold on multiple levels. These models can be useful in deformation decomposition or multiple scale procedures, where a cellular structure is represented first as a continuum material deforming under finite homogeneous strain. The design of such models and their non-linear elastic analysis remains to be explored. newpage

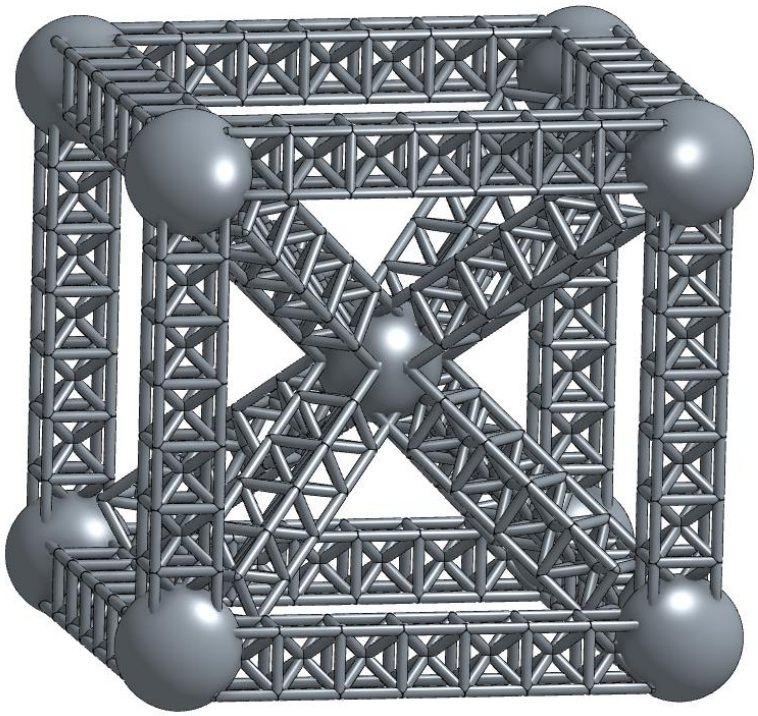

Figure 6.3: An example self-similar body-centred-cubic geometry.

6.2.5 Optimised 3D printed structures

The behaviour of generalised shear motion from Section 3.3 could be integrated into the mesoscopic model of Section 5 to give the time-dependent response of 3D printed structures in sandwich panels, such as the octet-truss Figure 6.4A or the hierarchical geometries developed by the author Figure 6.4B&C with a bending dominated structure embedded within a stretch-dominated architecture. The material stiffness is quantified by a multiscale relationship between the microscopic properties such as beam width. The relationship between oscillation frequency and applied load could lead to dampening or excitement under specific loads - which has applications in automotive and aerospace industries where manipulating vibrations can increase product lifespans as it can mitigate fatigue. This idea was awarded first place in the Cardiff Sparks competition in the 'Ideas' category, which funded a batch of 3D printed prototypes.

(A)

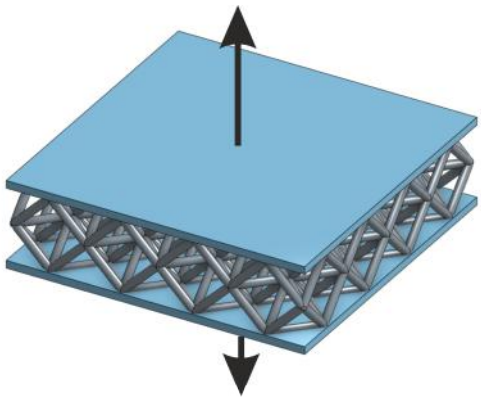

(B)

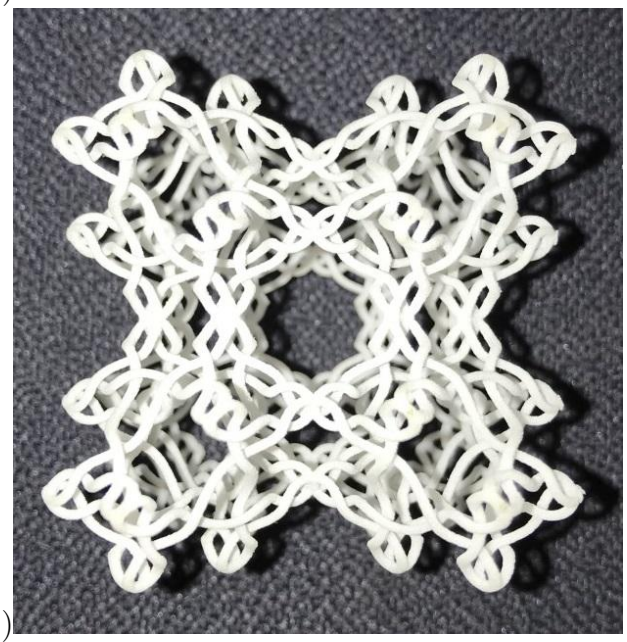

(C)

Figure 6.4: (A) An octet-truss geometry in a sandwich structure; and a hierarchical geometry designed by the author in an (B) octet geometry and (C) a hexagonal sandwich geometry.

Appendices

Appendix A

Insight into testing an ordered, open-cell geometry

We take this opportunity to explore the gap between the analytical theory presented in Section 5 and practical experiment. This task is non-trivial as both mathematical assumptions and experiments can have conflicting limitations.

The octet-truss geometry is chosen here as it is an ordered, isotropic lattice material with microscopic parameters that can be varied (such as beam thickness) to change the structure's elastic properties. The structure is highly efficient and is one of the most lightweight to stiff geometries available. It has been a geometry of interest in numerous studies [44,54,65,134,160,172,173] where it has been studied, (or 3D printed) with linear material. No literature was found for this structure using hyperelastic material.

Homogeneity

We assume in the mesoscopic framework that the material is deformed by a homogeneous **deformation**, such that the same deformation applies to each part of the material, regardless of position. As we produce a continuum material model, we assume that the cellular structure can be considered a homogeneous **material**.

The boundary conditions applied in an engineering tensile test often do not

allow homogeneous deformation. For example, a tensile test uses clamps to grip the test piece and these restrict lateral contraction, creating necking in the test material. Often the assumption is made that if the test piece is sufficiently long, then the middle section deforms homogeneously. Innovative test piece clamps have been designed for quasi-2D materials (2D designs with a thickness), discussed in Appendix B, which allow for homogeneous uniaxial tensile deformation.

The material can only be considered homogeneous if there are a sufficiently large number of cells and the boundary cells behave the same as the central cells. Unfortunately this is not the case with the octet-truss geometry as the behaviour of the boundary cells (which deform differently to the central cells) will dominate if they are not sufficiently far from the centroid of the sample. This means that the engineering test solutions above are inappropriate as a thin sample will be subject to the effects of boundary cells.

Stretch-dominated behaviour

The 'incomplete' cells on the boundaries are softer than the core material as the conditions for being stretch-dominated are not met here. The beams are organised into diamonds, as shown in Figure A.1 and bending occurs at the joints. The addition of cross bracing on the boundary can preserve stretch-dominated behaviour. If the bracing is orientated perpendicular to the direction of force, this will enforce stretching in the boundary beams, without adding surplus stiffness (as the beam will only resist cell contraction and not go into tension itself).

Also, the conditions for stretch-dominated behaviour are defined in the infinitesimal strain regime and do not necessarily hold true for large deformation. Shearing and buckling can be observed in very soft materials, or large deformation.

In our models we assume random orientation of beams and that on average, each beam undergoes the same deformation. The octet-truss has beams with a prescribed order and geometry and it is noted that 2/3 beams go into tension

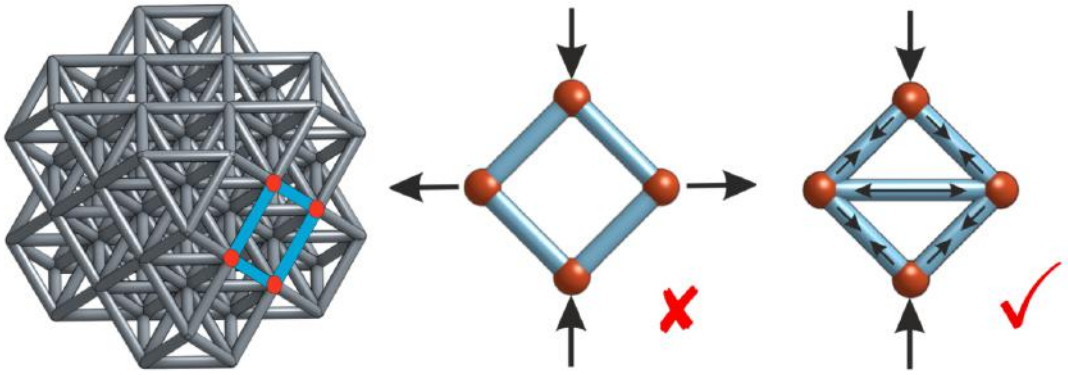

Figure A.1: The surface of octet-truss cells which show boundaries are not stretch-dominated.

and 1/3 go into slight compression (as expected in stretch-dominated structures). This can be seen in Figure A.2 where beams orthogonal to the stretch are blue (no stress) and all other beams are identically stressed (red). This model was created using Gibbon [120], an open source MatLab interface for FEBio.

Beam length, orientation and nodal connectivity

The walls are taken to be thin, with the thickness-to-length ratio $0 < k = t/L < 1$. As k increases, so does the joint volume which results in the assumption breaking down that the joint does not significantly contribute to the strain energy of the structure. There are limitations in the 3D printing process for beam length, thickness and cell size, due to unsupported overhangs. Using the printing technology in the Cardiff University Engineering department, the lowest k value achievable is $k = 0.333$, where the cell walls are cylinders with diameter 2mm, length 6mm and unit cell size 11.3mm. $k = 0.333$ is the upper limit of beam thickness ratio before the joints show too much deformation.

We also assume that:

- all cell walls have equal thickness and length (however here there are two different beam lengths. We could take the average beam length);
- the cell walls meet at joints with thickness t (which is roughly true here);

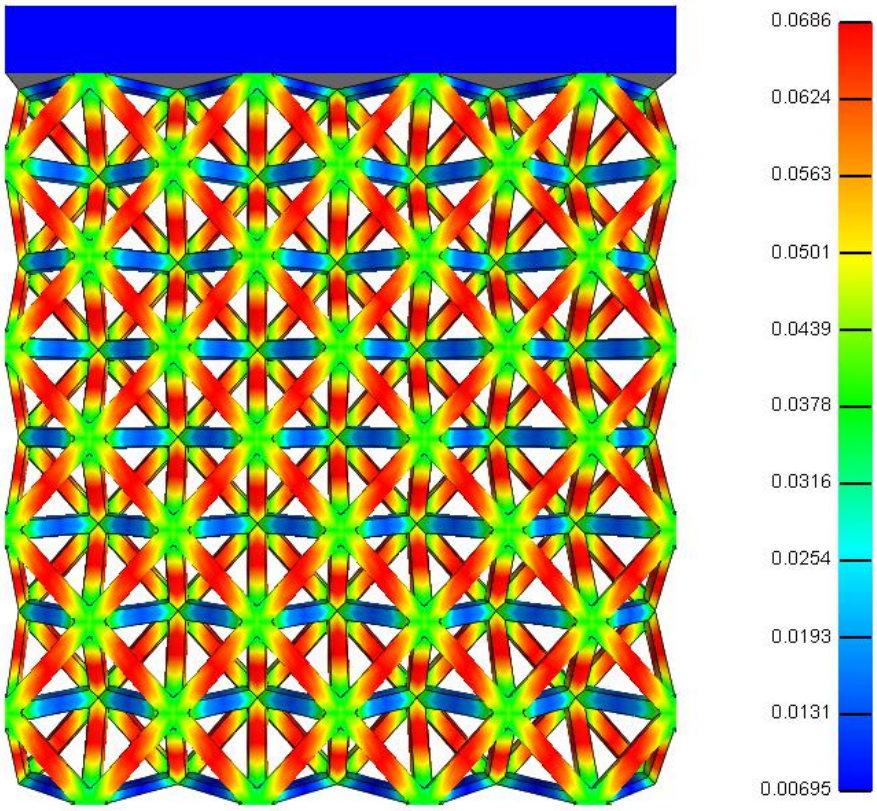

Figure A.2: Slice plot of an octet-truss geometry under small axial tension, where the colour bar represents effective stress in MPa.

Figure A.3: Octet-truss geometry printed at Cardiff University using ninjaflex.

- the number of walls connecting at a joint is constant (whereas there are 8 and 12 beam connections).

Measurement

In the mathematical models we calculate the stress within the continuum material body, but in a non-homogeneous material it is not clear how this internal stress translates. In experiment, there is often a normal stress applied to the boundary which is recorded as nominal (or engineering) stress. Due to the deformation gradient $\mathbf{F}$ being assumed to be strictly diagonal, the nominal stress is related to the first component of the 1^{st} Piola Kirchhoff stress tensor. From the stress on the boundary we can calculate the expected deformation in the mesoscopic material model. One can also measure the displacement in individual beams on the boundary, using optical methods such as DIC (digital image correlation) and video strain gauge, but as we know already, these beams act differently than those within the body.

Material properties

Often 3D printing material is not classified by a hyperelastic material model (with material constants) by the manufacturers so it is the researchers duty to perform this task. For the polymer 'ninjaflex' used at Cardiff University, Mr. Michael Robinson performed uniaxial tension (UT), biaxial tension (BT) and pure shear (PS) tests to classify the material (sufficient data for accurate hyperelastic model fitting), under a static setting. As the material is incompressible, then [37, 152] can be used to inform the fitting procedure and appropriate model selection for a rubber-liker material. The author aided in classifying ninjaflex, finding that Mooney-Rivlin or Yeoh-Fleming models [167] appropriately fit the data. As mentioned in Section 6.2.2, variability will exist within the material model as properties could vary between prints and could also vary with temperature.

Viscoelasticity and damage

We assume that the material consists of a true hyperelastic material which does not have strain rate dependant properties and does not undergo microscopic or macroscopic damage. However in practice, all materials undergo some microscopic damage/viscoelasticity and show hysteresis. Damage usually starts at the weakest point in a cellular structure and propagates from there [66]. The test print quality (Figure A.3) is an acceptable standard for mechanical testing, with bonding between layers and a roughly smooth step size between layers. However, many imperfections can be observed which could promote localised stresses and slip between layers after repeated or high intensity loading.

Summary

There is substantial evidence to support that this geometry cannot be tested in homogeneous conditions and that any attempt would be a qualitative approximation. There are different methods that could be approached, including using a sample geometry which is very wide perpendicular to the loading direction, and within a sandwich panel. Here the boundary conditions can be approximated with $\mathbf{F} = \text{diag}(\alpha, 1, 1)$ and simulated with periodic boundary conditions. However, the mathematics may be better optimised for this situation using simple shear assumptions rather than uniaxial tension on the microscopic scale.

Appendix B

Non-linear scaling effects in the stiffness of soft cellular structures

For cellular structures with uniform geometry, cell size and distribution, made from a neo-Hookean material, we demonstrate experimentally that large stretching causes non-linear scaling effects governed by the microstructural architecture and the large strains at the cell level, which are not predicted by the linear elastic theory. For this purpose, three honeycomb-like structures with uniform square cells in stacked distribution were designed, where the number of cells varied while the material volume and the ratio between the thickness and the length of the cell walls was fixed. These structures were manufactured from silicone rubber and tested under large uniaxial tension in a bespoke test fixture. Optical strain measurements were used to assess the deformation by capturing both the global displacements of the structure and the local deformations in the form of a strain map. The experimental results showed that, under sufficiently large strains, there was an increase in the stiffness of the structure when the same volume of material was arranged as many small cells compared to when it was organised as fewer larger cells. Finite element simulations confirmed our experimental findings. This study sheds a new light on the non-linear elastic responses of cellular structures in large-strain deformations, which cannot be captured with linear elasticity.

B.1 Introduction

The design and assessment of cellular structures undergoing large elastic deformations is central in many industrial and biomedical applications, and their mathematical modelling and mechanical analysis pose many theoretical and computational challenges [103, 104, 113, 118, 119]. In particular, soft cellular structures are the subject of important research efforts in regenerative applications, such as soft tissue scaffolds, for which a better understanding of the mechanical behaviour is necessary to optimise their functional performance [16, 39, 45, 47, 83, 148, 163, 171]. Cellular structures can also be found in both load-carrying and non-load-carrying matter, in nature as well as in several industrial areas (e.g., impact protection, aerospace, microelectronics, pharmaceutical and food processes) [56, 66, 122, 136, 161]. Therefore, by studying the fundamental mechanical responses of cellular structures, important insights can be gained for the development of many areas of research.

For natural and man-made cellular structures, several key factors determine the magnitude of the enhancement of stress level in the cellular body, including the cell geometry, the cell wall thickness, and the number of cells [103, 104, 118, 119, 144]. For two different structures made from the same volume of solid material, which is distributed uniformly as a small number of large cells or as a larger number of smaller cells, respectively, if the ratio between the thickness and the length of the cell walls is the same in both structures, then the stiffness of the structures under small strain elastic deformations is the same [66]. While this is valid for many cellular structures with linear elastic cell walls, and similarly, for structures with non-linear elastic walls in the small strain regime, in many cellular solids, the cell size is expected to have a more independent effect on the elastic responses, even though this effect is typically obscured by other structural properties [9, 145].

In this study, for cellular structures with uniform geometry, cell size and distribution, and a neo-Hookean hyperelastic cell wall material [138, 156], we demon-

strate experimentally that sufficiently large stretching causes non-linear elastic effects which are governed by the microstructural architecture and the large strains at the cell level, and are not predicted by the linear elasticity theory. For this purpose, three honeycomb-like structures with uniform square cells in stacked distribution were designed, where the number of cells varies while the total material volume and the ratio between the thickness and the length of the cell walls is fixed. These structures were manufactured from silicone rubber and tested under large uniaxial tension in a bespoke test fixture. Optical strain measurement techniques were used to assess the deformation by capturing both the global displacements of the structure and the local deformations in the form of a strain map [50, 60, 154, 165, 170]. The experimental results show that there is an increase in the stiffness of the structure when the same volume of solid material is arranged as many small cells than when organised as fewer larger cells. This behaviour is also captured by our finite element simulations of cellular structures with similar geometries and cell wall material properties.

This study sheds a new light on the non-linear elastic responses [67, 73, 88, 113, 124, 127, 157] of soft cellular structures, which cannot be captured by the classical linear-elastic theory. In particular, we show that, under sufficiently large strains, the stiffness of the structures with non-linear elastic cell walls varies with the cell size [104, 118], in contrast to the results predicted for structures with linear elastic cell walls [66], given that the same volume of material is used for each structure, and that the thickness-to-length ratio for the cell walls remains the same. This has important implications for the optimal design of cellular materials in various applications, and in particular, for stretch-dominated architectures, which are structurally more efficient, due to a higher stiffness-to-weight ratio, than the bending-dominated ones [30, 66, 113, 118, 119, 144].

B.2 Experimental material and methods

B.2.1 Structure design and manufacture

Three periodic honeycomb-like structures with a different number of square cells in stacked distribution were designed and manufactured, ensuring that the overall volume of solid material used and the ratio between the thickness and the length of the cell walls is the same for all structures, whilst the number of cells vary. The geometric parameters for the designed structures are summarised in Table B.1 and illustrated on a single structure in Figure B.1. In this figure, the tabs seen at the top and the bottom of the structure allow for the physical structure to be mounted in the bespoke test fixture, as described in detail in the next section which focuses on the experimental set-up.

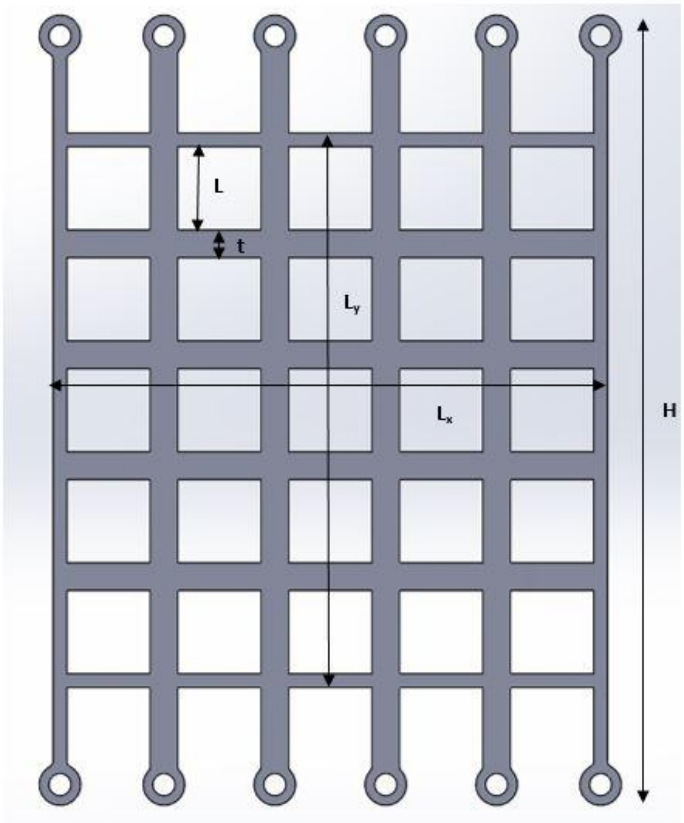

Figure B.1: Geometry of cellular structure with 5×5 cells.

Individual aluminium moulds were created for each of the structures, and the

cellular structure	overall height, H (mm)	structure height, L_X (mm)	structure width, L_Y (mm)	structure depth, L_Z (mm)	cell wall length, L (mm)	cell wall thickness, t (mm)	cell wall thickness-to-length ratio, t/L
3×3 cells	170.833	100	100	10	25.00	8.33	3.00
5×5 cells	142.50	100	100	10	15.00	5.00	3.00
9×9 cells	127.67	100	100	10	8.33	2.78	3.00

Table B.1: Geometric parameters of the undeformed cellular structures tested experimentally.

structures were then cast out of Tech-Sil 25 silicone. This silicone is a two-part silicone, mixed as per the manufacturer's instructions, which underwent a two-part de-gassing process, first after the initial mixing and second after the casting, then allowed 24 hours to cure. The material behaviour of this silicone is characterised by a neo-Hookean hyperelastic model, described by equation (B.2.1), with Young's modulus E= 0.74 MPa and Poisson's ratio ν=0.48 under infinitesimal deformations. The neo-Hookean model is the simplest non-linear hyperelastic model, originally proposed to characterise the non-linear elastic behaviour of rubberlike material in [138, 156]. Our parameter values were obtained through uniaxial tensile and compression testing, using the process of inverse analysis, prior to the manufacturing of the structures. A total of six structures were manufactured, two of each structure type.

B.2.2 Experimental setup

To conduct the uniaxial tensile testing of each structure, a bespoke fixture was designed (see Figure B.2). This allowed for the (top and bottom) ends of the structure to slide horizontally whilst the structure was loaded vertically, meaning that all the initially straight and vertical cell walls remained almost straight and vertical throughout the testing, avoiding the unwanted bending of the side walls, which is commonly seen during more traditional tensile tests whereby the ends

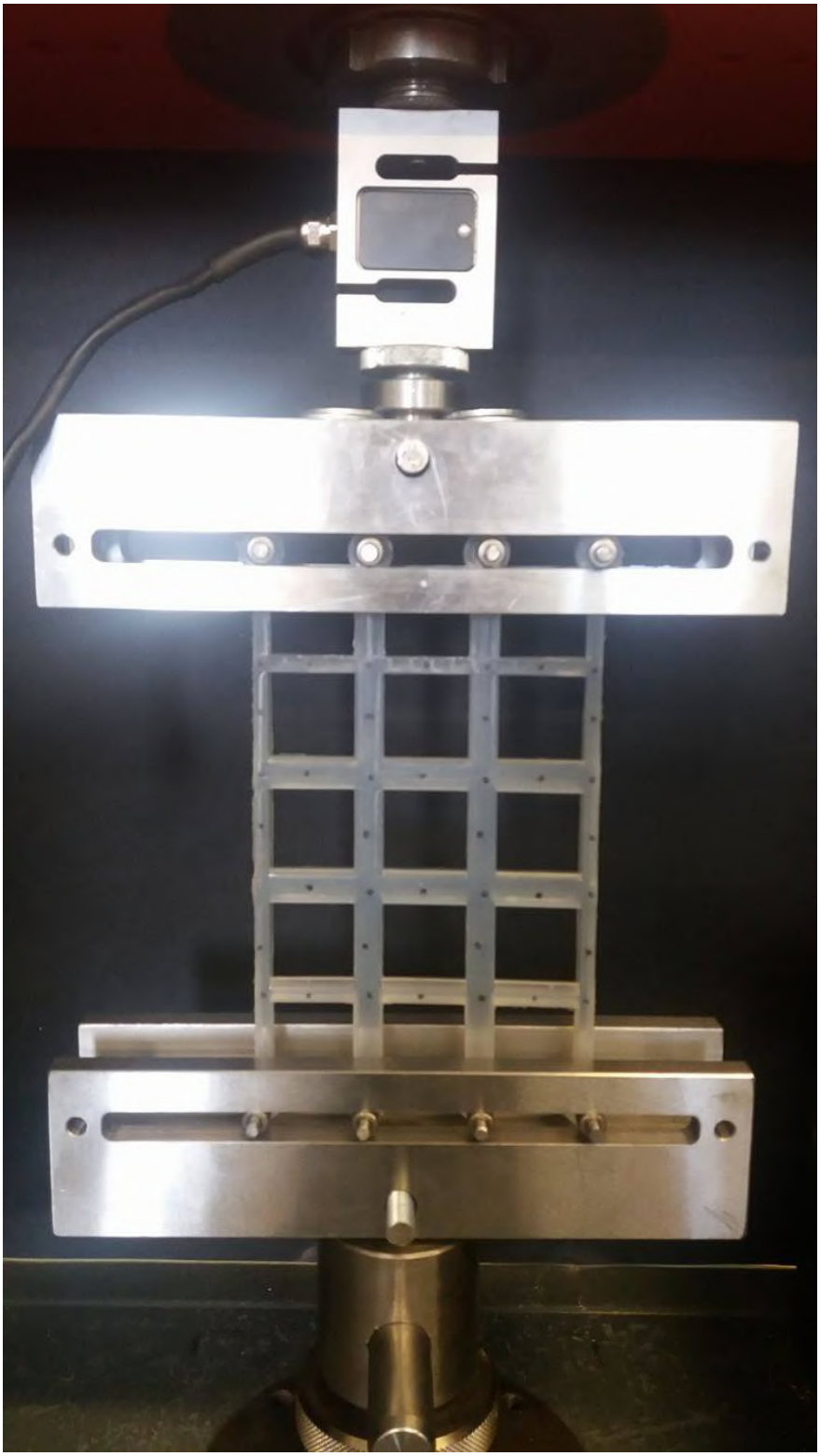

Figure B.2: Bespoke test fixture allowing the structure to slide in the horizontal direction and create a straight edge during tension.

of a structure are clamped. This was achieved through the use of dowel rods and needle roller bearings, where the friction within the system was minimised through polishing of the contact surfaces. When the coefficient of friction was experimentally measured for the system, a resulting mean CoF of 0.02 ± 0.003 was found, demonstrating minimal friction within the bespoke test fixture.

Uniaxial tensile tests were conducted using a Zwick - Roell Z050 tensile testing machine, with a 2kN load cell to measure tensile force. Initially, loading and unloading tests were carried out to verify that the structures were elastically deformed, i.e., all the changes in the deformed structures were reversible. For this, each structure was subjected to a 60N tensile load in 10N increments and unloaded to 0N after each increment. To measure their local and global deformations, the structures were subjected to a maximum tensile load of 50N. To capture quasi-static deformations, the tests were performed at a velocity of 2 mm/s, and a pre-load of 1N was used to remove slack from the experimental set-up. Tests were conducted twice for each structure type (n=2).

B.2.3 Digital Image Correlation

Digital image correlation (DIC) is a non-contact optical measurement technique measuring specimen displacement. A high contrast pattern is applied to the surface of the specimen, which provides unique points of identification to allow the software to track the displacement of the specimen. The specimen is imaged in its unloaded state, and this acts as a point of reference for the software. The specimen is then imaged throughout loading, either through video or through a series of camera images. The software will then use the captured images to track the unique points within the high contrast pattern, measuring the displacement of the specimen. From the displacement, strain can then be computed using the parameter of the affine transformation and the gradients of the deformation [50,60,154,165,170]. Within this study, two DIC systems were used, the first was the Imetrum Video

Gauge system. This was used to capture the global deformation of the structure through the application of virtual strain gauges. The second system was a Q-400 Dantec Dynamic system used to create a 2D map of the strains at a local level, focusing solely on the centre cell of each structure.

Measuring global deformation

A video strain gauge system (Imetrum) was used to capture the global deformation of the structure during tensile tests. The system was used with a single camera with a general-purpose lens and calibrated using markers of a known distance apart within the field of view, as per the manufacturer's instructions. Markers were applied to the surface of the specimen to allow the software, provided as part of the system, to track the deformation of the structure. These were applied to the structure using a black marker pen, with markers applied to the intersections and the mid-wall of the cells. When processing the data, virtual strain gauges were applied to the structure, using markers that maximised the length of the gauge, thus reducing errors within the system. For the purpose of this study, a limited number of points were selected to validate the new loading fixture, although there is a potential for further exploiting results obtained from these data.

Measuring local deformation

The Q-400 (Dantec Dynamics) system was used to capture the local deformation of the structures and to validate the finite element models (FEMs). The system consisted of the necessary software, Instra4D, a HiLis light source and a data logging system to connect the cameras to the laptop. The HiLis light source is a high intensity LED illumination system which provides cool and homogeneous illumination. Two digital cameras were used with the system and were mounted onto a tripod with the HiLis light source positioned between them. The two cameras were connected to a data logging system, which in turn was connected to

the laptop. Following this, the aperture and focus of both cameras were adjusted, focusing on the high contrast speckle pattern applied to the surface of the silicone specimen [165]. This high contrast speckle pattern was applied using white and black face paint (Snazaroo). Three different camera setups were required, due to the differences in structure geometry, ensuring the most appropriate setup for each structure in terms of the field of view. Each camera set-up differed in terms of their field of view only, with the same equipment including calibration target and camera lenses used for each. Following the setup of the DIC system, it was necessary to conduct a calibration. This determined the position and orientation of each of the cameras with respect to the surface of the specimen and related the pixel size of the object image to the metric scale. In order to calibrate the system, a series of eight calibration images were taken of a calibration target. The calibration target used for this study was a 9×9 grid, 40mm x 40mm (Dantec Dynamics). The target was rotated and tilted for each image to allow the software to determine the required parameters. A calibration residuum of < 0.1 was considered acceptable [165]. Data was processed within the DIC software, Instra4D, with the parameters from data capture and processing displayed in Table B.2. For each structure, two polygons were drawn over the surface of the struts, one covering the vertical strut, and one covering the horizontal strut. In both cases, the joints were excluded from the analysis. For the polygon, mean values of the strain over the surface were exported. Throughout this study, the Green-Lagrange strain is used [73, 113, 127].

B.2.4 Experimental results

Global deformation of structures

To validate the new loading fixture (see Figure B.2), and thus ensure that the boundary conditions achieved are as expected, the global behaviour of each structure was analysed using the Imetrum video strain gauge system. Virtual strain gauges were added to the structure, as shown in Figure B.3(a), with the red dots

experimental technique used	3×3 cells	5×5 cells	9×9 cells
calibration residuum	<0.1	<0.1	<0.1
speckle pattern size	0.45-1.2 mm	0.35-1.2 mm	0.25-0.6 mm
subset	17 pixels	17 pixels	17 pixels
step size	17 pixels	17 pixels	17 pixels
spatial resolution	1.33 mm	1.02 mm	0.697 mm
total number of images	15	15	15
displacement			
displacement noise	0.005 mm	0.015 mm	0.020 mm
strain			
smoothing method	none	none	none
strain noise	20 mstrain	20 mstrain	20 mstrain

Table B.2: Parameters for the DIC data capture and processing.

depicting the marks made on the physical structure. Struts 1, 2 and 3 were compared to verify that the strain was the same for each of these struts, thus ensuring that no end-effects were present in the structure. The results can be seen in Figure B.3(b), where the struts exhibit almost identical mean vertical strains at loads up to around 80N. Throughout the paper, strains are presented as millistrain or mstrain. Struts 2 and 5 were analysed to ensure that the new loading fixture created symmetrical boundary conditions, as seen in Figure B.3(c), where the mean vertical strains for these two struts are almost identical.

In addition to the vertical strain of different struts, the horizontal strain was also analysed. Virtual strain gauges were added to the structure as shown in Figure B.4(a), with the red dots depicting the marks made on the physical structure. Struts 7 and 8 were compared to verify that the strain was the same for each strut, thus ensuring that no end-effects were present within the deformed structure. These results are illustrated in Figure B.4(b), where the struts exhibit almost identical mean horizontal strains at loads up to around 80N. Struts 8 and 9 were analysed to ensure that the loading fixture created symmetrical boundary conditions, as seen in Figure B.4(c), where the mean horizontal strains for these two struts are almost identical.

Although the reported results correspond to the structure with 5×5 cells,

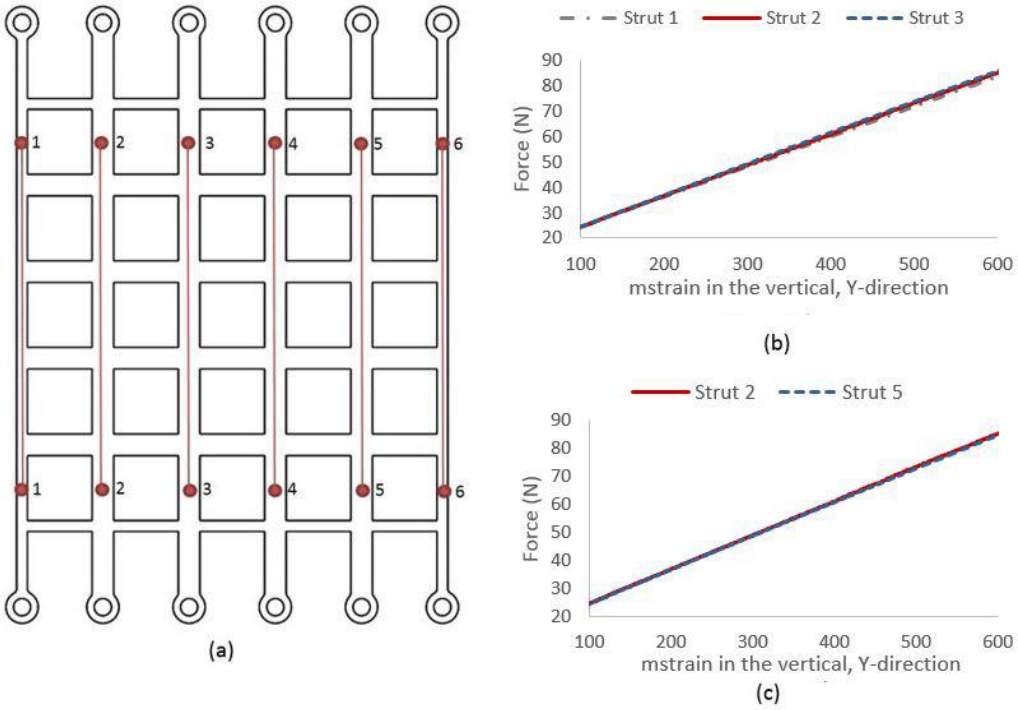

Figure B.3: Comparison of vertical strains in vertical struts: (a) schematic of cellular structure showing the location and numbering of strain gauges for each strut; (b) comparison of mean vertical strains in struts 1, 2 and 3; and (c) comparison of mean vertical strains in struts 2 and 5. The strain shown is in mstrain.

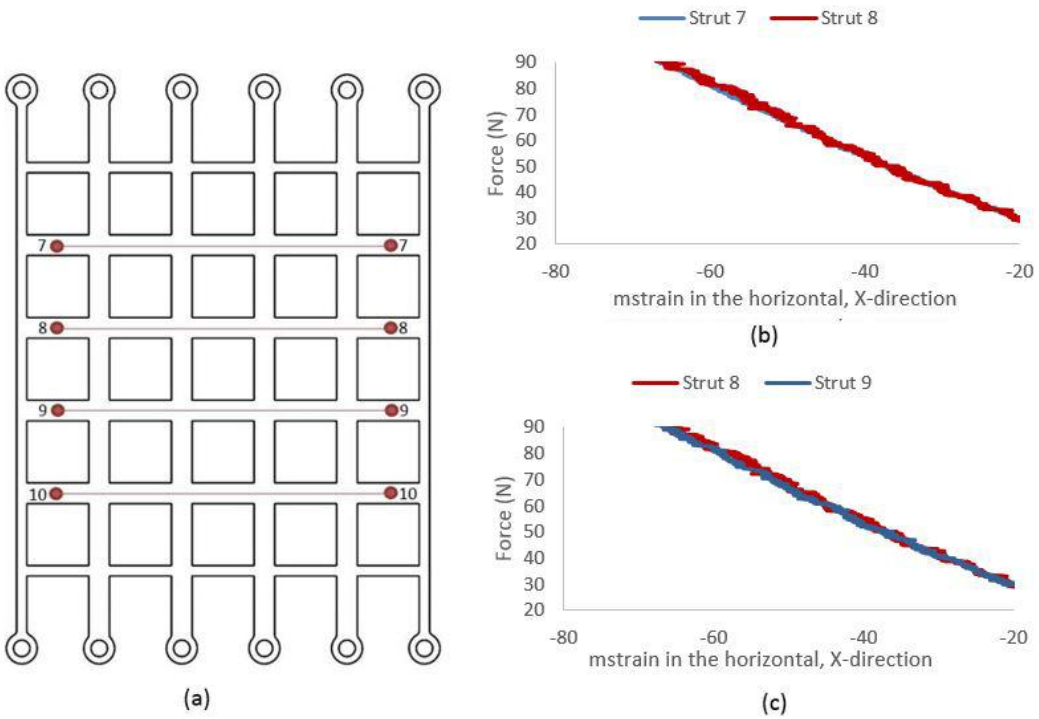

Figure B.4: Comparison of horizontal strains in horizontal struts: (a) schematic of cellular structure showing the location and numbering of strain gauges for each horizontal strut; (b) comparison of mean horizontal strains in struts 7 and 8; and (c) comparison of mean horizontal strains in struts 8 and 9. The strain shown is in mstrain.

similar results were obtained for the structures with 3×3 and 9×9 cells, thus validating the new loading fixture in creating the desired boundary conditions for uniaxial tensile testing under large strains.

To ensure that all testing remained within the elastic limits of the structures and no plastic deformation occurred, a series of loading-unloading tests were also performed. The loading conditions were as described previously, with each structure being subjected to a 60N tensile load in 10N increments and unloaded to 0N after each increment. Figure B.5 shows the results for the three structures. The data demonstrate no plastic deformation of the structure, with each structure clearly remaining within its elastic region, with minimal hysteresis between the loading and unloading paths.

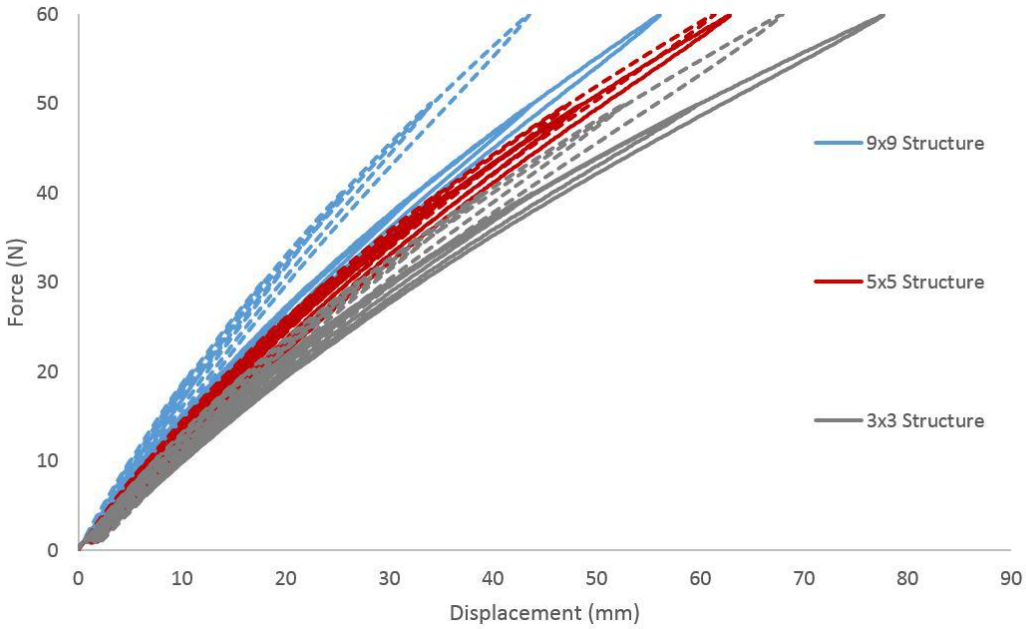

Figure B.5: Applied force vs. maximum vertical displacement in tensile loading and unloading of the three structures. The blue, red and grey lines represent the 9×9 structure, the 5×5 structure and the 3×3 structure respectively, with the dotted and solid lines differentiating between different samples. For experimental testing, n=2.

Additionally, the experimental results demonstrated some variation between different samples of the same structure (see Figure B.5). Despite these variations,

the same trend was seen within the data, with the 9×9 structure being stiffer that the 5×5 structure which was in turn stiffer than the 3×3 structure. The variation between samples could be caused by a number of factors. One possibility is the slight inconsistencies in the manufacturing process. For example, the silicone used is a two-part silicone and small variations in the volume of the mixture could influence its mechanical properties. Another possible explanation for the variation in experimental results is the slight change in the testing environment, for example, tests were not conducted in a temperature-controlled environment.

Local deformation of structures

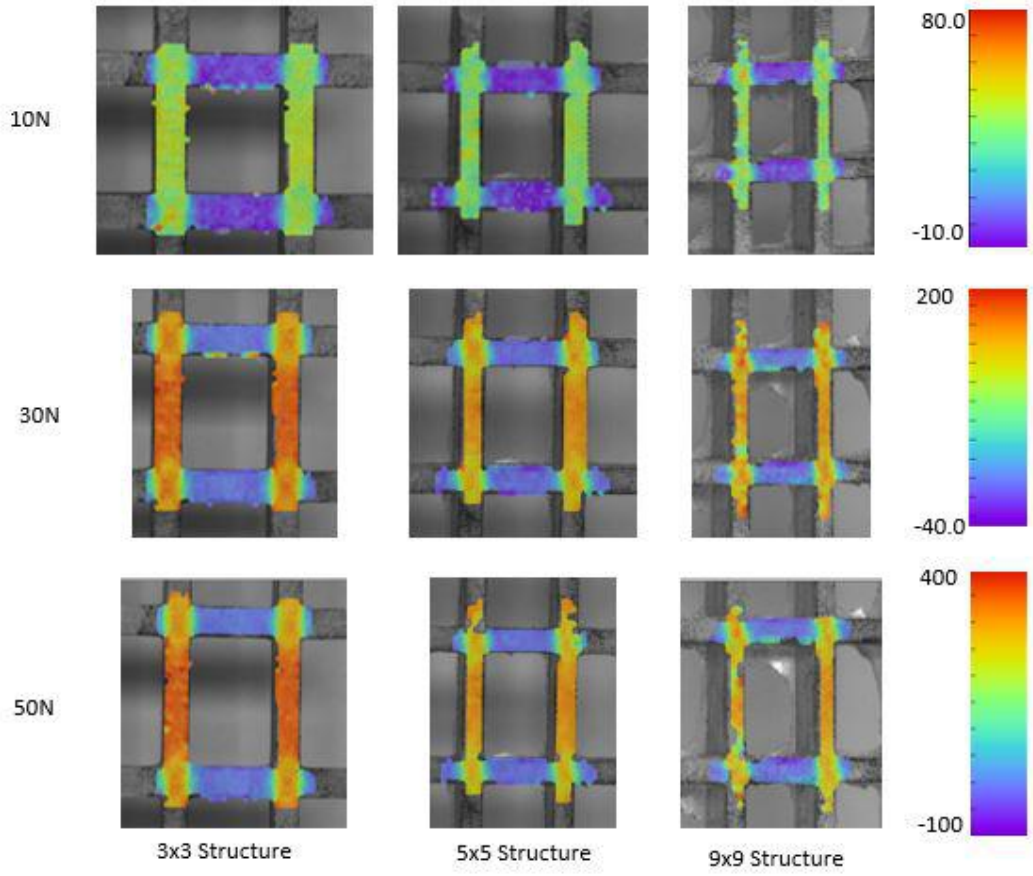

Figure B.6: Colour maps showing the vertical strain in each structure at 10N, 30N and 50N, with the left hand column depicting the 3×3 structure, the middle column depicting the 5×5 structure, and the right hand column depicting the 9×9 structure. The strain shown is in mstrain.

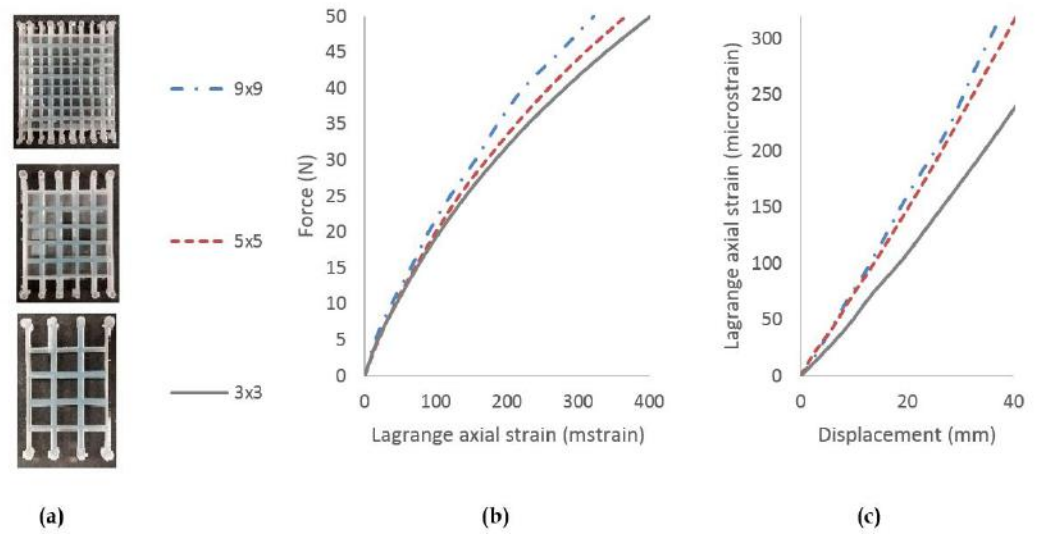

Figure B.7: Comparison of the deformation of the centre cell of the structure tested experimentally using DIC: (a) photos of physical structures; (b) applied tensile force vs. mean vertical strain; (c) mean vertical strain vs. maximum vertical displacement of the load machine. The strain shown is in mstrain.

Since all cells in the structure are deformed similarly, for our analysis, we focus on the central cell. In Figures B.6-B.8, we show the strain maps within the three different structures under three different loads each. The same strain map scale was used for the three structures within each image, but varied for the different loading stages. At 10N tensile load, there appears to be almost no difference between the strains in the three structures, as seen from Figure B.6, but as the load increases, the difference between the strains in these structures increases. For example, Figure B.6 suggests that, in the structure with 9×9 cells, the vertical strain at 50N tensile load is greater than in the 5×5 cells structure, which in turn is greater than in the 3×3 cells structure. This observation is confirmed by the results plotted in Figure B.7, where the force required to stretch the structure with 9×9 cells to a certain magnitude of Lagrange axial strain (or by a certain maximum vertical displacement) is greater than for the structure with 5×5 cells, which in turn, is greater than for the structure with 3×3 cells. Importantly, it should be noted that Figure B.7(b) shows almost no differences in the strains of the cell walls within the small strain regime (typically, this is classified as below 4% strain or

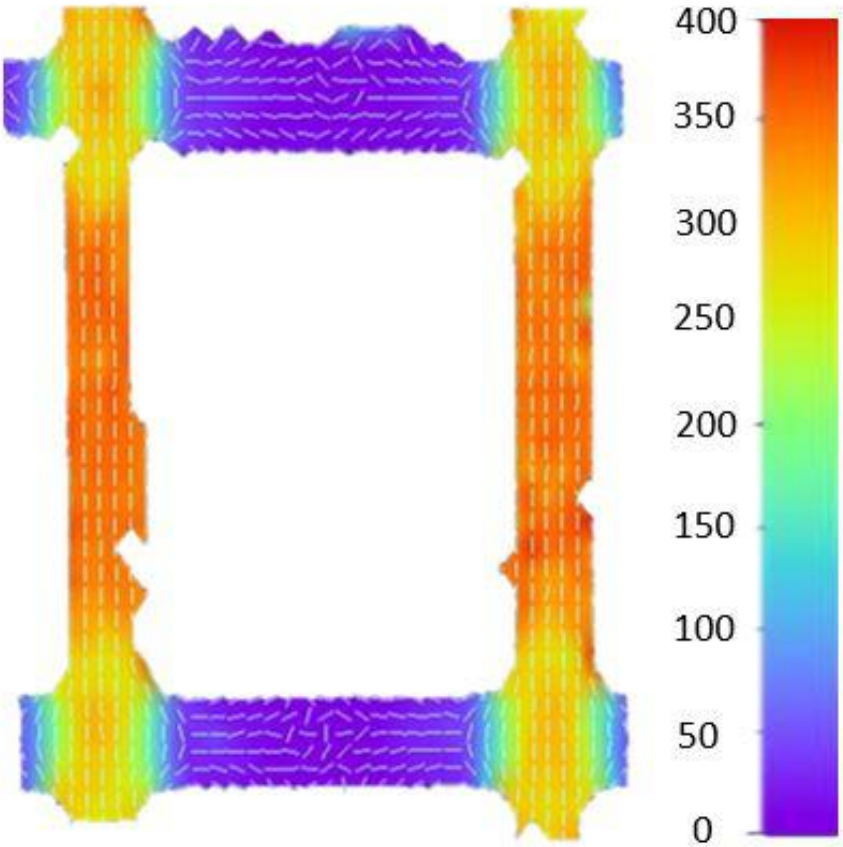

Figure B.8: The maximum principal strain for the structure with 3×3 cells at a 50N tensile load, with the small lines within the strain map showing the local orientation of the strain. The strain shown is in mstrain.

40mstrain). The strain within the cell walls begin to vary at around 150mstrain, showing the stiffening effect of the cell arrangements at larger deformations.

To illustrate the orientation of the maximum principal strains in the structures under tensile loads, in Figure B.8, the strain orientation in the structure with 3×3 cells at a 50N tensile load is shown. However, similar trends were observed in the other structures as well, although with different magnitudes of strain. As seen from Figure B.8, the maximum principal strain is orientated in the vertical direction within the vertical struts, and corresponds to longitudinal tension, whereas in the horizontal walls, the maximum principal strain is orientated in the horizontal direction and corresponds to longitudinal compression. At the intersection between the horizontal and vertical walls, the orientation of the maximum principal strain shows a more curved alignment, highlighting the more complex behaviour that occurs at these joints.

B.2.5 Finite element simulation

Model set-up

In this section, we assess computationally non-linear stretching effects in periodic cellular structures with square cells in stacked distribution and neo-Hookean cell wall material [138, 156], similar to those tested experimentally. Within the finite element simulations, the generalised neo-Hookean model was used, characterised by the strain energy density function:

$$\mathcal{W}(I_1, I_2, I_3) = \frac{\mu}{2}\left(I_1 - 3 - \ln I_3\right) + \frac{\lambda}{2}\left(\ln I_3^{1/2}\right)^2, \tag{B.2.1}$$

where $\mu = E/[2+\nu] > 0$ and $\lambda = \nu E/[(1+\nu)(1-2\nu)] > 0$ are constant material parameters, with E and ν denoting the Young's modulus and Poisson's ratio respectively, and μ representing the shear modulus at infinitesimal deformations, and $\mathbf{C} = \mathbf{F}^T\mathbf{F}$ and $\mathbf{B} = \mathbf{F}\mathbf{F}^T$, with $\mathbf{F}$ denoting the (large-strain) deformation

gradient. The Green-Lagrange strain tensor then takes the form $\mathbf{E} = (\mathbf{C} - \mathbf{I})/2$, where $\mathbf{C}$ is the right Cauchy-Green deformation tensor defined above and $\mathbf{I}$ is the identity tensor (note the boldface notation for tensors) [73, 113, 127].

As in the experimental tests, a Young's modulus, E, of 0.74 MPa and a Poisson's ratio, ν, of 0.48 were assumed for the cell wall material. These parameter values were then used to compute the constants μ and λ for the neo-Hookean model, given by (B.2.1), in the finite element simulations. As a Poisson's ratio of 0.5 corresponds to perfect incompressibility, a Poisson's ratio of 0.48 represents a condition of slight compressibility (or near incompressibility). The modelled structures had the same geometry as those tested experimentally, but the symmetry of the boundary conditions was used to reduce computational cost, modelling only half of the tested specimen. To compute the force-displacement responses in the computational structures, cylindrical metal rods inserted through the hoops at the end of the structure were modelled, mimicking the physical tests conducted experimentally. The position of these rods can be seen clearly in Figure B.9. These rods were modelled as rigid bodies, and the boundary conditions between the rods and the structure, as rigid interfaces. The rigid rods had a prescribed displacement in the positive vertical direction to create the prescribed vertical stretch of the structure. The internal and external faces of the structure were allowed to deform freely. The boundary conditions applied to the model are shown schematically in Figure B.9.

The numerical results recorded here were obtained within the Finite Element for Biomechanics (FEBio) software environment [92]. The model structures were created in SolidWorks and imported into the FEBio software, and a mesh refinement study was performed for each structure, the results of which are shown in Figure B.10, to ensure that the numerical results are independent of the mesh size. To evaluate the mesh sensitivity, the total reaction force was used as this was a criteria of interest in evaluating the overall behaviour of each structure.

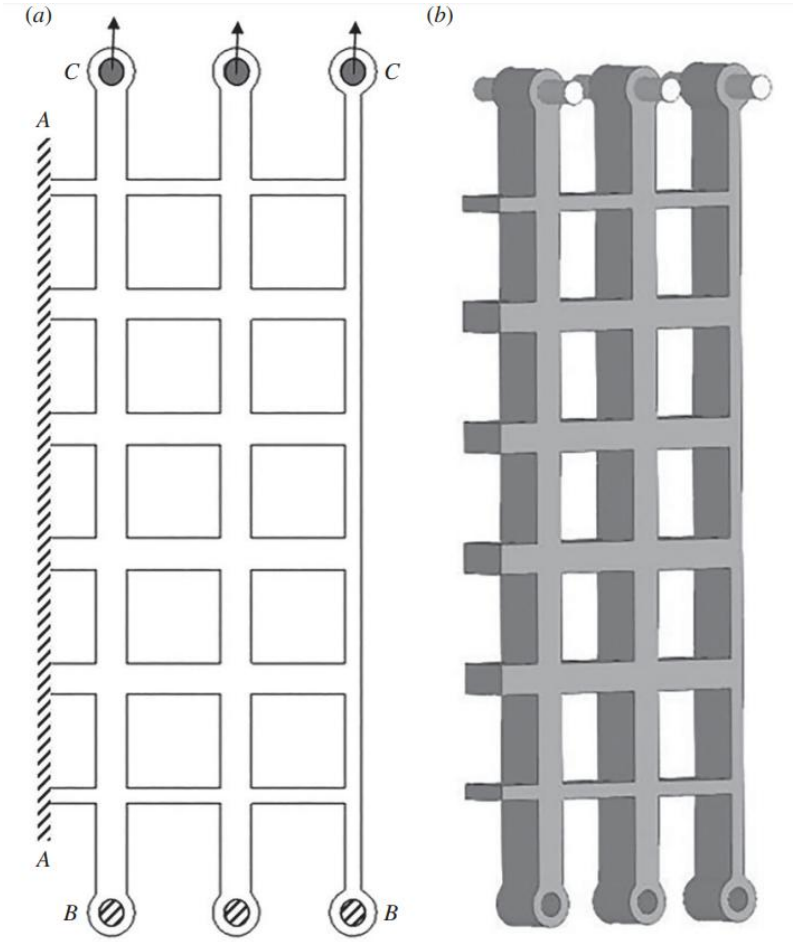

Figure B.9: (a) Schematic view of the finite element boundary conditions, with dash lines along AA showing the surfaces fixed using the symmetry constraint, BB showing the fixed constraint applied in the horizontal and out of plane direction for the inner surface of the holes and CC showing the location of the rigid rods and the direction of stretch. (b) A three-dimensional view of the finite element set-up, clearly displaying the location of the rigid rods.

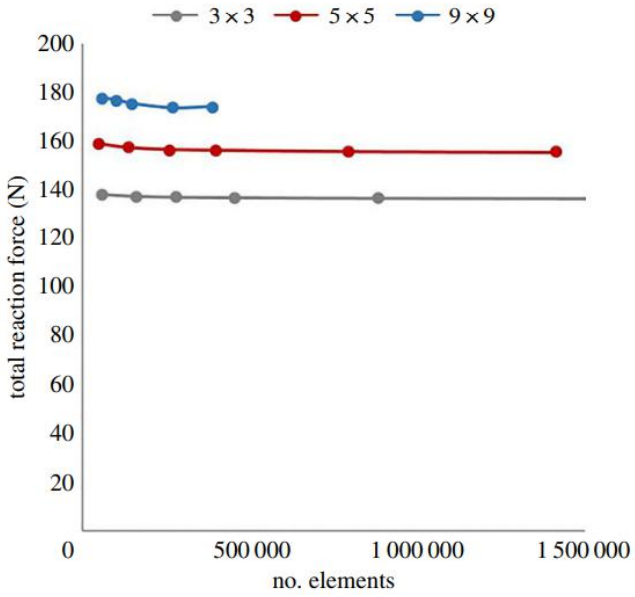

Figure B.10: Mesh sensitivity study for the finite element modelling of the three structures investigated, showing the total reaction force for each structure and the total number of elements in each model.

The reaction force was computed within the FEBio software for each of the rigid rods used in constraining the structures. To calculate the total reaction force for each structure, the computed forces for each rigid rod were added together and the resulting reaction force was doubled due to the symmetry assumption applied to the model. The results were deemed to be independent of meshing parameters once three results in a row were within 1% of one another. The mesh elements used were 4-node linear tetrahedral elements, with the exact details of the mesh used for each structure found in Table B.3. An example of the mesh used for the 5×5 structure can be seen in Figure B.11.

structure	total number of elements	total number of nodes	element type
3×3 cells	449851	98921	four-node linear tetrahedral
5×5 cells	398165	94147	four-node linear tetrahedral
9×9 cells	267391	72971	four-node linear tetrahedral

Table B.3: Final mesh parameters for each structure.

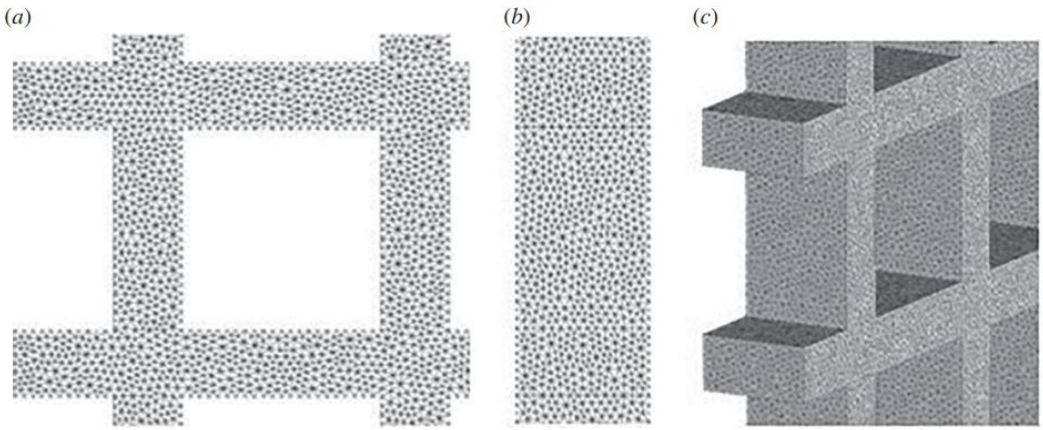

Figure B.11: Example of the mesh for the 5 5 structure with (a) showing the front view of the mesh, (b) showing the side-on view or the elements through the thickness and (c) showing a three-dimensional view of the meshed structure.

Comparison with experimental data

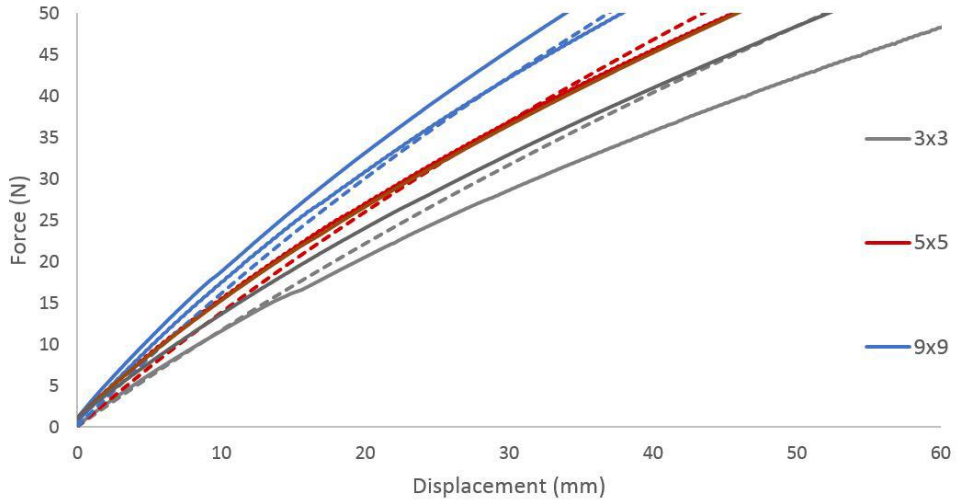

Figure B.12: Comparison of force – displacement curves for the FEBio computational models (dashed lines) and the corresponding experimental data (solid lines) of the three structures. For experimental testing, n=2.

The numerical results from the computational models were compared with the experimental data. For the finite element models, the reaction force on the rigid rods was exported, as well as the displacement of the structure, to compare with the force-displacement data acquired experimentally. The results shown in Figure B.12 for the finite element simulation are in qualitative agreement with the experi-

mental data, as for both the computation and experimental structures, the stiffness clearly increases with the number of cells. In addition to the force-displacement curves, the vertical strain maps across the computational and experimental structures with 5×5 cells are presented, at the same scale, in Figure B.13. In this figure, the magnitude of the strains found computationally and experimentally are similar.

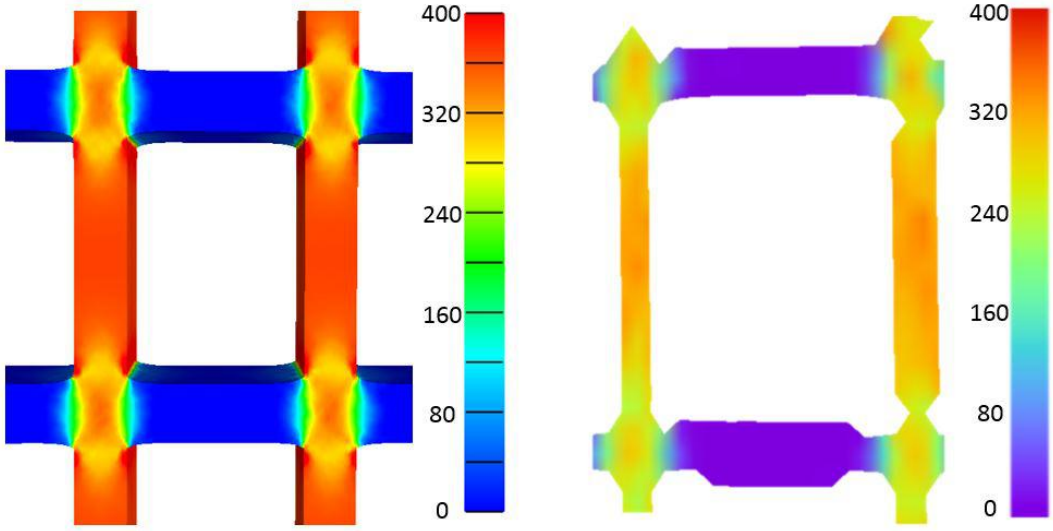

Figure B.13: Comparison between vertical strain in the structure with 5 5 cells at 50 N load: (a) FEBio model and (b) experimental. Note that the two figures are shown at similar scale bars (the colours are software-specific). The strain shown is in mstrain.

For all structures, there are slight differences between the finite element simulations and experimental results. These differences can be attributed to assumptions made within the modelling process. One example would be the material model representing the silicone used to create the structures. For this study, a neo-Hookean hyperelastic model was chosen with parameters determined experimentally. Furthermore, there is a variation in the experimental results between samples making it difficult to evaluate the difference between finite element simulations and experimental testing. More experimental testing is required to assess these variations.

Analysis of FEM data

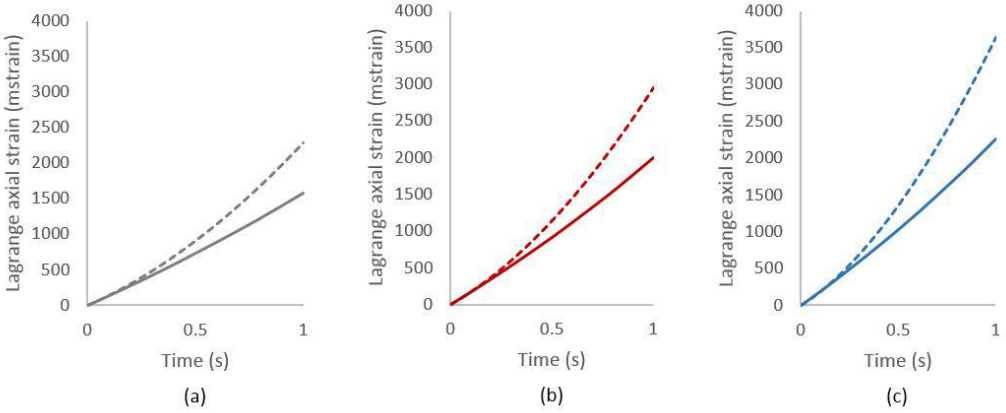

Figure B.14: Additional analysis of the finite element models for each structure, with (a) showing the 3×3 structure, (b) showing the 5×5 structure and (c) showing the 9×9 structure. The solid lines show the response of the centre cell joint and the dashed lines show the response of the centre cell vertical wall. Each figure shows the total structure displacement against the Lagrange axial strain (mstrain).

In order to understand the difference in behaviour between the different structures investigated as part of this study further analysis of the FEM models was conducted. As part of this analysis, it was found that the joints within the structures exhibit a different non-linear behaviour compared to the cell walls (Figure B.14). The non-linear behaviour of the joints changes due to the extra constraints, therefore when the number and size of the joints changes within a structure, the mechanical response of the structure changes. Figure B.14 shows that, in the small strain regime, the difference between the response of the cell joint and the cell wall is negligible, with the difference increasing outside of the small strain regime. This trend can be seen in all structures investigated as part of this study.

B.3 Conclusion

In general, for different cellular structures with linear elastic cell walls, containing the same volume of solid material, which is distributed either as a small number

of large cells or as a larger number of smaller cells, when the ratio between the thickness and the length of a wall is the same, the stiffness of the corresponding structure is expected to be the same [66]. For similar structures of non-linear elastic material also, this behaviour appears reasonable under small strains. However, in real structures, under sufficiently large strains, the cell size is expected to have a more independent effect, even though this effect may be relatively minor or harder to separate from other mechanical responses [9, 145].

The aim of this paper was to separate the cell size effect from other non-linear elastic responses when the size of the cells and the size of the structure are comparable (i.e., the cells are not infinitesimally small relative to the cellular sample). Specifically, for cellular structures with uniform cell size, shape, and distribution, we demonstrated experimentally, for the first time, that, under large-strain deformations, the stiffness in cell walls made from an isotropic non-linear hyperplastic material increases when the number of cells increases while the volume of solid material and the ratio between the thickness and the length of the wall remain fixed. This can be attributed to the non-linear responses of the elastic cell wall joints in addition to that of the cell walls. Therefore, when the number and size of the joints changes, the response of the structure will change. Further investigation is required to understand the limits of the structures in regard to their stiffness.

For our experimental tests, we developed a novel loading method for cellular structures under uniaxial tensile tests, which allows for a structure to be loaded in such a way that the end-effects are minimal and the boundary conditions are suitable for non-linear elastic analysis under large strains.

In addition to the experimental study, we constructed computational models which simulate the physical structures and reproduce the elastic effects observed experimentally. Finite element models are suitable for further investigation of three-dimensional structures with different cell size or cell wall material parame-

ters, and subject to different loads [118, 119].

Although many natural structures are irregular, cellular structures with regular geometry are easily reproducible and can be studied systematically to identify the independent influence of different properties [103, 104, 118, 119, 144]. In particular, our analysis offers valuable insight into the independent mechanical effect of cell size for structures under large elastic strains, which cannot be captured within the linear elasticity framework. Our results naturally open the door to many new questions, and will inspire further theoretical and experimental investigations.

Appendix C

FEBio SDDP configuration

If the reader wishes to implement their own SDDP in FEBio the following extract from a .FEB file will be useful. Stated below are the parameters for each analysis step and the tied and sliding contact interfaces. These parameters are known to work in FEBio v2.5.0.

```
<?xml version="1.0" encoding="ISO-8859-1"?>
<febio_spec version="2.0">
<Step name="Step01">
<Module type="solid"/>
<Control>
        <time_steps>10</time_steps>
        <step_size>0.1</step_size>
        <max_refs>15</max_refs>
        <max_ups>0</max_ups>
        <dtol>0.001</dtol>
        <etol>0.01</etol>
        <rtol>0</rtol>
        <lstol>0.9</lstol>
        <time_stepper>
```

```
                <dtmin>0.01</dtmin>
                <dtmax>0.1</dtmax>
                <max_retries>5</max_retries>
                <opt_iter>10</opt_iter>
        </time_stepper>
        <analysis type="static"/>
</Control>
<Contact>
        <contact type="tied" name="Tied01">
                <laugon>1</laugon>
                <tolerance>0.2</tolerance>
                <penalty>1000</penalty>
                <minaug>0</minaug>
                <maxaug>10</maxaug>
                <surface type="master">...</surface>
                <surface type="slave">...</surface>
        </contact>
<Step name="Step02">
<Module type="solid"/>
<Control>
        <time_steps>1</time_steps>
        <step_size>1</step_size>
        <max_refs>15</max_refs>
        <max_ups>0</max_ups>
        <dtol>0.001</dtol>
        <etol>0.01</etol>
        <rtol>0</rtol>
        <lstol>0.9</lstol>
```

```
        <time_stepper>
                <dtmin>0.1</dtmin>
                <dtmax>1</dtmax>
                <max_retries>1000</max_retries>
                <opt_iter>10</opt_iter>
        </time_stepper>
        <analysis type="static"/>
</Control>
<Contact>
        <contact type="facet-to-facet sliding" name="Sliding01">
                <laugon>1</laugon>
                <tolerance>0.2</tolerance>
                <penalty>30</penalty>
                <two_pass>1</two_pass>
                <auto_penalty>0</auto_penalty>
                <fric_coeff>0</fric_coeff>
                <fric_penalty>0</fric_penalty>
                <search_tol>0.01</search_tol>
                <minaug>0</minaug>
                <maxaug>10</maxaug>
                <gaptol>0</gaptol>
                <seg_up>0</seg_up>
                <surface type="master">...</surface>
                <surface type="slave">...</surface>
        </contact>
</Contact>
</Step>
</febio_spec>
```

Bibliography

[1] Adeeb SM, Epstein M. 2009. Fractal elements. Journal of Mechanics of Materials and Structures 4, 781-797.

[2] Adler JH, Emerson DB, Farrell PE, Maclachlan SP. 2017. Combining deflation and nested iteration for computing multiple solutions of non-linear variational problems. SIAM Journal of Scientific Computing 39(1), 29-52.

[3] Ainsworth M, Mihai LA. 2006. A comparison of solvers for linear complementarity problems arising from large-scale masonry structures. Applications of Mathematics 51(2), 93-128.

[4] Ajdari A, Jahromi BH, Papadopoulos J, Nayeb-Hashemi H, Vaziri A. 2012. Hierarchical honeycombs with tailorable properties. International Journal of Solids and Structures 49, 1413-1419.

[5] Alamar MC, Vanstreels E, Oey ML, Molto E, Nicolai BM. 2008. Micromechanical behaviour of apple tissue in tensile and compression tests: Storage conditions and cultivar effect. Journal of Food Engineering 86, 324-333.

[6] Alayyash K. 2017. The non-linear elasticity of cellular bodies under large deformations. PhD thesis. Cardiff University, Cardiff, UK.

[7] Ashby MF, Easterling KE, Harrysson R, Maiti SK. 1985. The fracture and toughness of woods. Proceedings of the Royal Society of London 398, 261-280.

[8] Baker M, Ericksen JL. 1954. Inequalities restricting the form of stress-deformation relations for isotropic elastic solids and Reiner-Rivlin fluids. Journal of the Washington Academy of Sciences 44, 24-27.

[9] Barett AH, Cardello AV, Lesher LL, Taub IA. 1994. Cellularity, mechanical failure, and textural perception of corn meal extrudates. Journal of Texture Studies 25, 77-95.

[10] Beatty MF, Stalnaker DO. 1986. The Poisson function of finite elasticity. Journal of Applied Mathematics 53, 807-813.

[11] Beatty MF. 1989. Gent-Thomas and Blatz-Ko models for foamed elastomers. In Mechanics of Cellulosic and Polymeric Materials, AMD v. 99 (MD v. 13), R. W. Perkins ed, American Society of Mechanical Engineering, New York, 75-78.

[12] Beatty MF. 1996. Introduction to non-linear elasticity. In Non-linear Effects in Fluids and Solids, M. M. Carroll, M. A. Hayes eds., Plenum Press, New York and London, 13-104.

[13] Beatty MF. 2001. Seven lectures in finite elasticity. In Topics in Finite Elasticity, M. Hayes, G. Saccomandi eds., Springer-Verlag, Wien, 31-93.

[14] De Belie N, Harlett IC, Harker FR, Baerdemaeker JD. 2000. Influence of ripening and turgor on the tensile properties of pears: A microscopic study of cellular and tissue changes. Journal of the American Society for Horticultural Science 125(3), 350-356.

[15] Blatz PJ, Ko WL. 1962. Application of finite elastic theory to deformation of rubbery materials. Transactions of The Society of Rheology 6, 223-251.

[16] Boccaccio A, Uva AE, Fiorentino M, Lamberti L, Monno G. 2016. A mechanobiology-based algorithm to optimize the microstructure geometry of bone tissue scaffolds. International Journal of Biological Sciences 12, 1-17.

[17] Bourne MV. 1980. Texture evaluation of horticultural crops. Horticultural Science 15, 51-57.

[18] Bruce DM. 2003. Mathematical modelling of the cellular mechanics of plants. Philosophical transactions of the Royal Society of London. Series B, Biological sciences 358(1437), 1437-1444.

[19] Brummell DA. 2006. Cell wall disassembly in ripening fruit. Functional Plant Biology 33(2), 103-119.

[20] Broedersz CP, MacKintosh FC. 2014. Modeling semiflexible polymer networks. Review of Modern Physics 86, 995-1036.

[21] Bronik K. 2017. Implementation and validation of a cohesive fracture model through contact mechanics with application to cutting and needle insertion into human skin. PhD thesis. Cardiff University, Cardiff, UK.

[22] Chen H, Zhu F, Jang KI, Feng X, Rogers JA, Zhang Y, Huang Y, Ma Y. 2017. The equivalent medium of cellular substrate under large stretching, with applications to stretchable electronics. Journal of the Mechanics and Physics of Solids 000, 1-9.

[23] Cheng GD, Cai YW, Xu L. 2013. Novel implementation of homogenization method to predict effective properties of periodic materials. Acta Mechanica Sinica 29(4), 550-556.

[24] Chirico S, Di Bari V, Foster T, Gray D. 2018. Enhancing the recovery of oilseed rape seed oil bodies (olesomes) using bicarbonate-based soaking and grinding media. Food Chemistry 241, 419-426.

[25] Ciarlet PG, Necăs JN. 1985. Unilateral problems in non-linear, three-dimensional elasticity. Archive for Rational Mechanics and Analysis 87, 319-338.

[26] Ciarlet PG, Necăs JN. 1987. Injectivity and self-contact in non-linear elasticity. Archive for Rational Mechanics and Analysis 97, 171-188.

[27] Civille GV. 2011. Food texture: pleasure and pain. Journal of Agricultural and Food Chemistry 59, 1487-1490.

[28] Cybulska J, Zdunek A, Psonka-Antonczyk KM, Stokke BT. 2012. The relation of apple texture with cell wall nanostructure studied using an atomic force microscope. Carbohydrate Polymers 92, 128-137.

[29] De Belie N, Hallett IC, Harker FR, De Baerdemaeker J. 2000. Influence of Ripening and Turgor on the Tensile Properties of Pears: A Microscopic Study of Cellular and Tissue Changes. Journal of the American Society for Horticultural Science 125(3), 350-356.

[30] Deshpande VS, Ashby MF, Fleck NA. 2001. Foam topology bending versus stretching dominated architectures. Acta Materialia 49, 1035-1040.

[31] Deshpande VS, Fleck NA, Ashby MF. 2001. Effective properties of the octet-truss lattice material. Journal of the Mechanics and Physics of Solids 49, 1747-1769.

[32] Destrade M, Gilchrist MD, Motherway J, Murphy JG. 2012. Slight compressibility and sensitivity to changes in Poisson's ratio. International Journal for Numerical Methods in Engineering 90, 403-411.

[33] Destrade M, Horgan CO, Murphy JG. 2015. Dominant negative Poynting effect in simple shearing of soft tissues. Journal of Engineering Mathematics 95(1), 87-98.

[34] Destrade M, Murphy JG, Saccomandi G. 2012. Simple shear is not so simple. International Journal of Non-Linear Mechanics 47, 210–214.

[35] Destrade M, Saccomandi G. 2010. On the rectilinear shear of compressible and incompressible elastic slabs. International Journal of Engineering Science 48, 1202-1211.

[36] Destrade M, Saccomandi G, Sgura I. 2009. Inhomogeneous shear of orthotropic incompressible non-linearly elastic solids: singular solutions and biomechanical interpretation. International Journal of Engineering Science 47, 1170–1181.

[37] Destrade M, Saccomandi G, Sgura I. 2017. Methodical fitting for mathematical models of rubber-like materials. Proceedings of the Royal Society A 473.

[38] Dinwoodie JM. 1981. Timber, its Nature and Behaviour. Van Nostrand Reinhold, NY, USA.

[39] Discher DE, Janmey P, Wang Y. 2005. Tissue cells feel and respond to the stiffness of their substrate. Science 310, 1139-1143.

[40] Dixon GR. 2007. Vegetable Brassicas and Related Crucifers. Centre for Agriculture and Biosciences International, Wallingford, UK.

[41] Dominy NJ, Yeakel JD, Bhat U, Ramsden L, Wrangham RW, Lucas PW. 2016. How chimpanzees integrate sensory information to select figs. Interface Focus 6(3), 20160001.

[42] Dunlop JWC, Fratzl P. 2013. Multilevel architectures in natural materials. Scripta Materialia 68, 8-12.

[43] Egan P, Ferguson S, Shea K. 2017. Design of hierarchical 3D printed scaffolds considering mechanical and biological factors for bone tissue engineering. Journal of Mechanical Design 139, 061401.

[44] Elsayed MSA, Pasini D. 2010. Multiscale structural design of columns made of regular octet-truss lattice material. International Journal of Solids and Structures 47, 1764-1774.

[45] Engelmayr Jr. GC, Papworth GD, Watkins SC, Mayer Jr. JE, Sacks MS. 2006. Guidance of engineered tissue collagen orientation by large-scale scaffold microstructures. Journal of Biomechanics 39, 1819-1831.

[46] Engelund ET, Svensson S. 2011. Predicting the reorientation of microfibrils in plant fibres under tensile strain. Unpublished.

[47] Engler AJ, Sen S, Lee Sweeney H, Discher DE. 2006. Matrix elasticity directs stem cell lineage specification. Cell 126, 677-689.

[48] Epstein M, Adeeb SM. 2008. The stiffness of self-similar fractals. International Journal of Solids and Structures 45, 3238-3254.

[49] Ericksen JL. 1955. Deformation possible in every compressible isotropic perfectly elastic materials. Journal of Mathematics and Physics 34, 126-128.

[50] Evans SL, Holt CA. 2009. Measuring the mechanical properties of human skin in vivo using digital image correlation and finite element modelling. The Journal of Strain Analysis for Engineering Design 44, 337-345.

[51] Fan HL, Jin FN, Fang DN. 2008. Mechanical properties of hierarchical cellular materials. Part I: Analysis. Composites Science and Technology 68, 3380-3387.

[52] Fichera G. 1964. Problemi elastostatici con vincoli unilaterali: il problema di Signorini con ambigue condizioni al contorno. Memorie della Accademia Nazionale dei Lincei 8, 91-140.

[53] Fisher DV. 1943. Mealiness and quality of Delicious apples as affected by growing conditions, maturity and storage techniques. Scientia Agricola 23, 569-588.

[54] Fleck NA, Deshpande VS, Ashby MF. 2010. Micro-architectured materials: Past, present and future. Proceedings of the Royal Society of London A: Mathematical, Physical and Engineering Sciences 466, 2495-2516.

[55] Fortes MA, Nogueira MT. 1989. The Poisson effect in cork. Materials Science and Engineering A 122, 227-232.

[56] Fournier M, Dlouhá J, Jaouen G, Almeras T. 2013. Integrative biomechanics for tree ecology: beyond wood density and strength. Journal of Experimental Botany, doi:10.1093/jxb/ert279.

[57] Fung YC. 1967. Elasticity of soft tissues in simple elongation. American Journal of Physiology 213(6), 1532-44.

[58] Gao Q, Pitt RE. 1990. Mechanics of parenchyma tissue based on cell orientation and microstructure. Transactions of the American Society of Agricultural Engineers 34, 232-238.

[59] Gates RS, Pitt RE, Ruina A, Cooke RJ. 1986. Cell wall elastic constitutive laws and stress-strain behaviour of plant and vegetable tissue. Biorheology 23, 453-466.

[60] Genovese K. 2009. A video-optical system for time-resolved whole-body measurement on vascular segments. Optics and Lasers in Engineering 47, 995-1008.

[61] Gent AN, Thomas AG. 1959. The deformation of foamed elastic materials. Journal of Applied Polymer Science 1, 107-113.

[62] Gent AN, Thomas AG. 1963. Mechanics of foamed elastic materials. Rubber Chemistry and Technology 36, 597-610.

[63] Gibson LJ. 2005. Biomechanics of cellular solids. Journal of Biomechanics. 38(3), 377-399.

[64] Gibson LJ. 2012. The hierarchical structure and mechanics of plant materials. Journal of The Royal Society Interface 9(76), 2749-2766.

[65] Gibson LJ, Ashby MF. 1997. Cellular Solids: Structure and Properties, 2nd ed, Cambridge University Press, Cambridge, UK.

[66] Gibson LJ, Ashby MF, Harley BA. 2010. Cellular Materials in Nature and Medicine, Cambridge University Press, Cambridge, UK.

[67] Goriely A. 2017. The Mathematics and Mechanics of Biological Growth, Springer, New York, USA.

[68] Green A, Adkins J. 1970. Large Elastic Deformations (and Non-linear Continuum Mechanics). Oxford University Press, 2 edition, Oxford, UK.

[69] Griffiths DF, Dold JW, Silvester DJ. 2015. Essential Partial Differential Equations. Springer International Publishing, 1st edition, Switzerland.

[70] Harker FR, Hallett IC. 1992. Physiological Changes Associated with Development of Mealiness of Apple Fruit during Cool Storage. American Society for Horticultural Science 27(2712), 1291-1294.

[71] Harker FR, Redgwell R, Harlett IC, Murray S. 1997. Texture of Fresh Fruit. Horticultural Reviews, 20.

[72] Hill R. 1978. Aspects of invariance in solid mechanics. Advances in Applied Mechanics 18, 1-75.

[73] Holzapfel GA. 2000. Non-linear Solid Mechanics: A Continuum Approach for Engineering, John Wiley & Sons, New York.

[74] Holzapfel GA, Ogden GA. 2009. Constitutive modelling of passive myocardium: a structurally-based framework for material characterization. Philosophical Transactions of the Royal Society B 367, 3445–3475.

[75] Hooke R. 1665. Micrographia: Or Some Physiological Descriptions of Minute Bodies Made by Magnifying Glasses with Observations and Inquiries Thereupon. Dover 1961, New York, USA.

[76] Horgan CO, Saccomandi G. 2005. A new constitutive theory for fiber reinforced incompressible nonlinearly elastic solids. Journal of Mechanics and Physics of Solids 53, 1985-2015.

[77] Jackman RL, Stanley DW. 1995. Perspectives in the textural evaluation of plant foods. Trends in Food Science & Technology 6, 187-194.

[78] Jackson DI. 1967. Relationship between cell size in the cortex and pith of apples and varietal susceptibility to internal breakdown and core flush. New Zealand Journal of Agricultural Research 10(2), 319-322.

[79] Jarvis MC. 1998. Intercellular separation forces generated by intracellular pressure. Plant, Cell and Environment, 21(12):1307-1310.

[80] Jenks MA, Bebeli PJ. 2011. Breeding for Fruit Quality. John Wiley & Sons, Inc, New Jersey, United States.

[81] Johnston JW, Hewett EW, Hertog MLATM. 2002. Postharvest softening of apple (Malus domestica) fruit: A review. New Zealand Journal of Crop and Horticultural Science 30, 145-160.

[82] Kikuchi N, Oden JT. 1988. Contact Problems in Elasticity: A Study of Variational Inequalities and Finite Element Methods. SIAM, Philadelphia, USA.

[83] Knychala J, Bouropoulos N, Catt CJ, Katsamenis OL, Please CP, Sengers BG. 2013. Pore geometry regulates early stage human bone marrow cell tissue formation and organisation. Annals of Biomedical Engineering 41, 917-930.

[84] Köhler L,Spatz H. 2002. Micromechanics of plant tissues beyond the linear-elastic range. Planta 215, 33-40.

[85] Kumar B, Chaudury SR. 1998. Finite inhomogeneous shearing deformations of a transversely isotropic incompressible material. Journal of Elasticity 51, 81-87.

[86] Kumar D, Singh BP, Kumar P. 2004. An overview of the factors affecting sugar content of potatoes. Association of Applied Biologists 145, 247-256.

[87] Lakes R. 1993. Materials with structural hierarchy. Nature 361, 511-515.

[88] Le Tallec P. 1994. Numerical Methods for Non-linear Elasticity. Handbook of Numerical Analysis, III(Part 1). PG Ciarlet and JL Lions eds., North-Holland, 465-624.

[89] Lewis R, Yoxall A, Marshall MB, Canty LA. 2008. Characterising pressure and bruising in apple fruit. Wear 264, 37-46.

[90] Lin T, Pitt RE. 1986. Rheology of apple and potato tissue as affected by cell turgor pressure. Journal of Texture Studies 17, 291-313.

[91] Lozano JE, Añón C, Parada-Arias E, Barbosa-Cánovas GV. 2002. Trends in Food Engineering, Technomic Publishing Company, Inc. Lancaster, PA, UK

[92] Maas SA, Ellis BJ, Ateshian GA, Weiss JA. 2012. FEBio: Finite elements for biomechanics. Journal of Biomechanical Engineering 134(1), 011005.

[93] Marzano M. 1983. An interpretation of Baker-Ericksen inequalities in uniaxial deformation and stress. Meccanica 18, 233-235.

[94] Meakin PJ, Roberts JA. 1990. Dehiscence of fruit in oilseed rape (Brassica napus L.) I. Anatomy of pod dihiscence. Journal of Experimental Botany 41, 995-1002.

[95] Meakin PJ, Roberts JA. 1990. Dehiscence of fruit in oilseed rape (Brassica napus L.) II. The role of cell wall degrading enzymes and ethylene. Journal of Experimental Botany 41, 1003-1011.

[96] Mebatsion HK, Verboven P, Melese Endalew A, Billen J, Ho QT, Nicolai BM. 2009. A novel method for 3-D microstructure modeling of pome fruit tissue using synchrotron radiation tomography images. Journal of Food Engineering 93, 141-148.

[97] Melnik AV, Borja Da Rocha H, Goriely A. 2015. On the modeling of fiber dispersion in fiber-reinforced elastic materials. International Journal of Non-Linear Mechanics 75, 92–106.

[98] Mendoza F, Verboven P, Mebatsion HK, Kerckhofs G, Wevers M, Nicolaï B. 2007. Three-dimensional pore space quantification of apple tissue using X-ray computed microtomography. Planta 226(3), 559-570.

[99] Merodio J, Ogden RW. 2005. Mechanical response of fiber-reinforced incompressible non-linearly elastic solids. International Journal of Non-Linear Mechanics 40, 213-227.

[100] Merodio J, Saccomandi G, Sgura I. 2007. The rectilinear shear of fiber-reinforced incompressible non-linearly elastic solids. International Journal of Non-Linear Mechanics 42, 342-354.

[101] Meza LR, Das S, Greer JR. 2014. Strong, lightweight, and recoverable three-dimensional ceramic nanolattices. Science 345, 1322-1326.

[102] Mihai LA. 2010. A fixed-point approach to the limit load analysis of multi-body structures with Coulomb friction. Computers and Structures 88(13-14), 859-869.

[103] Mihai LA, Alayyash K, Goriely A. 2015. Paws, pads, and plants: the enhanced elasticity of cell-filled load-bearing structures. Proceedings of the Royal Society A 471, 20150107.

[104] Mihai LA, Alayyash K, and Wyatt HL. 2017. The optimal density of cellular solids in axial tension. Computer Methods in Biomechanics and Biomedical Engineering 20(7), 701-713.

[105] Mihai LA, Fitt D, Woolley TE, Goriely A. 2018. Likely cavitation in stochastic elasticity. Journal of Elasticity, 1-16 (doi: 10.1007/s10659-018-9706-1).

[106] Mihai LA, Fitt D, Woolley T, Goriely A. 2019. Likely equilibria of stochastic hyperelastic spherical shells and tubes. Mathematics and Mechanics of Solids, 24(7), 2066-2082 (doi: 10.1177/1081286518811881).

[107] Mihai LA, Fitt D, Woolley TE, Goriely A. 2019. Likely oscillatory motions of stochastic hyperelastic solids. Transactions of Mathematics and Its Applications, doi: 10.1093/imatrm/tnz003.

[108] Mihai LA, Goriely A. 2011. Positive or negative Poynting effect? The role of adscititious inequalities in hyperelastic materials. Proceedings of the Royal Society A: Mathematical, Physical and Engineering Sciences 467(2136), 3633-3646.

[109] Mihai LA, Goriely A. 2013. Numerical simulation of shear and the Poynting effects by the finite element method: An application of the generalised empirical inequalities in non-linear elasticity. International Journal of Non-Linear Mechanics 49, 1-14.

[110] Mihai LA, Goriely A. 2014. Non-linear Poisson effects in soft honeycombs. Proceedings of the Royal Society A 470, 20140363.

[111] Mihai LA, Goriely A. 2015. Finite deformation effects in cellular structures with hyperelastic cell walls. International Journal of Solids and Structures 53, 107-128.

[112] Mihai LA, Goriely A. 2016. Guaranteed upper and lower bounds on the uniform load of contact problems in elasticity. SIAM Journal on Applied Mathematics 76(4), 1558–1576.

[113] Mihai LA, Goriely A. 2017. How to characterize a non-linear elastic material? A review on non-linear constitutive parameters in isotropic finite elasticity. Proceedings of the Royal Society A 473, 20170607.

[114] Mihai LA, Safar A, Wyatt H. 2018. Debonding of cellular structures with fibre-reinforced cell walls under shear deformation. Journal of Engineering Mathematics 109(1), 3-19.

[115] Mihai LA, Woolley TE, Goriely A. 2018. Stochastic isotropic hyperelastic materials: constitutive calibration and model selection. Proceedings of the Royal Society A 474, 20170858.

[116] Mihai LA, Woolley TE, Goriely A. 2018. Likely equilibria of the stochastic Rivlin cube. Philosophical Transactions of the Royal Society of London. Series A: Mathematical and Physical Sciences, 20180068.

[117] Mihai LA, Woolley TE, Goriely A. 2019. Likely chirality of stochastic anisotropic hyperelastic tubes. International Journal of Non-Linear Mechanics 114, 9-20 (doi: 10.1016/j.ijnonlinmec.2019.04.004).

[118] Mihai LA, Wyatt H, Goriely A. 2017. A microstructure-based hyperelastic model for open-cell solids. SIAM Journal on Applied Mathematics 77, 1397-1416.

[119] Mihai LA, Wyatt H, Goriely A. 2017. Microstructure-based hyperelastic models for closed-cell solids. Proceedings of the Royal Society A 473, 20170036.

[120] Moerman KM. 2018. GIBBON: The Geometry and Image-Based Bioengineering add-On. Journal of Open Source Software 3(22), 506.

[121] Mooney M. 1940. A theory of large elastic deformation. Journal of Applied Physics 11, 582-592.

[122] Niklas KJ. 1992. Plant Biomechanics: An Engineering Approach to Plant Form and Function. Chicago, IL: The University of Chicago Press.

[123] Nilsson SB, Hertz CH, Falk S. 1958. On the relation between turgor pressure and tissue rigidity. II. Physiologia Plantarum 11, 818-837.

[124] Oden JT. 2006. Finite Elements of Non-linear Continua, 2nd ed, Dover.

[125] Oey ML, Vanstreels E, De Baerdemaeker J, Tijskens E, Ramon H, Hertog MLATM, Nicolai B. 2007. Effect of turgor on micromechanical and structural properties of apple tissue: a quantitative analysis. Postharvest Biology and Technology 44, 240-247.

[126] Ogden RW. 1972. Large deformations isotropic elasticity - on the correlation of theory and experiment for incompressible rubberlike solids. Proceedings of the Royal Society A 326, 565-584.

[127] Ogden RW. 1997. Non-Linear Elastic Deformations. Dover, New York, USA. 2nd edition.

[128] Peretto R, Favaron F, Bettini V, De Lorenzo G, Marini S, Alghisi P, Cervone F, Bonfante P. 1992. Expression and localization of polygalacturonase during the outgrowth of lateral roots in Allium porrum L. Planta 188, 164-172.

[129] Peyton SR, Ghajar CM, Khatiwala CB, Putnam AJ. 2007. The emergence of ECM mechanics and cytoskeletal tension as important regulators of cell function. Cell Biochemistry and Biophysics 47, 300-320.

[130] Pitt RE, Davis DC. 1984. Finite element analysis of fluid-filled cell response to external loading. Transaction of the ASAE 27(6), 1976-1983.

[131] Qiong G, Pitt RE. 1990. A mechanics model of the compression of cells with finite contact area. Biorheology 27, 225-240.

[132] Rajagopal KR, Wineman AS. 1987. New universal relations for non-linear isotropic elastic materials. Journal of Elasticity 17, 75-83.

[133] Rajani S, Sundaresan V. 2001. The Arabidopsis myc/bHLH gene ALCATRAZ enables cell separation in fruit dehiscence. Current Biology 11, 1914-1922

[134] Rayneau-Kirkhope D, Mao Y, Farr R. 2012. Ultralight fractal structures from hollow tubes. Physical Review Letters 109, 204301.

[135] Reeve RM. 1967. A review of cellular structure, starch, and texture qualities of processed potatoes. Economic Botany 21, 294-308.

[136] Rich PM. 1986. Mechanical architecture of arborescent rain forest palms. Principes 30, 117-131.

[137] Rivlin RS. 1948. Large elastic deformations of isotropic materials. II. Some uniqueness theorems for pure, homogeneous deformation. Philosophical Transactions of the Royal Society A 240, 491-508.

[138] Rivlin RS. 1948. Large elastic deformations of isotropic materials. IV. Further developments of the general theory. Philosophical Transactions of the Royal Society A 241, 379–397.

[139] Roberts JA, Elliott KA, Gonzalez-Carranza ZH. 2002. Abscission, dehiscence, and other cell separation process. Annual Review of Plant Biology 53, 131-158.

[140] Roberts JA, Whitelaw CA, Gonzalez-Carranza ZH, McManus MT. 2000. Cell separation process in plants - models, mechanics and manipulation. Annals of Botany 86, 223-235.

[141] Roesler H. 1987. The history of some fundamental concepts in bone biomechanics. Journal of Biomechanics 20(11), 1025-1034.

[142] Rosenthal AJ, Lacresse A, Voyer E. 2018. Contribution of skin and stone to texture measurements of spherical model fruits. Journal of Texture Studies 49, 23–29

[143] Rumpler M, Woesz A, Dunlop JW, van Dongen JT, Fratzl P. 2008. The effect of geometry on three-dimensional tissue growth. Journal of the Royal Society Interface 5, 1173-1180.

[144] Safar AT, Mihai LA. 2018. The non-linear elasticity of hyperelastic models for stretch-dominated cellular structures. International Journal of Non-Linear Mechanics 106, pp. 144-154.

[145] Scanlon MG. 2005. Biogenic Cellular Solids, in Soft Materials: Structure and Dynamics. Marcel Dekker, New York, USA.

[146] Sexton R, Roberts JA. 1982. Cell biology of abscission. Annual Reviews of Plant Physiology 33, 133-162.

[147] Shield RT. 1971. Deformations possible in every compressible, isotropic, perfectly elastic material. Journal of Elasticity 1, 91-92.

[148] Shih YRV, Tseng KF, Lai HY, Lin CH, Lee, OK. 2011. Matrix stiffness regulation of integrin-mediated mechanotransduction during osteogenic differentiation of human mesenchymal stem cells. Journal of Bone and Mineral Research 26, 730-738.

[149] Signorini A. 1933. Sopra alcune questioni di elastostatica. Atti Societ'a Italiana per il Progresso della Scienze 2(2), 231-251.

[150] Smee A. 1847. The Potatoe Plant, Its Uses and Properties. Kessinger Legacy Reprints, Whitefish, MT, USA.

[151] Spence J, Vercher Y, Gates P, Harris N. 1996. 'Pod shatter' in Arabidopsis thaliana, Brassica napusand B. juncea. Journal of Microscopy 181, 195-203.

[152] Steinmann P, Hossain M, Possart G. 2012. Hyperelastic models for rubber-like materials: consistent tangent operators and suitability for Treloar's data. Archive of Applied Mathematics 82(9), 1183-1217.

[153] Storakers B. 1986. On the material representation and constitutive branching in finite compressible elasticity. Journal of the Mechanics and Physics of Solids 34, 125-145.

[154] Sutton M, Orteu JJ, Schreire HW. 2009, Image correlation for shape, motion and deformation measurements: basic concepts, theory and applications, Springer, New York.

[155] Traveset A, Robertson AW, Rodriguez-Pérez. 2007. Seed Dispersal: Theory and Its Applications in a Changing World. Centre for Agriculture and Biosciences International, Wallingford, UK.

[156] Treloar LRG. 1944. Stress-strain data for vulcanized rubber under various types of deformation. Transactions of the Faraday Society 40, 59-70.

[157] Truesdell C, Noll W. 2004. The Non-Linear Field Theories of Mechanics. Springer, New York, USA. 3rd ed.

[158] Twardowski T. 2010. Chances, perspectives and dangers of GMO in agriculture. Journal of Fruit and Ornamental Plant Research 18(2), 63-69.

[159] Vigliotti A, Pasini D. 2012. Stiffness and strength of tridimensional periodic lattices. Computer Methods in Applied Mechanics and Engineering 229-232, 27-43.

[160] Vigliotti A, Pasini D. 2013. Mechanical properties of hierarchical lattices. Mechanics of Materials 62, 32-43.

[161] Weaire D, Fortes MA. 1994. Stress and strain in liquid and solid foams. Advances in Physics 43, 685-738.

[162] Weiss JA, Maker BN, Govindjee S. 1996. Finite element implementation of incompressible, transversely isotropic hyperelasticity. Computer Methods in Applied Mechanics and Engineering 135, 107-128.

[163] Wieding J, Wolf A, Bader R. 2014. Numerical optimization of open-porous bone scaffold structures to match the elastic properties of human cortical bone. Journal of the Mechanical Behavior of Biomedical Materials 37, 56-68.

[164] Winer JP, Oake S, Janmey PA. 2009. Non-linear elasticity of extracellular matrices enables contractile cells to communicate local position and orientation. PloS ONE 4, e6382.

[165] Wyatt HL, Pullin R, Yang THJ, Evans SL. 2016. Deformation during the electrosurgical vessel sealing process. Strain 52, 372-379.

[166] Yeung T, Georges PC, Flanagan LA, Marg B, Ortiz M, Funaki M, Zahir N, Ming W, Weaver V, Janmey PA. 2005. Effects of substrate stiffness on cell morphology, cytoskeletal structure, and adhesion. Cell Motility and the Cytoskeleton 60, 24–34.

[167] Yeoh OH, Fleming PD. 1998. A new attempt to reconcile the statistical and phenomenological theories of rubber elasticity. Journal of Polymer Science Part B: Polymer Physics 35, 1919–1931.

[168] Zdunek A, Kozioł A, Cybulska J, Lekka M, Pieczywek PM. 2016. The stiffening of the cell walls observed during physiological softening of pears. Planta.

[169] Zdunek A, Umeda M. 2004. Influence of cell size and cell wall volume fraction of failure properties of potato and carrot tissue. Journal of Texture Studies 36, 25-43.

[170] Zhang D, Arola DD. 2004. Applications of digital image correlation to biological tissues. Journal of Biomedical Optics 9, 691-699.

[171] Zhang H, Landmann F, Zahreddine H, Rodriguez D, Koch M, Labouesse M. 2011. A tension-induced mechanotransduction pathway promotes epithelial morphogenesis. Nature 471, 99-103.

[172] Zheng X, Lee H, Weisgraber TH, Shusteff M, DeOtte J, Duoss EB, Kuntz JD, Biener MM, Ge Q, Jackson JA, Kucheyev SO, Fang NX, Spadaccini CM. 2014. Ultralight, ultrastiff mechanical metamaterials. Science 344, 1373-1377.

[173] Zheng X, Smith W, Jackson JA, Moran B, Cui H, Chen D, Ye J, Fang N, Rodriguez N, Weisgraber TH, Spadaccini CM. 2016. Multiscale metallic metamaterials. Nature Materials 15, 1100-1106.

[174] Zhu HX, Melrosez JR. 2003. A mechanics model for the compression of plant and vegetative tissues. Journal of Theoretical Biology 221, 89-101.